Design of 2D Material-Based Heterostructures for Rechargeable Batteries

A thesis presented for the award of the degree of

Doctor of Philosophy

from

University of Technology Sydney

By

Shijian Wang, B. Sc., M. Eng.

January 2022

CERTIFICATE OF ORIGINAL AUTHORSHIP

I, *Shijian Wang* declare that this thesis, is submitted in fulfilment of the requirements for the award of *Doctor of Philosophy*, in the *School of Mathematics and Physical Sciences, Faculty of Science* at the University of Technology Sydney.

This thesis is wholly my own work unless otherwise referenced or acknowledged. In addition, I certify that all information sources and literature used are indicated in the thesis.

This document has not been submitted for qualifications at any other academic institution.

This research is supported by the Australian Government Research Training Program.

Production Note:
Signature removed prior to publication.

January 2022

DEDICATION

This thesis is dedicated to my family and my beloved scientific career.

ACKNOWLEDGEMENTS

So many people provided generous help during my three and a half-year Ph.D. studying period, especially in the COVID-19 pandemic. Firstly, I would like to sincerely appreciate my principal supervisor, Prof. Guoxiu Wang, for his kind, patient and continuous support and valuable guidance within my Ph.D. study. I would also like to thank my co-supervisors, Dr. Pan Xiong, Dr. Jinqiang Zhang and Dr. Xin Guo for their professional advice and enthusiastic support on my research. Besides, I am deeply grateful to Dr. Jane Yao for her selfless and kind assistance to my laboratory work.

Special thanks are given to my colleagues at UTS, Dr. Bing Sun, Dr. Hao Liu, Dr. Dawei Su, Dr. Yufei Zhao, Dr. Dong Zhou, Dr. Weizhai Bao, Dr. Liubing Dong, Dr. Weihong Lai, Dr. Hao Tian, Dr. Hong Gao, Dr. Xiao Tang, Dr. Xiaochun Gao, Dr. Yi Chen, Dr. Kang Yan, Dr. Tianyi Wang, Dr. Fan Zhang, Min Luo, Pauline Jaumaux, Javad Safaei, Yuhan Xie, Zefu Huang, and all other members for your kind assistance and collaboration in my PhD study and life.

I am also grateful to the collaborators beyond UTS, Prof. Peter H. L. Notten, Dr. Guiyin Xu, Dr. Peng Li, Dr. Rui Zang, Sai Zhao, Jian Yang, and all people helped me.

In addition, I wish to thank the administrative and technical support that I received from Dr. Ronald Shimmon, Dr. Linda Xiao, Elizabeth Gurung Tamang, Herbert Yuan, Mark Lockery, Helen Xu, and other staff in MaPS, MAU, and Faculty of Science.

The financial support from UTS scholarships and Australian Research Council (ARC) through the Discovery Projects (DP180102297) are gratefully acknowledged.

Last but not the least, I would like to thank my parents, and my girlfriend Xiaona Chang for supporting me spiritually and materially throughout my PhD period and my life.

LIST OF PUBLICATIONS

1. **Shijian Wang**,[1] Sai Zhao,[1] Xin Guo,* Guoxiu Wang,* "2D Material-Based Heterostructures for Rechargeable Batteries", ***Advanced Energy Materials***, 2022, 12, 2100864.

2. **Shijian Wang**,[1] Pan Xiong,[1]* Jinqiang Zhang, Guoxiu Wang,* "Recent progress on flexible lithium metal batteries: Composite lithium metal anodes and solid-state electrolytes", ***Energy Storage Materials***, 2020, 29, 310-331.

3. **Shijian Wang**, Pan Xiong,* Xin Guo, Jinqiang Zhang, Xiaochun Gao, Fan Zhang, Xiao Tang, Peter H. L. Notten, Guoxiu Wang,* "A stable Conversion and Alloying Anode for Potassium-Ion Batteries: A Combined Strategy of Encapsulation and Confinement", ***Advanced Functional Materials***, 2020, 30, 2001588.

4. **Shijian Wang,** Xin Guo,* Javad Safaei, Peng Li,* Yaojie Lei, Yufei Zhao, Zefu Huang, Qinfen Gu, Qiaobao Zhang, Bing Sun, Guoxiu Wang,* "Pre-Introduced Strain Enhancing Structural Stability of δ-MnO_2 in Aqueous Zinc-Ion Batteries", Ready for submission.

5. Xin Guo,[1] Hong Gao,[1] **Shijian Wang**,[1] Guang Yang, Xiuyun Zhang,* Jinqiang Zhang, Hao Liu,* Guoxiu Wang,* "MXene-Based Aerogel Anchored with Antimony Single Atoms and Quantum Dots for High-Performance Potassium-Ion Batteries", ***Nano Letters***, 2022, In press, Doi: 10.1021/acs.nanolett.1c04389.

6. Pengxin Li, Xin Guo,* Rui Zang, **Shijian Wang**, Yuqi Zuo, Zengming Man, Peng Li,* Shuaishuai Liu, Guoxiu Wang,* "Nanoconfined SnO_2/$SnSe_2$ heterostructures in N-doped carbon nanotubes for high-performance sodium-ion batteries", ***Chemical Engineering Journal***, 2021, 418, 129501.

7. Xiao Tang, Dong Zhou,* Bao Zhang, **Shijian Wang**, Peng Li, Hao Liu, Xin Guo, Pauline Jaumaux, Xiaochun Gao, Yongzhu Fu, Chengyin Wang, Chunsheng Wang,* Guoxiu Wang,* "A universal strategy towards high–energy aqueous multivalent–ion batteries", ***Nature Communications***, 2021, 12, 2857.

8. Yuqi Zuo, Peng Li,* Rui Zang, **Shijian Wang**, Zengming Man, Pengxin Li, Siyu Wang, Wei Zhou, "Sulfur-Doped Flowerlike Porous Carbon Derived from Metal–Organic Frameworks as a High-Performance Potassium-Ion Battery Anode", ***ACS Applied Energy Materials***, 2021, 4, 2282-2291.

9. Pan Xiong, Fan Zhang, Xiuyun Zhang, Yifan Liu, Yunyan Wu, **Shijian Wang**, Javad Safaei, Bing Sun, Renzhi Ma, Zongwen Liu, Yoshio Bando, Takayoshi Sasaki, Xin Wang, Junwu Zhu,* Guoxiu Wang,* "Atomic-scale tandem regulation of anionic and cationic migration for long-life alkali metal batteries", ***Nature Communications***, 2021, 12, 4184.

10. Yufei Zhao, Jinqiang Zhang,* Yuhan Xie, Bing Sun, Junjie Jiang, Wen-Jie Jiang, Shibo Xi, Hui Ying Yang, Kang Yan, **Shijian Wang**, Xin Guo, Peng Li, Zhaojun Han, Xunyu Lu, Hao Liu,* Guoxiu Wang,* "Constructing Atomic heterometallic sites in ultrathin nickel-incorporated cobalt phosphide nanosheets via a boron-assisted strategy for highly efficient water splitting", ***Nano Letters***, 2021, 21, 823-832.

11. Eider Goikolea, Verónica Palomares, **Shijian Wang**, Idoia Ruiz de Larramendi, Xin Guo, Guoxiu Wang,* Teofilo Rojo,* "Na-Ion Batteries—Approaching Old and New Challenges", ***Advanced Energy Materials***, 2020, 10, 2002055.

12. Guiyin Xu,* Daiwei Yu, Dongchang Zheng, **Shijian Wang**, Weijiang Xue, Xiangkun Elvis Cao, Hongxia Zeng, Xianghui Xiao, Mingyuan Ge, Wah-Keat Lee, Meifang

Zhu,* “Fast heat transport inside lithium-sulfur batteries promotes their safety and electrochemical performance”, ***iScience***, 2020, 23, 101576.

13. Hao Tian, Huajun Tian, **Shijian Wang**, Shuangming Chen, Fan Zhang, Li Song,* Hao Liu,* Jian Liu,* Guoxiu Wang,* “High-power lithium–selenium batteries enabled by atomic cobalt electrocatalyst in hollow carbon cathode”, ***Nature Communications***, 2020, 11, 5025.

14. Kang Yan, Shuoqing Zhao, Jinqiang Zhang, Javad Safaei, Xingxing Yu, Tianyi Wang, **Shijian Wang**, Bing Sun,* Guoxiu Wang,* “Dendrite-free sodium metal batteries enabled by the release of contact strain on flexible and sodiophilic matrix”, ***Nano Letters***, 2020, 20, 6112-6119.

15. Pan Xiong, Fan Zhang, Xiuyun Zhang, **Shijian Wang**, Hao Liu, Bing Sun, Jinqiang Zhang, Yi Sun, Renzhi Ma, Yoshio Bando, Cuifeng Zhou, Zongwen Liu, Takayoshi Sasaki,* Guoxiu Wang,* “Strain engineering of two-dimensional multilayered heterostructures for beyond-lithium-based rechargeable batteries”, ***Nature Communications***, 2020, 11, 3297.

16. Hong Gao, Xin Guo,* **Shijian Wang**, Fan Zhang, Hao Liu,* Guoxiu Wang,* “Antimony-based nanomaterials for high-performance potassium-ion batteries”, ***EcoMat***, 2020, 2, e12027.

17. Pan Xiong, Bing Sun, Nobuyuki Sakai, Renzhi Ma,* Takayoshi Sasaki,* **Shijian Wang**, Jinqiang Zhang, Guoxiu Wang,* “2D superlattices for efficient energy storage and conversion”, ***Advanced Materials***, 2020, 32, 1902654.

18. Yufei Zhao, **Shijian Wang**, Hao Liu, Xin Guo, Xingrong Zeng, Wenjian Wu,* Jinqiang Zhang,* Guoxiu Wang,* “Porous Mo_2C nanorods as an efficient catalyst for

the hydrogen evolution reaction", ***Journal of Physics and Chemistry of Solids***, 2019, 132, 230-235.

19. Pan Xiong, Xiuyun Zhang, Hao Wan, **Shijian Wang**, Yufei Zhao, Jinqiang Zhang, Dong Zhou, Weicheng Gao, Renzhi Ma,* Takayoshi Sasaki,* Guoxiu Wang,* "Interface modulation of two-dimensional superlattices for efficient overall water splitting", ***Nano Letters***, 2019, 19, 4518-4526.

20. Xuemei Li, **Shijian Wang**, Xiao Tang, Rui Zang, Peng Li, Pengxin Li, Zengming Man, Cong Li, Shuaishuai Liu, Yuhan Wu, Guoxiu Wang,* "Porous $Na_3V_2(PO_4)_3$/C nanoplates for high-performance sodium storage", ***Journal of Colloid and Interface Science***, 2019, 539, 168-174.

21. Zengming Man, Peng Li, Dong Zhou,* Rui Zang, **Shijian Wang**, Pengxin Li, Shuaishuai Liu, Xuemei Li, Yuhan Wu, Xiaohui Liang, Guoxiu Wang,* "High-performance lithium–organic batteries by achieving 16 lithium storage in poly (imine-anthraquinone)", ***Journal of Materials Chemistry A***, 2019, 7, 2368-2475.

22. Pengxin Li, Xin Guo, **Shijian Wang**, Rui Zang, Xuemei Li, Zengming Man, Peng Li, Shuaishuai Liu, Yuhan Wu, Guoxiu Wang,* "Two-dimensional Sb@TiO_{2-x} nanoplates as a high-performance anode material for sodium-ion batteries", ***Journal of Materials Chemistry A***, 2019, 7, 2553-2559.

Table of Contents

TABLE OF FIGURES

LIST OF TABLES

ABSTRACT

Two-dimensional (2D) materials have been regarded as promising electrode materials for rechargeable batteries because of their advantages in providing ample active sites and improving electrochemical reaction kinetics. However, it remains great challenges for 2D materials to fulfill all requirements for high-performance energy storage devices in terms of electronic conductivity, the number of accessible active sites, structural stability, and mass production capability. Recent advances in constructing 2D material-based heterostructures offer opportunities for utilizing synergistic effects between the individual blocks to achieve optimized properties and enhanced performance for rechargeable batteries. In this doctoral thesis, several 2D material-based heterostructures varying from 0D-2D, 1D-2D to 2D-2D heterostructures have been designed, synthesized, and applied to rechargeable batteries. These include Sb single atoms and quantum dots co-decorated $Ti_3C_2T_x$ MXene-based aerogels (0D-2D heterostructure), N-doped conductive carbon coating and 2D graphene nanosheets co-modified Sb_2Se_3 nanorods (1D-2D heterostructure), and superlattice-like 2D-2D heterostructure constructed by unilamellar MnO_2 and graphene nanosheets. The specific morphology features, physicochemical properties of these heterostructures, and their functions on ion storage mechanisms and kinetics have also been deeply investigated. The enlightening techniques in this thesis provide promising design strategies for 2D material-based heterostructure electrodes in rechargeable batteries.

INTRODUCTION

The prevalent trend of energy transformation from traditional fossil fuels to clean renewable energy inspires the rapid development of energy storage, especially rechargeable batteries. In our daily life, those electrode materials with low cost, high energy density, and good safety exhibit infinite prospects in applying electric vehicles, large-scale electrochemical energy storage, and portable and wearable devices. Two-dimensional (2D) materials can be a good candidate benefiting from their unique open planar ionic channels, large specific surface areas, excellent mechanical robustness, and flexibility. Even so, none of the unary 2D material meets all requirements of electrode materials in rechargeable batteries, like specific capacity, working voltage, conductivity, mechanical stability, *etc.* For example, although graphene and MXene anode materials have low working voltage, excellent conductivities and mechanical flexibility and stability, their poor specific capacity limits the application in high-energy-density battery systems. Reversely, phosphorene anodes exhibit very high specific capacity, which can even reach 2500 mAh g^{-1} in lithium-ion batteries. However, their alloying reaction mechanism will cause a severe volume change during charge-discharge processes, and finally result in structure degradation and pulverization. As for transition metal dichalcogenides (TMDs) and transition metal oxides (TMOs), their relatively high working voltages, often over 1V, cut down the power density of full cells when coupled with cathodes. Constructing 2D material-based heterostructures coupling with various dimensional building blocks presents the potential on filling the gaps of solo 2D materials, and meanwhile has the possibility of introducing unexpected new physicochemical properties.

The exploration and design of 2D material-based heterostructures for rechargeable batteries is the principal theme throughout this doctoral thesis, including the manufacturing techniques on combining different dimensional units and 2D species, the study and adjustment of physical and chemical features in specific configurations, and the electrochemical performance with related mechanisms in rechargeable batteries. Each chapter is outlined as follows:

a) Chapter 1 summarizes the recent development of 2D material-based heterostructures for rechargeable batteries. This section introduces several traditional constructing strategies, such as manually transfer-assembly, liquid-phase self-assembly, and *in-situ* growth processing, and then the unique features of different configurations ranging from 0D-2D, 1D-2D to 2D-2D heterostructures. Besides, the modification of 2D material-based heterostructures is also illustrated, including surface optimization and defect engineering. At last, the functional roles of 2D material-based heterostructures in rechargeable batteries are classified into four aspects, in terms of boosted charge transfer, promoted ion diffusion, restricted volume expansion, and enhanced electrochemical reactivities in detail.
b) Chapter 2 is the experimental section, explaining the construction approaches of 2D material-based heterostructures we built, basic physiochemical characterizations and electrochemical tests.
c) Chapter 3 introduces the fabrication 0D-2D heterostructures that is antimony (Sb) single atoms and quantum dots embedded on MXene nanosheets. The obtained heterostructure anodes exhibit improved charge transfer kinetics, enhanced potassium storage capability, reinforced structural stability in potassium-ion batteries.
d) Chapter 4 combines conductive encapsulation and 2D confinement strategies to build 1D-2D heterostructures, where N-doped carbon encapsulated antimony selenide

(Sb_2Se_3) nanorods are well confined between flexible reduced graphene oxide (rGO) nanosheets. The all-around protection to Sb_2Se_3 nanorods successfully restricts their volume changes in potassium-ion batteries, and then promotes cycling stability. Besides, the complicated potassium storage mechanism of Sb_2Se_3 is deeply revealed.

e) Chapter 5 demonstrates the construction of 2D-2D heterostructures, a superlattice-like unilamellar δ-MnO_2 nanosheets coupled with positively charged rGO nanosheets via a liquid-phase electrostatic self-assembly method. The unique superlattice structure pre-introduces strains into MnO_2 crystal lattice, effectively prohibiting Mn dissolution in aqueous zinc-ion batteries. The fundamental studies demonstrate physicochemical features in superlattice and explain the generation of pre-introduced strains and their functional behaviours during cycling.

f) Chapter 6 concludes the entire thesis and puts forward perspectives toward the development of 2D material-based heterostructures.

Keywords: 2D materials, heterostructures, potassium-ion batteries, aqueous zinc-ion batteries, Sb quantum dots, MXene, Sb_2Se_3 nanorods, graphene, MnO_2 nanosheets

Chapter 1 Literature Review

Energy transformation from traditional sources to renewables is an irresistible trend owing to the finite supply of fossil fuels, like coal and petroleum, and the continuous fall of costs for renewable energy. The world-widely employed and developed renewable energy sources currently include solar, wind, geothermal and hydropower. Nuclear energy as a specific clean energy, although not renewable, is also a competitive candidate in the next-generation energy. However, they are not sufficiently cost-effective to every country now, because their discovery and development require for not only advanced conversion techniques and specific geographical and climatic conditions, but also reliable energy storage system due to their intermittent, regional, and weather-dependent properties. Australia has great potential in developing these clean and renewable energy sources, especially on solar and wind power.[1] Currently, batteries are the best choice for energy storage in the increasingly electrified world. Developing high-performance rechargeable batteries with low cost and high energy density is urgently demanded to meet the increasing needs of portable electronics, electric vehicles, and electric grids.[2-5] In particular, nanomaterials with a large electrochemically active surface and short ion diffusion paths can accelerate device reaction kinetics by orders of magnitude, which allows a significantly improved energy and power density and cycle life.[6,7]

The exploration of two-dimensional (2D) materials in rechargeable batteries has been developed extremely fast due to their unprecedented properties compared to their bulk counterparts.[8,9] Their open 2D channels facilitate ion transport and can endow all the material surfaces accessible, thereby resulting in fast charge storage and increased capacity. Furthermore, the high aspect ratio and superior mechanical properties render them promising for wearable technologies.[10] However, a single 2D material can barely

meet the manifold requirements for high-performance electrode materials. Besides, the large active surface area of 2D materials may bring new puzzles such as parasitic and irreversible reactions at the solid-electrolyte interface.[10,11]

Constructing 2D material-based heterostructures not only offers an effective pathway to overcome these limitations but also keeps the merits of pristine 2D materials, as well as bringing new possibilities by turning their physicochemical properties.[12] A number of heterostructures with varying dimensionalities have been created for energy-related applications. These 2D material-based heterostructures present unique properties such as superior mechanical strength, fast electronic and ionic conductivities, enhanced electrochemical activity, and structural stability.[13,14] For example, compositing electrically conductive graphene or MXenes (2D transition metal carbides and/or nitrides) with redox-active transition metal chalcogenides can simultaneously achieve a remarkably enhanced capacity and cycling performance.[15]

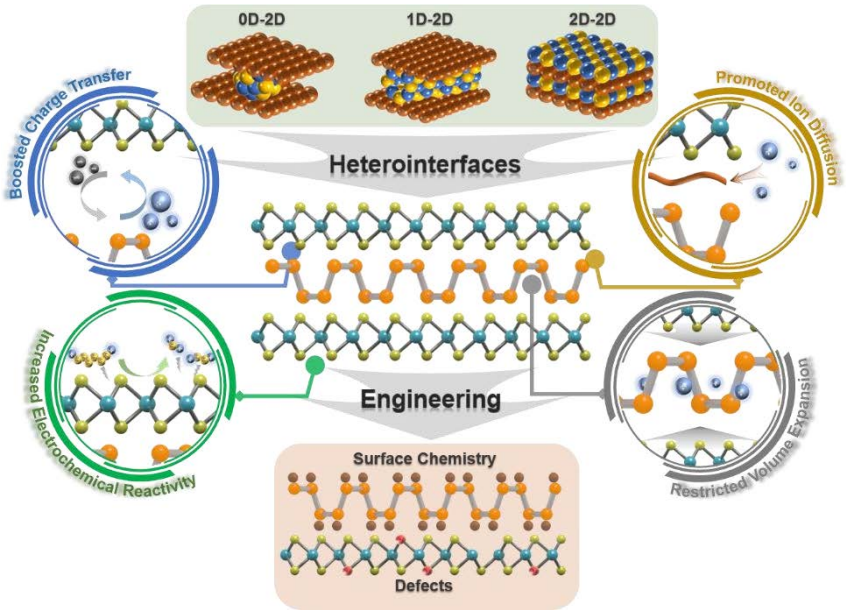

Figure 1.1 Schematic illustration for the primary functional roles of the mixed dimensional 2D material-based heterostructures in rechargeable batteries.

As novel 2D materials continually emerge, great flexibility for the fabrication of their heterostructures is expected. Here we present a critical literature review on emerging 2D material-based mixed dimensional heterostructures, with particular emphasis on their functionalities for rechargeable batteries, including alkali-ion batteries, multivalent-ion batteries, and lithium-sulfur batteries. We first introduce the general synthesis strategies for preparing heterostructures, including both covalently-bonded and van der Waals (vdW)-connected 2D material-based heterostructures. We then present the advances and limitations in two categories of mixed-dimensional heterostructures (namely, low dimensional-2D and 2D-2D heterostructures) and analyze the heterostructure engineering methodology beyond changing components. Finally, we discuss the applications of 2D material-based heterostructures according to their different roles in the context of rechargeable batteries (**Figure 1.1**).

1.1 Construction of 2D Material-Based Heterostructures

The synthetic strategies of preparing 2D heterostructures directly influence on their physical and chemical properties, as well as determining their application domain. Generally, mechanical assembly and *in-situ* growth methods are two conventional approaches to construct 2D heterostructures. Mechanical assembly methods, including manually transfer-assembly and electrostatically self-assembly approaches, can generate heterostructures based on vdW forces, which maintain the robust physical contact between different components. For the *in-situ* growth method, the components combine with each other at the atomic level by forming chemical bonding and thus give stabilize heterostructures.

1.1.1 Manually transfer-assembly

Mechanical assembly can precisely control the arrangement of heterostructures, which is of great importance for fundamental research on the physical properties of the desired heterostructures.[16-20] For example, Wang *et al*.[21] proposed a "pick-and-lift" method to realize layer-by-layer (LBL) assembly of a sandwich-like boron nitride (BN)/graphene heterostructure, in which a 2D crystal adhered on a membrane was brought into contact with another 2D crystal (**Figure 1.2a**). Owing to the strong vdW force between different crystals, the second 2D crystal are very likely to stick with the first one after lifting up the membrane. Such a method could precisely control the heterostructures and achieve a well-defined clean interface between the 2D nanomaterials, which is beneficial for electron mobility. However, such micromanipulation techniques are too complicated to scale up for rechargeable batteries.

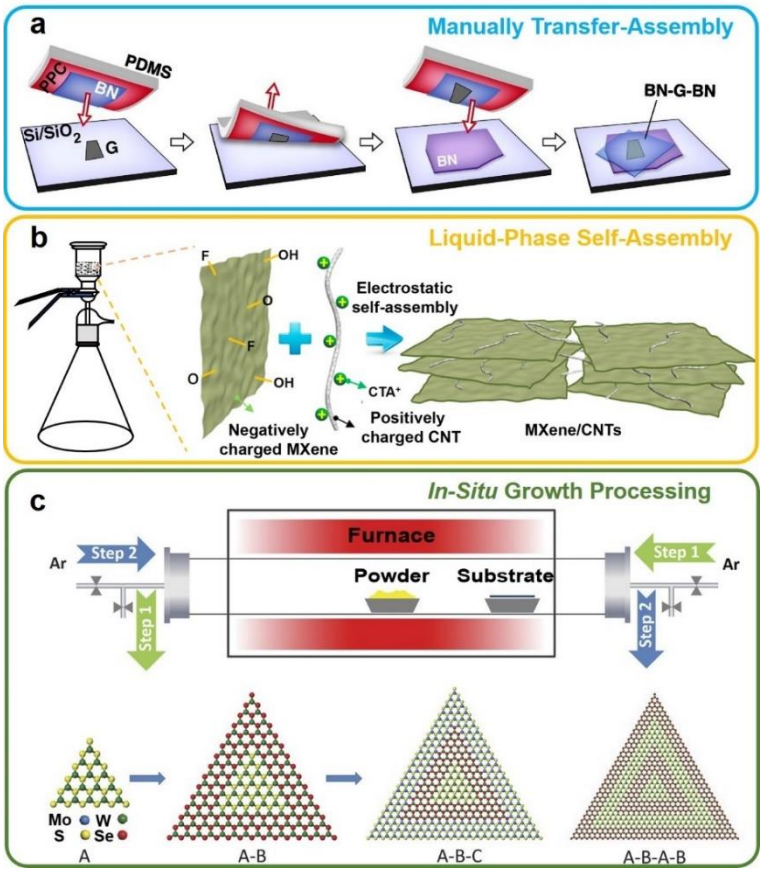

Figure 1.2 Synthetic methods of 2D material-based heterostructures. a) Schematic of the vdW technique for polymer-free assembly of layered materials.[21] b) Schematic showing the preparation of porous MXene ($Ti_3C_2T_x$)/CNT electrode by the self-assembly method.[22] c) Schematic illustration of a modified CVD system for robust epitaxial growth of lateral heterostructures. The precisely controlled flow can ensure the highly robust sequential growth of monolayer seed A, A−B heterostructure, A−B−C multi-heterostructure, and A−B−A−B superlattice.[23]

1.1.2 Liquid-phase self-assembly

2D materials synthesized by liquid-phase exfoliation methods can normally be dispersed homogeneously in solvents and form colloidal suspension of 2D materials, which allows the assembly of 2D material-based heterostructures on a large scale. By using homogenous liquid dispersions of 2D materials, a variety of strategies can realize

the LBL assembly of heterostructures more efficiently. These include alternating Langmuir-Blodgett (LB) film transfer, dip coating, spin coating, and spray coating. These LBL assembling approaches not only balance simplicity, productivity, and cost, but can also tune the thickness of heterostructures precisely. For example, Gogotsi's group realized the scalable manufacturing of MXene/graphene lamellar heterostructures by a simple spray coating method.[24] The arrangements of two components and the thickness in obtained heterostructures can be easily manipulated by modulating the concentration of individual components in precursor solutions, flow volumes, and repetition times, respectively.

Although these methods mentioned above are universal for heterostructure assembly, it is still challenging to achieve high-order LBL heterostructures because of lacking the direct interaction force between the constituent materials. Self-assembly relying on electrostatic attraction is a scalable approach to realize ordered assembly of heterostructures. But the surface modification of nanomaterials is a prerequisite to creating an opposite charge-inducing interaction between two individual building blocks. After the self-assembly process, subsequent treatment is usually employed to lock the architecture in heterostructures, such as vacuum infiltration and freezing drying.[25-27] As shown in **Figure 1.2b**, Xie *et al.* fabricated flexible $Ti_3C_2T_x$/carbon nanotubes (CNTs) composite paper by using this route, in which CNTs were first grafted with a cationic surfactant cetyltrimethylammonium bromide (CTAB) and then can be attracted by the negatively charged MXene nanosheets.[22] Generally, the solution-based mechanical assembly technique for constructing heterostructures is preferable for large-scale applications because of the low cost, accessible conditions, and simple processing steps. More importantly, it is also universal for the assembly of the nanomaterials with distinct properties because no lattice matching is required. Nevertheless, there are still problems

regarding this method, including unclean interfaces due to the introduction of surfactants and a relatively low overall yield. The potential solutions to the former are adopting suitable solvents for deep cleaning or using calcination or radiation techniques to remove the surfactants. As for increasing yield, that is powerfully relevant to the production of 2D material monomers. Effective exfoliation methods should be investigated and promoted in the future.

1.1.3 *In-situ* growth processing

In-situ growth is another route to construct heterostructures, which enables robust and clean interfaces/heterojunctions because the second material grows directly on specific crystalline facets of the first material. Numerous techniques have been developed to prepare the 2D material-based heterostructures including chemical vapor deposition (CVD), atomic layer deposition (ALD), wet-chemical methods. CVD is a traditional technique for preparing pure materials and thin films on substrates.[28-30] It is also a reliable method for *in-situ* synthesizing 2D material-based heterostructures. Duan and co-workers demonstrated a universal CVD method to synthesize 2D monolayer heterostructures, multi-heterostructures, and superlattices (**Figure 1.2c**).[23] During this process, specifically, a cycled gas atmosphere is applied to support the homogeneous nucleation and growth at the initial synthesis stage of 2D crystals. Subsequently, the configurations of 2D heterostructures can be well-controlled with different CVD steps. However, lattice compatibility or catalysis on the specific substrate is imperative for growing a second material on pristine 2D materials. Metal dichalcogenide-based heterostructures are one kind of 2D heterostructures that have been synthesized principally by CVD methods. These include GaSe/$MoSe_2$, WS_2/MoS_2, ReS_2/WS_2, and MoS_2/graphene, *etc*.[31-34] Notably, the configuration of the heterostructures can be well controlled by simply changing synthetic parameters, including gas-flow rates and

temperature. Li *et al.* reported the CVD growth of 2D GaSe/$MoSe_2$ heterostructures with a large lattice misfit. Interestingly, GaSe could either grow vertically or laterally on horizontal $MoSe_2$ nanosheets under different Ar flow.[31]

ALD is an alternative choice to perform *in-situ* growth of heterostructures with atomic-scale precision. Thanks to the unique mechanisms of surface self-saturated reactions, ALD is advantageous in terms of thickness control and conformality.[35] Herein, the sequential layer-by-layer ALD technique promotes the production of finely manipulated nanostructures at the atomic scale with desired properties. For instance, Ahmed *et al.*[36] prepared HfO_2 coated SnO_2/MXene by depositing SnO_2 onto the surface of MXene nanosheets and subsequent coating of a HfO_2 layer onto the former composite via a two-step ALD process. The heterojunctions between SnO_2 and MXene nanosheets can restrict volume expansion during electrochemical reaction and effectively increase the electrical conductivity of materials. A thin passivation layer of HfO_2 was also shown to be useful by acting as an artificial SEI film in lithium-ion batteries.

The wet-chemical method, including solution-processing, hydrothermal and solvothermal reactions, is one of the frequently used approaches for in-situ construction of complex heterostructures, such as 1D forests/2D nanoarrays on substrates and 3D hierarchical assemblies.[37] Typically, one material is used as a template, and a soluble precursor of another heterostructure component directly reacts on the template surface to form the final product. It is important to note that the affinities between templates and soluble precursors should be strong enough to ensure the reaction preferentially occurs on the template surface rather than forming separate-product particulates.[38] Qiu's group coupled various layered nanomaterials (MoS_2, FeNi-LDHs) vertically onto MXene nanosheets by one-pot co-deposition methods.[39-41] Surface functional groups of MXenes

offer active sites for the absorption of transition metal ions. A subsequent co-deposition process contributes to the strong interfacial coupling, excellent structural stability, and good electronic conductivity. In addition to integrating different components into hybrid architectures, substrate materials can also self-assemble into 3D interconnected networks during *in-situ* growth processes.[42,43] For example, rich surface groups-terminated graphene and MXene nanosheets can self-assemble into 3D networks with the support of induced metal cations to synthesize heterostructures.[44,45]

In general, the aforementioned *in-situ* growth methods can result in clean and robust heterointerfaces, thereby realizing highly efficient electron transfer and further facilitating electrochemical kinetics. Nevertheless, the CVD and wet-chemical approaches require preconditions such as a good lattice match or additional induced forces, which hinder their extensive applications. Besides these methods, the ALD technique is more suitable for modifying materials rather than mass production of heterostructure materials for rechargeable batteries, owing to its low efficiency and high cost.

1.2 Structural Features in Different Dimensionalities

2D nanomaterials have been intensively used as building blocks to prepare heterostructures due to their unique physical and chemical properties. In particular, the high aspect ratio offers multiple active sites for anchoring or growing a second component with different dimensionalities, such as 0D nanoparticles, 1D nanotubes/fibers, or 2D nanosheets/nanoplates. For these heterostructures comprising anisotropic materials, the presented structural features closely correlate to the original structural types of the two constituents. Besides, the same building blocks also possess different geometric configurations when forming heterostructures. For instance, 1D nanofibers can either

grow vertically on a 2D horizontal plane *via* covalent bonding or arrange parallel to the 2D plane *via* vdW forces. These heterostructures with different configurations have distinct heterointerfaces, which would alter the corresponding properties in turn, such as mass transportation and electron transfer capability. Therefore, understanding the basic structural features is imperative for us to design high-performance 2D material-based heterostructure materials according to the specific requirements from targeted materials for rechargeable batteries.[46] In this section, we classify and present the structural characteristics of 2D material-based heterostructures based on the dimensionalities. We also discuss the advances and limitations of each configuration in the context of battery applications.

1.2.1 2D-low dimensional heterostructures

When 2D nanomaterials are combined with 0D nanoparticles, such as quantum dots (QDs), the 2D nanomaterials usually act as substrates, which can inhibit the aggregation of nanoparticles, enhancing electron transfer and suppressing volume change of nanoparticles during electrochemical reactions.[47,48] Graphene and MXenes are two examples that are usually used as substrates in 2D-0D heterostructures due to their relatively high specific surface area (SSA) and excellent electronic conductivity. For example, MXenes have been employed as substrates for numerous electrochemically-active materials, including transition metal oxides,[36] sulfur, and silicon nanoparticles, which have high theoretical capacities but low conductivity. In hybrid heterostructures, nanoparticles have intimate interfacial contact with 2D materials *via* either strong covalent bonds or weak vdW interaction. Nazar's group[49] coupled sulfur on the surface of Ti_2C based on the chemical absorption of S atom by Ti atom, which contributed to both the enhanced conductivity and improved retention of polysulfides when applied in Li−S batteries. Hui *et al*.[50] reported Si/MXene heterostructures in which Si nanoparticles are

uniformly anchored on MXenes surface *via* Si−O−Ti bonds (**Figure 1.3a**). Such heterostructure design suppresses volume expansion and aggregation of Si nanoparticles and enhances electron transfer kinetics when apply in rechargeable batteries.

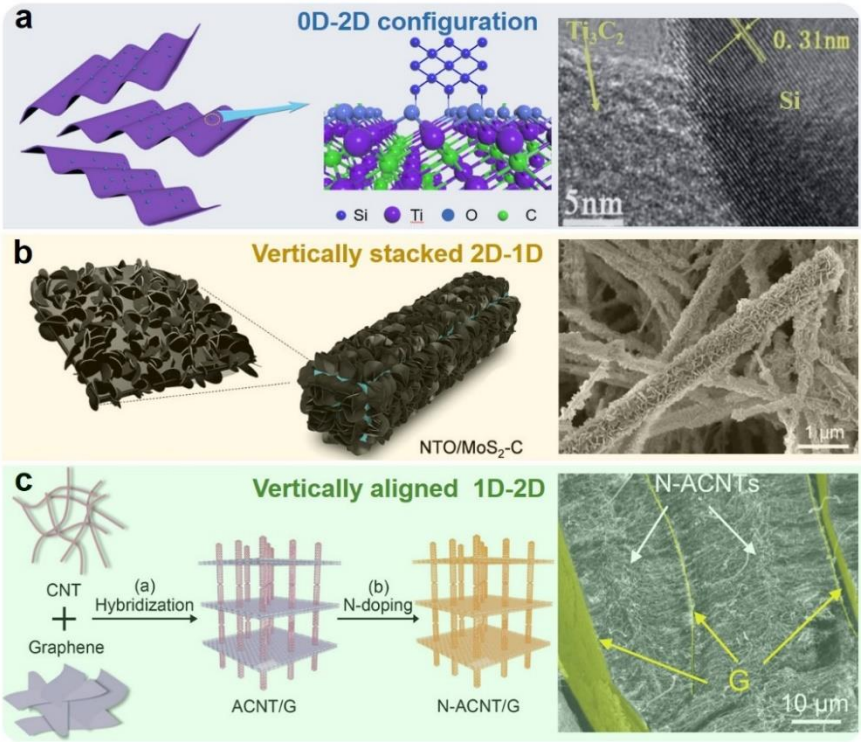

Figure 1.3 Structural features of heterostructures constructed from 2D nanomaterials and low-dimensional nanomaterials. 0D-2D configuration: a) Schematic illustration of the synthesis of bridging between the Ti_3C_2 nanosheets and Si nanoparticles in Si/Ti_3C_2 0D/2D heterostructures with TEM image.[50] Vertically stacked 2D-1D: b) Schematic illustration and SEM image of NTO/MoS_2-C nano-architectures.[51] Vertically aligned 1D-2D: c) Schematic of the synthesis procedures and SEM images of N-ACNT/G hybrids.[52]

Nanoparticles can also be encapsulated by 2D nanosheets to form core-shell heterostructures, thanks to the good flexibility of 2D nanosheets. Typically, outer layer 2D nanosheets will stick to the nanoparticle surfaces *via* vdW forces or electrostatic attractions. As a result, the volume expansion of nanoparticles can be confined by the 2D

nanosheet “shell”, which can improve electrode structural stability. Guo *et al*.[53] prepared $Ti_3C_2T_x$ encapsulated TiO_2 nanospheres as high-performance anodes for sodium-ion batteries. The MXene layer enhanced electronic conductivity, suppress the volume change, maintain the integrity of the electrode, and contribute to the formation of a stable SEI layer.

2D-1D heterostructures have more possible configurations, owing to their anisotropic geometries. Their architectures can be divided into vertical and parallel stacking formats, with the former mainly depending on covalent bonds and the latter mostly resulting from vdW forces. Vertical stacking structures can be 1D nanomaterials directly grown on the surface to form a forest on the 2D plane or 2D nanosheets deposited onto 1D nanomaterials to obtain arrays. As shown in **Figure 1.3b**, Wang *et al.* fabricated a core-shell NTO/MoS_2-C hierarchical nanohybrid, in which 1D sodium titanate (NTO) nanowires act as core substrate and 2D MoS_2 coupled by carbon nanosheets (MoS_2-C) are vertically aligned on nanowires.[51] In this configuration, the MoS_2 sheet arrays normally have a lateral size smaller than the diameter of the NTO nanowires. When applied as battery electrode materials, these rigid NTO nanowires enhance structural stability and ionic diffusion, while MoS_2 promotes ion storage and thus increases specific capacity.[54] Numerous similar heterostructures have been successfully fabricated, including WS_x/WO_3 thorn-bush nanofibers[55] and Mn_3O_4@H-TiO_2.[56] In contrast, if the lateral sizes of 2D nanosheets are much larger than those of 1D nanomaterials, 1D forests could stand vertically on the basal plane of 2D nanosheets. Such a nanostructure enables a high SSA by suppressing the aggregation of nanomaterials. Besides these aspects, there are also tunable free spaces inside the nanoarrays, which play an important role in regulating internal stresses generated from volume expansion. Nevertheless, the loading density of 1D nanomaterials on 2D substrates is not high and may limit volumetric

capacity when these materials are employed as electrode materials. Sometimes vertically-aligned 1D nanomaterials can bridge adjacent nanosheets, resulting in 3D hierarchical architectures with tunable porosities and enhanced electrons transfer pathways. For instance, Tang *et al.*[52] prepared nitrogen-doped aligned CNT/graphene sandwiches (N-ACNT/G hybrids) with aligned CNTs and graphene sheets growing vertically to each other with a long-range periodicity (**Figure 1.3c**).

Parallel configurations between 1D and 2D nanomaterials are commonly constructed by self-assembly methods in solution. The incorporation of 1D materials can prevent the restacking of 2D nanosheets during electrode fabrication and endow accessibility to 2D material active sites. Furthermore, some electrochemically active 1D materials can provide extra capacity for energy storage. For example, Xu *et al.* fabricated hybrid anodes comprising 1D transition metal oxide (TMO) nanostructures (TiO_2 nanorods and SnO_2 nanowires) parallel to the MXene basal planes for lithium storage.[57] The MXene substrate promotes electron transfer at the interface and inhibits the aggregation of TMOs. Simultaneously, the restacking of MXene nanosheets can be avoided by the TMO spacers. Except for extremely parallel architectures, core-shell structures with 1D nanostructures encapsulated by 2D flexible nanosheets have also been prepared through self-assembly processes.[58] In such architectures, 2D nanomaterials can physically restrain volume expansion and contribute to the good structural stability of the electrodes.[59]

1.2.2 2D-2D heterostructures

2D-2D heterostructures (usually called 2D heterostructures) have been extensively investigated for diverse applications owing to their extraordinary properties. When various 2D nanomaterials are hybridized into heterostructures, three types of connection between nanosheets can be realized: edge-to-edge, edge-to-face, and face-to-face

heterojunctions. The structural features and properties of heterostructures vary with these different kinds of heterojunctions.

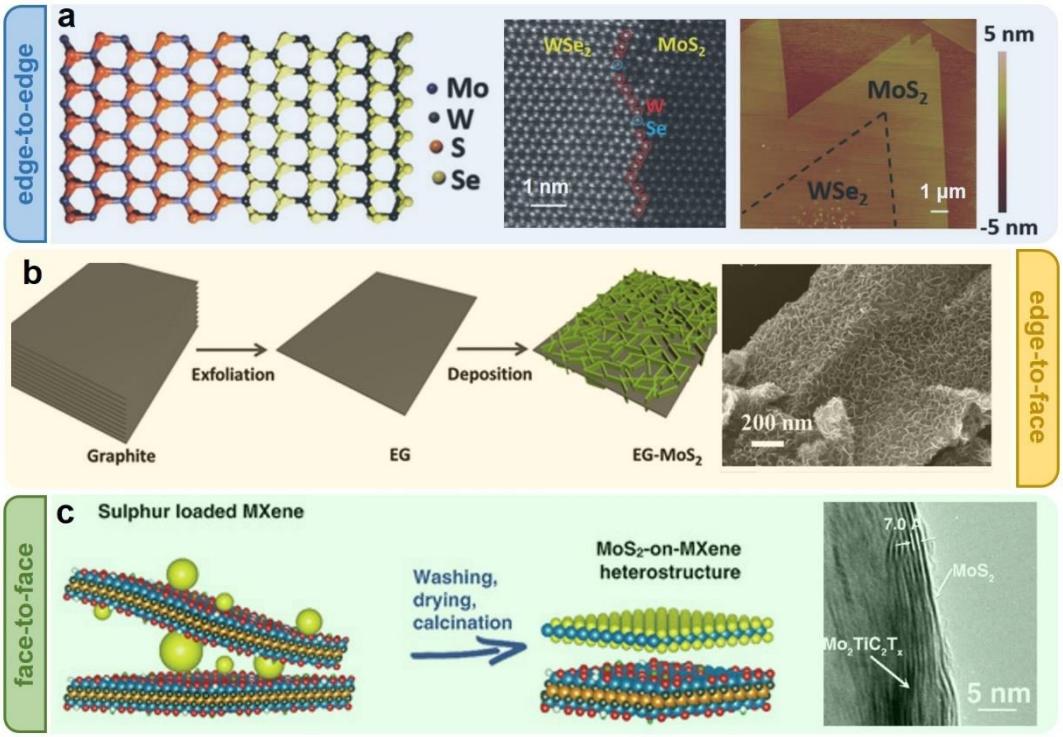

Figure 1.4 Structural features of 2D/2D heterostructures displaying different configurations and heterostructure engineering. Edge-to-edge: a) Schematic, high-resolution STEM image, and AFM image of monolayer WSe_2-MoS_2 lateral heterostructure.[60] Edge-to-face: b) Schematic illustration of preparation procedures and SEM image of vertically aligned EG-MoS_2.[61] Face-to-face: c) Schematic illustration of the preparation procedures and cross-sectional TEM image of MoS_2-on-MXene heterostructures.[62]

Horizontal in-plane heterostructures contain at least two different 2D nanosheets stitched together at the edge, whereby a strong edge-to-edge heterojunction forms through covalent bonds. Li *et al.*[60] demonstrated a vdW epitaxy technique and prepared monolayer WSe_2-MoS_2 lateral heterostructures, in which an atomically sharp interface between WSe_2 and MoS_2 was observed (**Figure 1.4a**). Due to small lattice mismatch

between the transition metal dichalcogenide (TMD) families, such edge-to-edge heterostructures are common and easy to fabricate (*e.g.*, WS_2, MoS_2, $MoTe_2$).[32,63] Meanwhile, the resulting lateral heterostructures are nearly pristine with few defects at the heterojunction, which makes it possible to manipulate bandgap and electron transfer between the different components.

Compared to edge-to-edge heterostructures that typically yield a high degree of lattice matching, edge-to-face heterostructures are more easily to be prepared using a wide variety of 2D nanomaterial species. Recently, vertically-aligned nanosheets on 2D conductive substrates have been intensively reported, such as exfoliated graphene (EG)-MoS_2.[61] MoS_2/Ti_3C_2 MXene heterostructure,[39,64] layered double hydroxides (LDHs) arrays/MXene nanohybrids,[40,41] and v-ReS_2/rGO nanocomposite.[65] With a perpendicular orientation of the 2D components, the obtained 3D architectures exhibit tunable porous microstructures with high SSA, which is favorable for the penetration of electrolytes and storage of ions.[66] MoS_2 is a typical 2D metal chalcogenide with promising theoretical capacity, but it has moderate electronic conductivity and easily restacks, which hinders its practical application. Herein, MoS_2 is usually coupled with highly conductive substrates into heterostructures to optimize its electrochemical performances. Recently, Feng's group[61] reported a 3D EG-MoS_2 network, in which vertical MoS_2 nanosheets are controllably patterned onto the basal plane of EG (**Figure 1.4b**). The heterojunctions between EG and MoS_2 nanosheets contribute to intimate contact, resulting in fast charge transport kinetics and high mechanical integrity, respectively. Similarly, Wang and co-workers[64] employed Ti_3C_2 MXene as conductive substrates for 1T-MoS_2 to construct a 3D interconnected heterostructure, which realized extra capacitance and outstanding rate performance due to the enlarged ion storage space and ultrafast electron transport originating from Ti_3C_2 MXene.

Although the aforementioned two configurations possess several merits, some problems still exist, such as the low capacity for mass loading of active materials and limited portion of heterojunctions/interfaces. The face-to-face alignment between 2D nanomaterials can maximize the contacting area of heterointerfaces and thus modulate the overall electronic structure of hybrid materials. It is worth noting that the order of 2D materials stacking in lamellar heterostructures is important because it may change the properties accordingly. The construction of face-to-face 2D heterostructures has been extensively reported, using the to various 2D nanomaterials, such as black phosphorus (BP), TMOs, TMDs, graphene and analogs,[67,68] *etc*. Electrostatic attraction-induced self-assembly can be used to fabricate alternative stacking of 2D nanosheets on a large scale and obtain lamellar superlattice heterostructures. Xiong and co-workers fabricated several different superlattices via this strategy, including 1T-MoS_2/graphene, $Ti_{0.87}O_2$/nitrogen-doped graphene, MoS_2/NiFe-LDH, and $VOPO_4$/graphene.[69-72] A second 2D material (*e.g.*, MoS_2, $Ti_{0.87}O_2$, $VOPO_4$) can be restrained between two layers (or inside a fold) of a first 2D material (graphene, nitrogen-doped graphene). A robust heterointerface can effectively modulate the strain generated by the intercalation/deintercalation of either monovalent ions (Li^+, Na^+) or multivalent ions (Zn^{2+}, Al^{3+}).

In addition to stacking order, the chemistries at heterointerfaces also influence the overall properties of heterostructures, especially when considering contaminations that might be induced by surface modification steps prior to the main self-assembly step. A clean heterointerface contributes to intimate contact between the components and thereby promotes electron transfer. Chen *et al*.[62] demonstrated MoS_2-on-MXene heterostructures with clean interfaces by *in-situ* sulfidation of $Mo_2TiC_2T_x$ MXene (**Figure 1.4c**). Theoretical calculations revealed that the hybrid material is metallic, which can be

assigned to the heterointerface formed by direct contact between MoS_2 and highly conductive MXene.

1.3 Heterostructure Engineering

Beyond the advances mentioned above, the properties of heterostructures can be further optimized to meet the requirements of specific applications. These strategies include surface chemistry engineering (or interface engineering) and defect engineering, which directly influence electrical properties, stabilities, and lattice parameters of the heterostructures.[73,74] The comparison of two strategies were listed in **Table 1.1**.

Table 1.1 Advantageous and disadvantageous of surface chemistry engineering (interface engineering) and defect engineering.

	Surface chemistry engineering (Interface engineering)	Defect engineering
Advantageous	• Tuning surficial/interfacial properties, like ionic transport, surface reactivities, charging states, *etc.* • Easy operation in liquid/solution phases • Numerous choices of surficial/interfacial covalent groups	• Adjusting intrinsic physicochemical properties, like crystal structure, chemical stability, electronic conductivity, *etc.* • Accurate control of defect concentrations and types • Permanent change to the modified materials
Disadvantageous	■ Low depth of	■ Complicated in operation,

	modification in materials ■ Poor resistance to the group exchange or corrosion	mostly via solid-state method at high temperatures

1.3.1 Surface chemistry engineering

Surface chemistry engineering of 2D material-based heterostructures mainly includes covalent surface functional group regulation and surface coating. Surface functional groups usually exist on the surface of 2D nanomaterials, especially for those synthesized by liquid-exfoliation methods (such as MXenes and graphene analogs). The constituents of these functional groups considerably influence the physical and chemical properties of 2D materials.[75,76] A typical example is the 2D $Ti_{n+1}C_nT_x$ MXenes (T_x represents surface groups, such as −F, −OH, −Cl, −Br…), which show distinctive structural and electronic properties according to different surface terminations obtained.[77] Theoretical calculations revealed that the −OH and −O terminated MXenes possess different theoretical capacities and diffusion kinetics for alkali ion storage (**Figure 1.5a, b**).[78] Thus, modulating the properties of heterostructures can be achieved through tuning the surface chemistries of the individual building blocks. The methods for controlling the surface chemistries of pristine 2D materials and their impacts on electrochemical applications have been reported in the previous reviews.[79,80] For example, we recently constructed 2D phosphorene/$Ti_3C_2T_x$ MXene heterostructures by integrating F-rich MXene with phosphorene.[81] In-depth X-ray photoelectron spectroscopy analysis revealed that the fluorine terminations at the interface modulated the formation of SEI films by forming F-rich compounds on the anode surface.

Beyond pre-tuning the individual 2D constituents, the surface chemistries of heterostructures can also be controlled through additional post-treatment of the materials.

Xie *et al.* soaked rGO/$Ti_3C_2T_x$ films in 1 M HCl solution to increase the hydroxyl groups on the hybrid film and thereby facilitated water flux within the film (**Figure 1.5c**).[82] This also demonstrates that the surface groups of heterostructures closely affect the interactions at solid/liquid interfaces, which is important for electrochemical energy storage. Therefore, 2D material-based heterostructures with versatile surface chemistries offer a promising platform to improve electrochemical performance through modulating the reactions occuring on SEIs in rechargeable batteries.

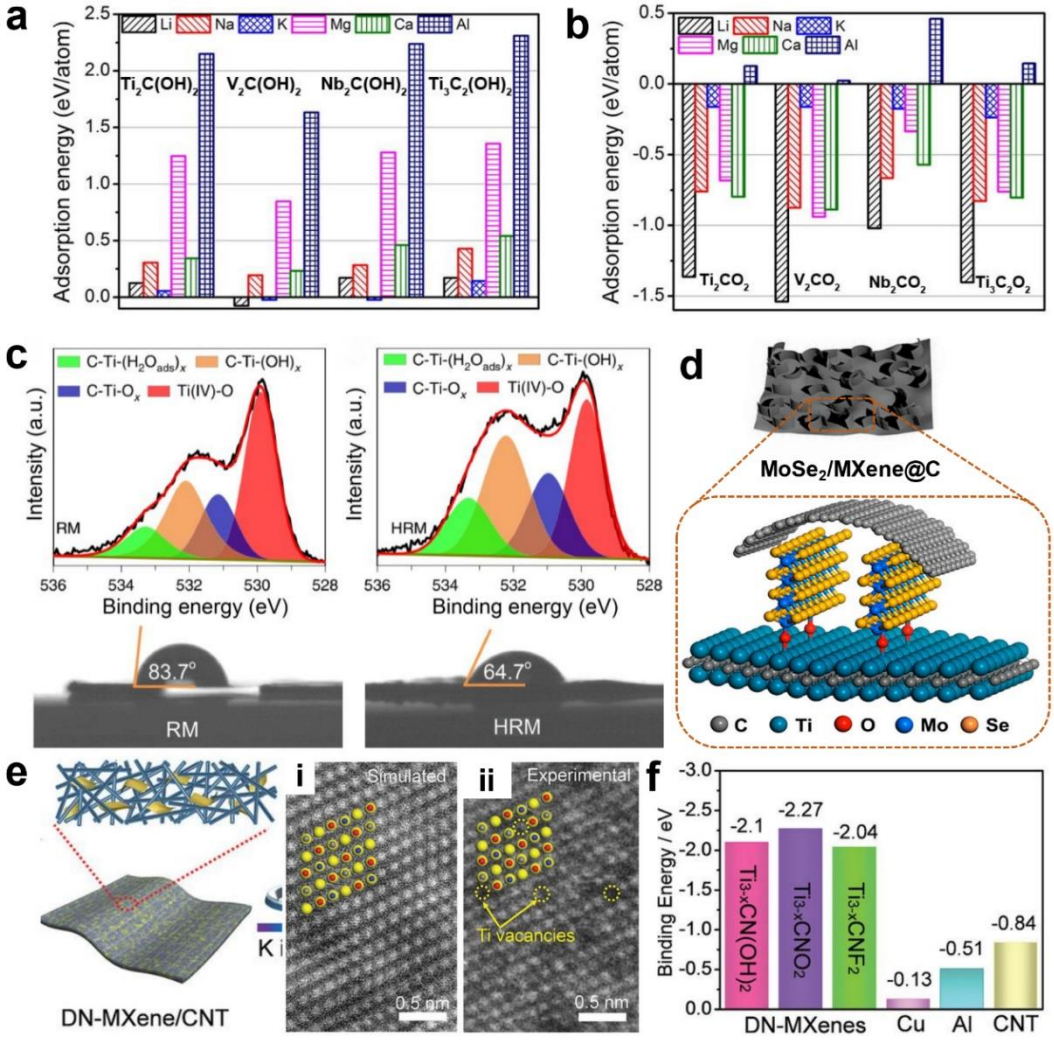

Figure 1.5 Surface chemical engineering and defect engineering of heterostructures. Ion adsorption energies for MXene nanosheets terminated by (a) −OH and (b) −O.[78] (c) Effect of changing functional groups on surface wettability of the RGO/MXene

heterostructure film.[82] (d) Schematic of carbon-coated $MoSe_2$/MXene heterostructure.[83] (e) Schematic illustration of the DN-MXene/CNT scaffold; (i) and (ii) are the simulated and corresponding experimental atomic-resolution HAADF-STEM images of the DN-MXene sheets; Ti: yellow atoms, C: grey atoms, N: blue atoms, Ti vacancy: circles, surface groups: red atoms. (f) The calculated binding energies of K atoms with different scaffolds or current collectors.[84]

Surface coating is another strategy to enhance the electrical conductivity, structural stability, and chemical stability of heterostructures. Carbonaceous materials are widely used for this purpose because of their low cost, easy-fabrication, high stability and good conductivity. For example, Qiu's group developed a carbon nanoplating strategy to decorate a MoS_2/Ti_3C_2 MXene heterostructure, which not only protected Ti_3C_2 MXene from degradation under high-temperature treatment, but also presented synergistic effects for lithium storage.[85] Similarly, Huang *et al*. recently prepared a $MoSe_2$/MXene heterostructure, in which the $MoSe_2$ nanosheets are vertically anchored on the MXene substrate to form a hierarchical 2D nanosheets structure. Subsequently, carbon coating was performed to reinforce the hierarchical 2D heterostructure and further enhance the conductivity of the hybrid structure (**Figure 1.5d**).[83]

1.3.2 Defect engineering

Defect engineering introduces structural/lattice disorder, leading to a change of both the lattice parameters and electronic structures of the materials. Several defect engineering strategies have been reported, including hetero-atom doping, atom substitution, and creation of atomic vacancies, *etc.* Similar to surface chemical engineering, heteroatom doping, or vacancy creation can be done both before or after the formation of heterostructures. Up to now, most of the relevant research works construct

defects or vacancies on the individual building blocks first and then fabricate them into heterostructures to modulate the overall properties. This route can concisely control defects on each constitute of the heterostructures. Post-treatment can also achieve precisely defect engineering if the two components of the heterostructure have distinct reaction activities.[86]

Both metallic atoms (Fe, Co, Ni, Pt, *etc.*) and non-metallic atoms (B, O, F, S, P, N, *etc.*) can be used as dopants to increase the electrochemical activity of 2D materials. Metallic doping or substitution has typically been used to improve electronic conductivity and accelerate electrochemical reaction kinetics.[87] For example, single Pt atoms can be immobilized on the surface of $Mo_2TiC_2T_x$ MXene by occupying Mo vacancies that are generated in the electrochemical exfoliation process. Such a substitution results in a higher Fermi level and lower work function of $Mo_2TiC_2O_2$-Pt_{SA}, indicating higher electronic energy levels and an improved capability to provide electrons.[88] Non-metallic doping and atomic vacancies can effectively change electrochemical properties such as diffusion kinetics and absorption energies. These materials could deliver the extra capacity for energy storage due to the enlarged interlayer spacing, enhanced electrochemical reactivity, and high surface polarity.[89,90] By utilizing the appreciable potassium-philic features of defect-rich $Ti_{3-x}CNT_y$ MXene, we recently developed dendrite-free potassium anodes by confining potassium metal in a porous $Ti_{3-x}CNT_y$/CNT heterostructure film (**Figure 1.5e**).[91] Theoretical simulations demonstrated that the defective $Ti_{3-x}CNT_y$ with higher binding energy is favorable for uniform potassium plating/stripping (**Figure 1.5f**). Nevertheless, it is worth noting that defect ratios in the heterostructures should be optimized to maximize the electrochemical performance because the electrical conductivity usually decreases along with an increased number of vacancies.

1.4 The Roles of Heterostructures in Rechargeable Batteries

The applications of 2D material-based heterostructures have been applied in diverse energy storage systems, such as alkali-ion batteries, multivalent-ion batteries, and alkali-sulfur batteries. Electrochemical properties (high specific capacities, good rate performance, and stable long-term cycling life) can be enhanced by the introduction of heterointerfaces, synergistic effects between configurations, and mechanical confinement by 2D substrates. Here, we illustrate the functional roles of 2D material-based heterostructures in rechargeable batteries.

1.4.1 Facilitating charge transfer

The charge transfer capability of electrode materials is critically important in rechargeable batteries. An enhanced charge transfer reduces the electron and ion transportation resistance in electrodes, thus facilitating the electrochemical reactions of electrode materials. Most 2D electrode materials have high charge transfer kinetics owing to their unique planar layered structures. Benefiting from this feature, 2D materials and the derivative 2D material-based heterostructures show overwhelming superiority in electrochemical activities and rate capabilities in alkali-ion batteries.

Typically, charge transfer can be directly quantified via physical approaches, especially Hall effect measurements. Subsidiary properties, like electronic and ionic conductivities, contribute to charge transfer kinetics in energy storage systems and are often measured by electrochemical characterizations. Luo *et al.* pressed 0D-2D Ni_2P@BP heterostructure powders into pellets for the measurement of electrical conductivity and charge carrier concentration using a physical properties measurement system (PPMS, Quantum Design).[92] As shown in **Table 1.2**, compared with BP single crystals and BP nanosheets, Ni_2P@BP heterostructures exhibit much higher charge carrier concentrations and

electrical conductivity at room temperature, as well as an enhanced Li-ion migration capability (the diffusion coefficient calculated from CV profiles under various scanning rates).

Table 1.2 Electrical conductivities, charge carrier concentration, and Li^+ diffusion coefficient of BP single crystal, BP nanosheets, and Ni_2P@BP heterostructures.[92]

	Electrical conductivities ($S\ m^{-1}$)	**Charge carrier Concentration** (cm^{-3})	**Li^+ diffusion Coefficient** ($cm^2\ s^{-1}$)
BP single crystals	1.10×10^3	5.00×10^{17}	
BP nanosheets	2.12×10^2	1.25×10^{17}	1.14×10^{-14}
Ni_2P@BP heterostructures	6.25×10^4	1.37×10^{20}	8.02×10^{-13}

However, the electrochemical techniques for measuring ionic transport inside cells are influenced by a plethora of other configurations, such as electrolytes, counter electrodes, current collectors, and additives, *etc*.[93] Meanwhile, the inevitable particle gaps and boundary barriers reduce the accuracy of electrical conductivity and Hall effect measurements in pressed pellets. Therefore, atomic-level observations and measurements of charge transfer in heterostructures are strongly required.

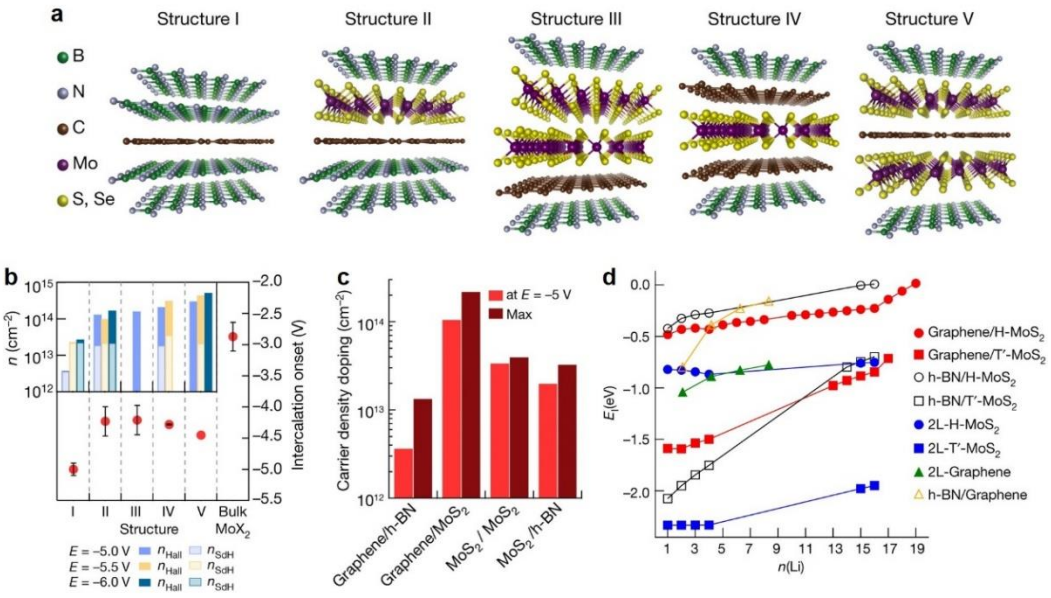

Figure 1.6 Charge transfer in vdW heterostructures. a) Atomic models of the heterostructure series used for investigating the effects of heterolayers on intercalation capacities and thermodynamics. b) Intercalation onset potentials of vdW heterostructures and bulk MoX_2. Inset, mean charge densities after intercalation. n_H, indicative of the total density, is depicted by the overall bar height, and graphene partial densities from SdH data (where available) are indicated by the lighter sub-bars. c) Estimated doping level of vdW interfaces. d) Computed lithium-atom binding energy as a function of the number of lithium atoms in the supercell.[94]

Recently, Bediako *et al.* thoroughly investigated the electronic and ionic charge accumulation behaviors in vdW heterostructures through both experimental investigations and theoretical calculations.[94] They constructed five types (structure I to V) of individual vdW heterostructures (**Figure 1.6a**) on micro-electrochemical cells, which were built from monolayer graphene and a molybdenum dichalcogenide (MoX_2) with insulating hexagonal boron nitride (*h*BN) encapsulation. These unique architectures bring convenience to study the *in-situ* Li^+ and electron transport during the intercalation process. Several important findings have been revealed. These include: (i) The charge

transfer preferably occurs on the MoX_2 layers rather than graphene counterparts in various graphene/MoX_2 heterostructures. As shown in **Figure 1.6b**, from low-temperature magnetotransport measurements, the maximum charge density distribution on graphene layers (n_{SDH}) was found to be only 2×10^{13} cm^{-2}, at least ten times lower than the charge transfer on MoX_2 layers (3×10^{14} cm^{-2}). (ii) Graphene heterolayers play an essential role in facilitating charge accumulation at MoX_2 layers. The maximum carrier density doping (**Figure 1.6c**) in a graphene/MoS_2 heterointerface attains the highest value compared to other heterointerfaces like MoS_2/MoS_2 and MoS_2/h-BN. (iii) The electrochemical enhancement of MoS_2/graphene/MoS_2 heterostructure (structure V) is also presented on the remarkable reduction of Li^+ intercalation onset voltage with a decreased potential by 0.25 V compared to other heterostructures (structure II to IV). From *in-situ* TEM observation and calculation, this is ascribed to the strain introduced phase transformation from semiconductor H- to metallic T'-phase induced by Li^+ intercalation into graphene/MoX_2 heterointerfaces, which results in a lower activation barrier (**Figure 1.6d**) for Li^+ insertion into T'-MoX_2. Consequently, Li^+ transfer capability has been improved in graphene/MoX_2 heterointerfaces.

Furthermore, various theoretical calculations have been concluded to demonstrate how the coupling effect triggers the interfacial electronic structure changes in a number of 2D material-based heterostructures, such as TMDs/graphene,[95-97] TMOs/graphene,[98] phosphorene/graphene,[99,100] C_3N_4/graphene,[101] TMDs/MXene,[102-104] GeSe/black phosphorus,[105] and TMDs/TMDs,[106] *etc*. Bader charge analysis is the most straightforward and commonly used theoretical method to study the charge transfer behaviors in heterostructures. The calculated values can indicate the gain or loss of electrons at certain atomic layers, reflecting the charge states as well as the charge transfer abilities. The charge transfer capability in intrinsic 2D material-based heterostructures is

highly relevant to the hetero-interfacial combinations, typically behaving as physical adsorption (vdW force) or covalent binding between components. Generally, stronger hetero-combinations show better charge transfer performance. For example, in the system coupled with TMDs, silicene loses more electrons than graphene because of a weak covalent bond between Si and TMDs rather than vdW interaction as graphene and TMDs. Similarly, among a series of TMDs/graphene heterostructures, SnS_2/graphene exhibits better charge transfer ability (−0.0043 |*e*| per C atom) than MoS_2/graphene (−0.0009 |*e*| per C atom) due to the higher covalent percentage in ionic Sn−S bonds owing to the weaker metallicity of Sn elements.[96] Furthermore, some other indicators, such as the rearranging of band structures and charge redistribution at heterointerfaces, were also applied to study the influence of charge transfer qualitatively.

Beyond theoretical calculations, the work function of semiconductors, namely the minimum energy of electron transport from Fermi level to an infinite distance, can be directly evaluated by experimental measurements, such as ultraviolet photoelectron spectroscopy (UPS). Based on the UPS results (**Figure 1.7a**), the work function of $NiTe_2$ (5.69 eV) and ZnTe (4.61 eV) can be calculated from the work function equation:

$$W_f = hv - |E_{sec} - E_{FE}|,$$

where hv is to the energy of the light source, E_{sec} and E_{FE} are energies of secondary-band edge and Fermi edge, respectively.[107] Therefore, a $NiTe_2$-ZnTe heterostructure has an internal electron flow from ZnTe to $NiTe_2$ due to the upward bending of the ZnTe band at the heterointerface (**Figure 1.7b**). The overall effect of this is that a built-in electric field originates from the *p*-*n* heterojunction.

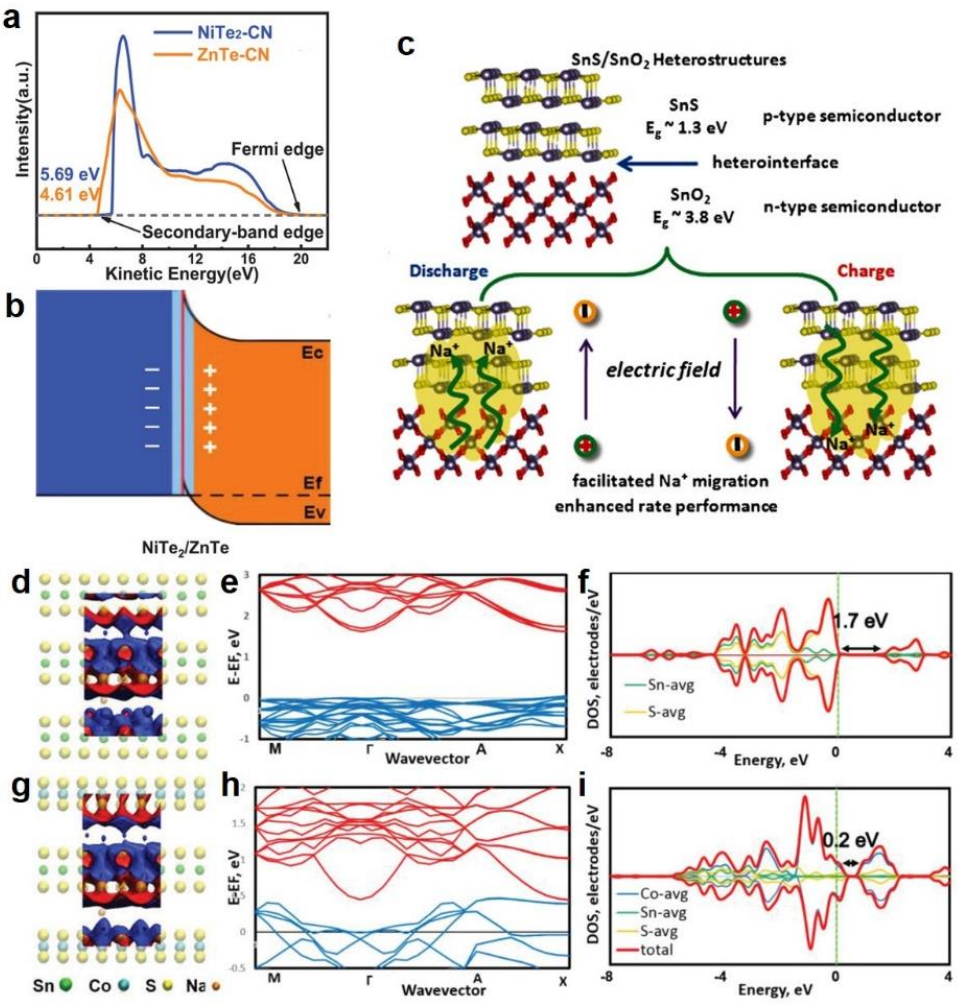

Figure 1.7 Built-in electric field at heterointerfaces. a) UPS spectra of $NiTe_2$–CN and ZnTe–CN (the Fermi edge was unified to 21.1 eV). b) schematic illustration of the $NiTe_2$/ZnTe anti-blocking heterointerface.[107] c) Schematic illustration of the induced built-in electric field in SnS/SnO_2 heterostructures.[108] Distributions of charge density difference (+ and – induced charges are represented in blue/red solid spheres, respectively): d) SnS_2; g) (SnCo)S_2; band structures (spin down α): e) SnS_2; h) (SnCo)S_2; electronic DOSs: f) SnS_2 and i) (SnCo)S_2.[109]

Guo's group demonstrated this effect in an SnS/SnO_2 heterostructure (**Figure 1.7c**).[108] SnS has a narrow bandgap of 1.3 eV, functioning as *p*-type semiconductor when coupled with the wide-band-gap (3.8 eV) *n*-type semiconductor SnO_2. During the discharge process, there is an internal electric field across the heterointerfaces, pointing across the

junction from the *n* region to the *p* region. Under the influence of the built-in electric fields, ionic conductivity is also strengthened. We further expanded this hypothesis from 2D-2D heterostructures to 1D-2D heterostructures, like SnS_2/Sb_2S_3@rGO composites, in which 1D Sb_2S_3 nanorods embedded on rGO nanosheets are covered by *in-situ* grown 2D SnS_2 nanoflakes with lattice dislocations.[110] Based on the results from the galvanostatic intermittent titration technique (GITT) during sodiation/desodiation, the SnS_2/Sb_2S_3@rGO composites displayed an overall Na^+ diffusion coefficient superior to SnS_2@rGO composites. This phenomenon benefits from the existence of micro-sized internal electric fields across the heterointerfaces, which enhance electron transfer from Sb_2S_3 to SnS_2, and subsequently result in an increased charge collection as well as Na^+ aggregation on the electrolyte-exposed SnS_2 surface during the discharge process. These effects may give rise to an enhanced diffusion coefficient. Fick's first law dictates that the boosted Na^+ concentration gradient will lead to an increased flux of Na^+ ions.

Recently, the effect of a built-in electric field on 0D-2D heterostructures was also studied. The MnS-MoS_2 heterostructures with 0D MnS nanoparticles coupled with 2D MoS_2 nanosheets exhibited a significantly increased ionic diffusion coefficient of 10^{-14}~10^{-13} cm^2 s^{-1} during discharge/charge processes. This is one to two orders of magnitude higher than that of bare MnS or MoS_2, calculated from GITT results.[111] Besides, through *ex-situ* EIS tests, MnS-MoS_2 heterostructures demonstrate the smallest resistance, corresponding to the best electrical conductivity. The built-in electric field contributes to both increased electron transfer and elevated ion migration of the heterostructure.

Theoretical calculations were also carried out to verify the existence of the built-in electric field. Yang *et al.* applied first-principles density functional theory (DFT)

calculations to identify the existence of an internal electric field in a 2D-2D $(SnCo)S_2$ heterostructure.[109] The density of states (DOS) comparison of SnS_2 and $(SnCo)S_2$ elucidates that the higher spin polarization of Co produces a raised valance band edge in $(SnCo)S_2$ and therefore results in a narrowed band gap (0.2 eV) for $(SnCo)S_2$ compared with 1.7 eV for pristine SnS_2, suggesting the formation of *p-n* heterojunctions (**Figure 1.7d-i**). Furthermore, the evident charge separation phenomenon based on the charge-difference distribution for $(SnCo)S_2$ clearly proved the existence of a built-in electric field in this heterostructure. For boosting Na^+ ion diffusion in SnS_2/Sb_2S_3 heterostructures, DFT calculations also elucidated this phenomenon.[112] Sb_2S_3 has an intrinsically higher Fermi level than SnS_2, which results in a downward Fermi level shift of SnS_2 and an opposite behavior for Sb_2S_3 once they contact. Consequently, the built-in electric field is generated with positive and negative charges accumulating on the Sb_2S_3 and SnS_2 sides of the heterointerface, respectively. A Na^+ reservoir is built on the SnS_2 interface, attracting the gathered negative charge. Therefore, abundant Na^+ ions can diffuse across the SnS_2/Sb_2S_3 heterointerface (especial on the SnS_2 sides) with a calculated Na^+ diffusion barrier of 0.20 eV, which is lower than SnS_2 (0.69 eV) and Sb_2S_3 (0.29 eV).

Overall, the critical factors for forming a built-in electric field are the difference in intrinsic energy levels and the good contact of the two components. The low-Fermi energy-level material serves as an electron donor and the high-Fermi energy-level one acts as an electron acceptor as well as an alkali-ion collector. According to these principles, the built-in electric field hypothesis has been broadly accepted in heterostructures even beyond 2D material-based species.[113] However, the creation of built-in electric fields can only be achieved in heterostructures consisting of semiconductors with distinct band gaps, like TMDs, and TMOs, *etc.* It is dramatically more challenging to explain the function of graphene-based heterostructures since 2D

graphene performs strong metallic (not semiconductor) properties with a bandgap of 0 eV.

1.4.2 Providing fast ion diffusion channels

2D materials building via the vdW interaction between monolayers are desirable electrode candidates, benefiting from relatively low diffusion barriers between and within planar monolayers for alkali-ion batteries. The advantage of "galleries" weakly attracted to each other by the vdW interaction between large planar areas of material makes nearly all 2D materials available for Li^+ intercalation. However, it becomes strenuous when applied in other alkali-ion batteries due to the difficulty of intercalating large ions (Na or K). Some efforts have been concentrated on fine-tuning gallery spacing distances by intercalating different ions or various dimensional materials (from 0D to 2D), in order to accommodate target intercalants, such as Na^+ and K^+ ions, or even multivalent ions like Mg^{2+}, Zn^{2+}, and Al^{3+}.[114-116] Thereby, the original 2D ion diffusion channels ("galleries") are modified by formed heterostructures with finely-tunable interspaces. The relationships between Li^+ diffusion kinetics and spacing distances of 2D layers (graphene and borophene) as well as heterostructures (borophene/graphene) have been revealed by DFT calculations (**Figure 1.8a, b**).[117] For both pure 2D layers and heterostructures, the charge transference of Li increases with increasing interlayer spacing in a small range (<5Å) and maintains constant after excessive expansion. In reverse, the adsorption energy has an opposite change during the expansion process with a quick decline below 4Å and a subsequently slight bounce until stabilizing. Since the weak adhesion between alkali metals and heterostructures can diminish the diffusion barriers and remove the effects of high occupancy,[103] the diffusion barrier of Li^+ in heterostructures also shows a similar tendency, with a dramatic decrease in the initial expansion of interspacing. This result verifies the suitability of enlarging interspacing *via* constructing heterostructures to

optimize the ionic diffusion channels in 2D materials. Principally, enlarged interspacing can weaken the vdW interactions between 2D nanosheets and consequently shorten the ionic diffusion pathway, broaden activated surface of 2D species, and finally facilitate ion transport. The increase of interspacing is strongly relevant to the type and arrangement of intercalated ions or moleculars. The ultimate situation is the exfoliation of 2D materials.

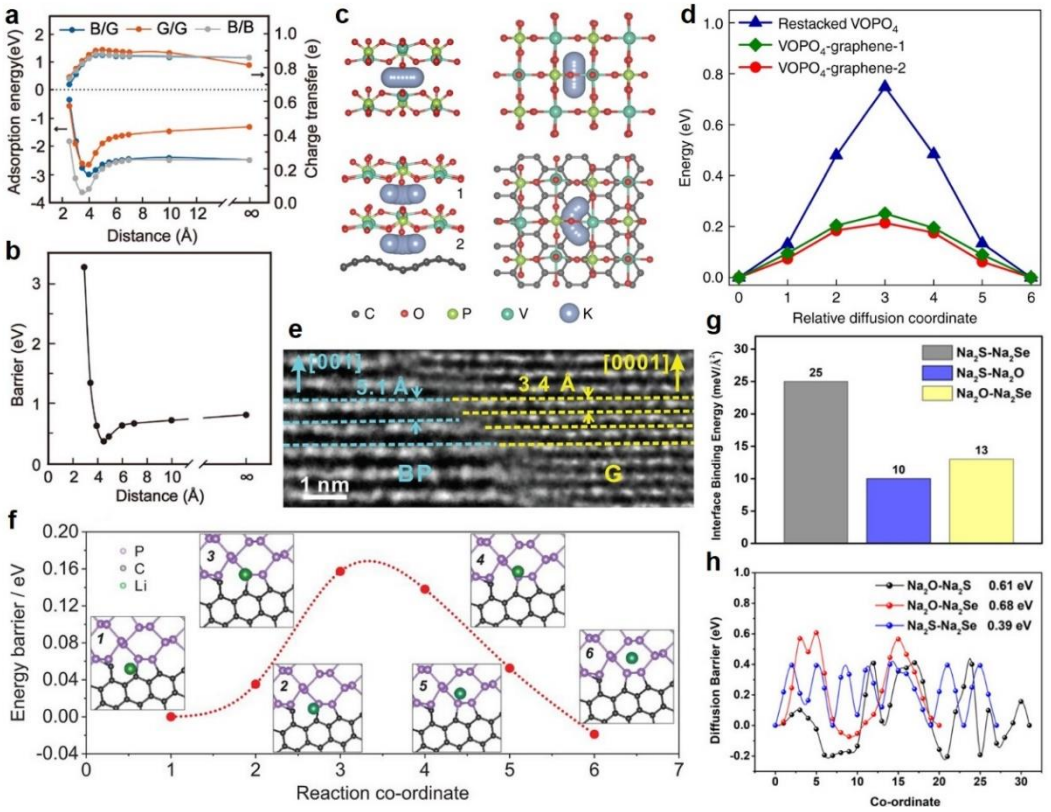

Figure 1.8 Ion diffusion behaviors in the 2D material-based heterostructures. a) The adsorption energies of Li in the interlayer of B/G, 2-layer graphene, and 2-layer borophene, as well as the charge transfer of Li with different interlayer distances. b) Diffusion barrier changes of one Li atom on the B/G heterostructure with the interlayer distance.[117] c) Typical models of K atom diffusion path in the interlayer of restacked $VOPO_4$ and $VOPO_4$-graphene. d) K diffusion energy profiles of restacked $VOPO_4$ and $VOPO_4$-graphene.[118] e) High-resolution TEM image showing the merge of basal planes of BP and graphite. Every two BP layers match with three graphene layers. f) The

minimum energy pathways for Li^+ to diffuse through the BP-G boundary.[119] g) Interface binding energy of three interface structures. h) Diffusion energy barrier of a Na atom in three interface structures.[120]

In fact, some heterostructures without enlarged 2D interspacing also present enhanced rate performance owing to the boosted ionic diffusion kinetics.[121-123] This should be ascribed to the increase of binding energy between one side of interfaces (depending on the intercalated ions and the configurations) and ions, which subsequently facilitates ion accumulation and the reduction of diffusion barriers.[102,103,121] However, these calculations are based on ideal thermodynamic models without consideration of mechanical variations in heterostructures. Our recent experiments found the interfacial strain in $VOPO_4$/graphene heterostructures induced superior rate performance in potassium-ion batteries.[118] Based on DFT calculations (**Figure 1.8c, d**), K^+ diffusion kinetics are improved not only at $VOPO_4$/graphene heterointerface (pathway 2) but also along the $VOPO_4$ sides next to the interface (pathway 1). Both diffusion energies are lower than the restacked $VOPO_4$ nanosheets, indicating the important role of interface strain in reducing diffusion barriers. Moreover, defects are occasionally introduced during the synthesis process, which can dramatically lower ionic diffusion barriers. For example, the ideal VSe_2/$MoSe_2$ heterostructure exhibits a Li^+ diffusion barrier of 0.48 eV, while this value is only 0.07 eV in vacancy-containing $V_{0.92}Se_{1.84}$/$MoSe_2$.[124]

Retaining smooth diffusion pathways inherited from parent 2D structures or materials is the most critical principle for the construction of heterostructures by further modifications. Black phosphorus is a promising anode material for alkali-ion batteries due to its high capacities and low ion diffusion barrier (theoretically, along a zigzag direction), but it suffers from edge reconstruction, which makes the advantages of fast

ionic diffusion to disappear in practical applications.[125] This phenomenon has been commonly overlooked in numerous fabrications or modifications of BP-based heterostructures. Although higher specific capacity and better cycling life have been achieved, the discharging/charging abilities at high current rates are still not as fast as desired.[126] Recently, Ji and Duan found that the existence of covalent bonds at the heterointerfaces between graphite and BP maintained edges open for fast Li^+ entry.[119] During a ball-milling process, P−C valent bonds are formed at the edges of BP layers, proven by dislocations at interfaces in HRTEM images (see **Figure 1.8e**) where every three graphene layers match with two BP layers in the plane. Other studies also proved the existence of valent bonding between P and C in ball-milled BP/graphite heterostructures through XPS spectra.[127,128] The X-ray absorption spectroscopy (XAS) measurements in P *K*-edge spectra show higher photon energy of peak A in the heterostructure (2146.2 eV) compared with that in bare BP (2145.7 eV). This corresponds to the charge transfer from P atoms to C atoms, which also strongly verified the existence of valent bonds. DFT calculations (**Figure 1.8f**) show that the energy barrier for Li^+ migration into BP through the heterointerface (0.16 eV) is much lower than across a reconstructed BP edge (0.52 eV). Consequently, the overall Li^+ diffusion coefficient of BP/graphite heterostructure increases by one order of magnitude, and the utilization and reversibility of BP electrodes have been improved.

The application of 2D ionic conductors can offset low ionic kinetics of the other material in a heterostructure and thus improve the overall ion diffusion capability. This strategy is especially useful for the modification of low-dimensional TMD and TMO anodes, such as Sb_2Se_3/rGO[129] and Fe_2O_3/MXene[130]. A typical activation energy E_a has been employed to identify the energy barrier of Na^+ intercalation in Sb_2O_3/MXene ($Ti_3C_2T_x$) heterostructures based on the Arrhenius equation:[131]

i_0=RT/(nFR_{ct})=$Aexp(-E_a/RT)$,

where R and F are ideal gas and Faraday constants, respectively; T is the absolute temperature, A is a temperature-independent coefficient, and n is the number of transferred electrons. Various charge transfer resistances (R_{ct}) can be determined *via* EIS measurements at different temperatures. Then the exchange current (i_0) can be calculated from the equation by plotting the Arrhenius profile (log i_0−1/T), from which the sodium activation energies of individual Sb_2O_3 and Sb_2O_3/($Ti_3C_2T_x$) heterostructure anodes are determined as 47.1 and 33.5 kJ mol^{-1}, respectively. The lower E_a for Sb_2O_3/$Ti_3C_2T_x$ heterostructure indicates the higher sodiation reactivity and faster Na^+ diffusion kinetics. Here the MXene layer plays an important role in the enhancement of kinetics due to its intrinsically high Na^+ diffusion coefficient (> 3.0×10^{-12} cm^2 S^{-1}).[132] Furthermore, the improvement in ionic intercalation kinetics is even noticeable in multivalent-ion batteries. DFT calculation shows the Mg^{2+} diffusion barrier in MoS_2/graphene heterostructures is 0.4 eV lower than that in MoS_2 bilayers (1.1 eV). According to the Arrhenius equation, the calculated diffusion coefficient ratio between MoS_2/graphene heterostructure and bare MoS_2 reaches 5.74×10^{11}, strongly indicating the fast Mg^{2+} diffusion kinetics in heterostructures.[133]

In general, most studies focused on constructing heterostructures with ion diffusion channels before considering applications in batteries. However, the as-built architectures could become fragile after ion intercalation and/or conversion reactions. The phase transformation and the subsequent volume change may induce the segregation of the two coupled components and the collapse of existing ion diffusion pathways. A forward-thinking design has been reported in terms of enabling discharge products to form heterointerfaces in sodium-ion batteries, such as Na_2O, Na_2S, and Na_2Se.[120] In this

system, there are three types of configurations among discharging products, *i.e.*, Na_2S-Na_2Se, Na_2O-Na_2Se, and Na_2S-Na_2O. DFT calculations indicate that Na_2S-Na_2Se has the most stable interface with an interface binding energy of 25 meV $Å^2$, which is twice the value of the others (**Figure 1.8g**). More importantly, this heterointerface has the lowest Na^+ diffusion barrier of only 0.39 eV (vs. 0.61 eV and 0.68 eV for Na_2O-Na_2Se and Na_2S-Na_2O), owing to the relatively weak electronegativity of S (2.589) and Se (2.424) than O (3.61) (**Figure 1.8h**). This means the electrostatic effect at a Na_2S-Na_2Se interface is less significant. Under the guidance of this model, the constructed 2D-2D SnS-$SnSe_2$ heterostructures exhibit dramatically improved Na^+ diffusion kinetics even during cycling. This work shows great significance for the fabrication of heterostructures through comprehensive structural variations before, during, and after electrochemical reactions.

1.4.3 Restricting volume expansion

In alkali-ion storage systems, most electrode materials undergo volume expansions during the alkali-ion insertion process. This phenomenon is especially conspicuous in anode materials. The expansion ratios are highly related to the intercalation ions and the types of anode materials. For example, graphite, a typical insertion-type anode material, suffers from 13% volume expansion after full lithiation but over 60% after potassiation. The volume changes in alloy materials are much more significant, usually more than 100% (>300% for Si, P, Sn, 135% for Sb, *etc.,* in lithium-ion batteries). The insertion of alkali ions into conversion and alloying anodes is often accompanied by phase transformations, including the formation of transition metal and alkali metal dichalcogenides (MX), or oxides for TMDs or TMOs, and alkali-ion rich alloys for alloying-type materials.[5] The crystal structure changes bring a volumetric variation of electrode materials, which leads to the aggregation of inactive and poorly-conducting discharging products, weakening electrical continuity between active materials and current collectors during long-term

insertion-extraction processes. Through synchrotron X-ray tomography techniques, Ebner *et al.* observed the *in-situ* phase transformation of Li and SnO to Li_2O and Li_xSn during the lithiation process, associated with a substantial volume expansion (258%).[134] This causes severe mechanical rupture of active material particles and irreversible structural distortion of electrodes.

Table 1.3 Young's modulus (E), Poisson's ratio (ν), elastic moduli (C_{11} and C_{12}), uniaxial strains along zigzag (δ_x), and armchair (δ_y) directions of various 2D materials and heterostructures.[104]

system	E (N/m)	ν	C_{11} (N/m)	C_{12} (N/m)	δ_x (%)	δ_y (%)
Graphene	341.2	0.169	351.4	59.6	15	15
MoS_2	139.2	0.239	147.7	35.3	20	26
Ti_2CF_2	178.9	0.308	196.4	60.5	30	16
Ti_2CO_2	213.2	0.299	234.1	70.0		
MoS_2/Ti_2CF_2	309.6	0.265	333.1	88.3	28	20
MoS_2/Ti_2CO_2	370.6	0.274	400.6	109.7	24	22

Consequently, electrodes suffer from a fast capacity fade when cycling. An effective approach to solve this problem is constructing heterostructures with 2D materials by utilizing their excellent mechanical properties. In a 2D hexagonal lattice, there are two high-symmetry directions, *i.e.,* zigzag (x) and armchair (y) directions associated with distinct strengths of chemical bonds. **Table 1.3** shows the calculated mechanical properties, including Young's modulus, Poisson's ratio, elastic moduli, and uniaxial strains along x and y directions of various 2D monolayers and heterostructures. After coupling with MXene monolayers (Ti_2CF_2 or Ti_2CO_2), Young's modulus of MoS_2 is increased, indicating the enhancement of mechanical flexibility. While the uniaxial

strains of heterostructures are the average values of the two constituents.[104] Nevertheless, both MoS_2/Ti_2CF_2 and MoS_2/Ti_2CO_2 have better uniaxial strains than graphene, suggesting the good mechanical strength of these heterostructures. The blue phosphorene/MS_2 (M=Nb and Ta)[135] and black phosphorene/TiC_2[136] heterostructures also achieved increased mechanical strength, according to similar calculations. Recently, Li *et al.* studied the in-plane stiffness (Young's modulus) change (**Figure 1.9a**) of a blue phosphorene/graphene heterostructure during Li^+ intercalations. Although the stiffness decreases with the increase of Li^+ contents, over 83% retention of stiffness has been achieved, corresponding to the formation of $Li_{22}P_{18}C_{32}$, with a small volume expansion of 10.89% (including 1.24% surface areas extension and 9.53% interspace increase).[100] This demonstrated the volume change restriction effect of heterostructures.

To confirm theoretical calculations, *in-situ* measurement techniques are needed to quantify microscopic volume changes precisely. Cui *et al.* detected the anisotropic volume variation of black phosphorus *via* an *in-situ* TEM technique.[137] They found that the *x* axis spacing of phosphorene layers was nearly unchanged, while *y* and *z* axes underwent huge expansions (up to 92% and 160%, respectively) during a sodiation process. Without coupling with other 2D materials like graphene or MXene, capacities faded within several cycles.[81,138] Furthermore, it is also desired to reveal the buffering effect of constructing heterostructure on phosphorene by visualization methods. Mai's group fabricated a 1D-2D heterostructure (V_2O_3@C-NTs@rGO) consisting of V_2O_3 nanoparticles sealed in 1D amorphous carbon nanotubes (V_2O_3@C-NTs) and 2D rGO nanosheets and proved the confinement of volume change through *in-situ* TEM imaging.[139] The nanoscale cathode V_2O_3@C-NTs@rGO heterostructures (or V_2O_3@C-NTs for comparison) were fixed on tungsten meshes and assembled into half cells with Na metal anodes separated by Na_2O electrolytes (**Figure 1.9b, d**). From the resultant *in-*

situ TEM images, 1D V_2O_3@C-NTs were observed to undergo only a slight expansion during the sodiation process (**Figure 1.9c, e**). Instead, rGO nanosheets are stretched to absorb the strain from the phase transformation of V_2O_3. In contrast, the intercalation of Na ions causes visible swelling and even cracks on individual V_2O_3@C-NTs without rGO.

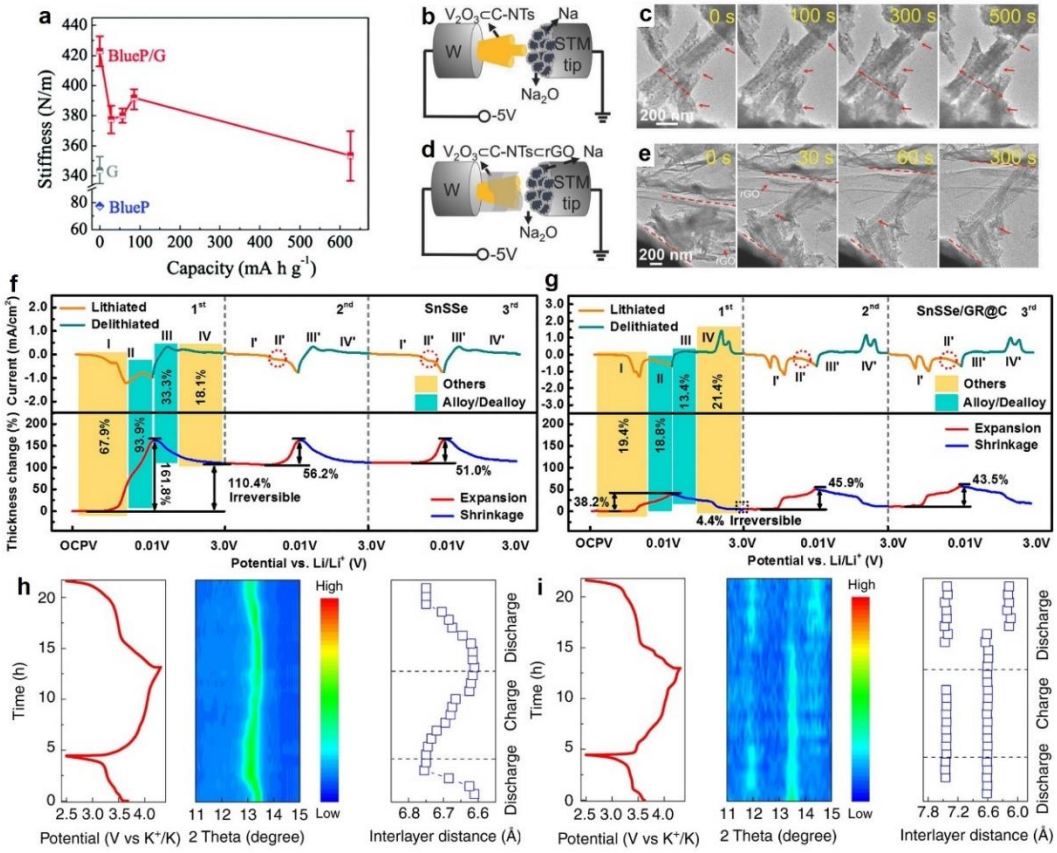

Figure 1.9 Volume variations of the 2D material-based heterostructures within the intercalation/extraction of alkali ions. a) The stiffness of blue phosphorene/graphene (BlueP/G) with different Li contents. The grey and blue values represent the stiffness of graphene and BlueP, respectively.[100] Schematic and structural evolution of b, c) the V_2O_3⊂C-NTs and d, e) V_2O_3⊂C-NTs⊂rGO electrodes observed by in situ TEM experiments, respectively.[139] Volume change test result of f) SnSSe and g) SnSSe/GR@C electrodes.[140] Typical charge/discharge profiles and *in-situ* XRD patterns

of (h) $VOPO_4$-graphene and (i) $VOPO_4$ nanoflakes as cathodes for PIBs with the calculated interlayer distances during charge/discharge processes in PIBs.[118]

Although *in-situ* TEM characterization can monitor the structural variation, the results do not reflect the actual volume change of electrodes. Measuring the thickness of post-cycled electrodes at macroscopical scale is another way to evaluate the volume expansion of the electrode materials. For example, we fabricated GO-wrapped N-doped carbon-coated 1D Sb_2Se_3 (Sb_2Se_3@NC@GO) composite for potassium-ion batteries.[141] By comparing the thickness of electrodes before and after cycling interspersed with *ex-situ* SEM characterizations, we evaluated the swelling of individual Sb_2Se_3@NC and Sb_2Se_3@NC@rGO heterostructure electrodes. After 8 cycles, the increase of Sb_2Se_3@NC electrode thickness reaches over 100%; while the thickness change of the 1D-2D Sb_2Se_3@NC@rGO heterostructure is only ~10%, which strongly proved the buffering effect of constructing heterostructures. Furthermore, electrochemical dilatometry techniques can be applied *in-situ* to obtain data on electrode dilatation.[142] Kim *et al.* directly grew nanosized Fe_3O_4 particles on rGO nanosheets as a 0D-2D heterostructure (Fe_3O_4/rGO) for lithium storage.[143] The dilatometric experiments indicate that the heterostructure has a much lower initial expansion (26% *vs.* 90% for commercial Fe_3O_4) and stable breathing-like variations beyond the second cycle, which is mainly attributed to the low deformation (<5%) of rGO substrates. Recently, Chen *et al.* reported in detail the step-wisely volumetric changes (related to multistep reactions) of individual SnSSe anodes and SnSSe/GR (graphene) heterostructures with the support of a carbon coating.[140] Combining CV curves with *in-situ* electrochemical dilatometry, as shown in **Figure 1.9f and g**, both conversion and alloying reactions cause severe volume expansion to SnSSe anodes. Overall, individual SnSSe was observed to suffer from a giant expansion rate of 161.8% during the lithiation process and an irreversible

electrode distortion of 110.4% after charging, reflecting the serious damage to the integrity of electrodes. In contrast, the integration of the SnSSe/GR heterostructure *via* carbon coating dramatically reduces the degree of volume variation.

Unlike visual observation, the analysis of crystal parameters is usually a more accurate approach for quantifying volume variations. This method is often employed for investigating cathode materials or insertion-type anode materials. Recently, our group synthesized a novel zero-strain cathode by introducing interfacial strain in a 2D-2D $VOPO_4$/graphene heterostructure, which was self-assembled *via* electrostatic adsorption of negatively-charged $VOPO_4$ and positively-charged graphene nanosheets.[118] The mismatch of lattice spacing of two components triggers interfacial strains at heterointerfaces when graphene is interfaced to $VOPO_4$. The blue shifts of O−P−O and V=O stretching modes of $VOPO_4$ in Raman spectra are solid evidence proving the compressive interfacial strain on $VOPO_4$ surfaces with lattice strain values of ~4.0% from experimental observations and 3.2% from DFT calculations. During the K^+-ion insertion process, *in-situ* XRD results indicate only a tiny swelling (2.0%) associated with weak shifts of (001) peak in $VOPO_4$/graphene heterostructures (**Figure 1.9h, i**). In contrast, restacked plain $VOPO_4$ nanoflakes suffer from a tremendous expansion of 136% with a significant increase of interlayer spacing to ~0.75 nm. This excellent zero-strain performance of $VOPO_4$/graphene heterostructures is ascribed to the offset of volume expansion by interface strain at the heterointerfaces.

1.4.4 Increasing electrochemical reactivity

In rechargeable batteries, electrochemical reactions often occur on the interfaces between solid-state electrodes and liquid-state electrolytes. Due to the large surface areas and good wettability of electrolytes, 2D pillared materials in heterostructures (Figure

1.10), especially graphene, MXene, *etc.*, play an important role in improving electrochemical reactivity in alkali-ion batteries.[144,145]

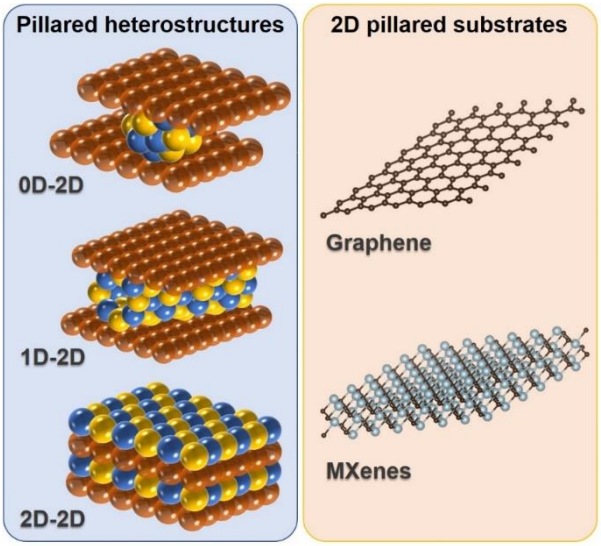

Figure 1.10 Schematic illustration of 2D pillared materials in heterostructures.

The heterostructure-induced enhancement of electrochemical reactivity in other types of rechargeable batteries, such as alkali metal-sulfur batteries, shows different mechanisms.[146] In Li-S batteries, 75% theoretical capacity comes from the slow liquid-solid phase transformation between soluble Li_2S_4 and insoluble solid Li_2S in organic electrolytes. The sluggish kinetics of this reaction usually results in a "shuttle effect" of soluble lithium polysulfides (Li_2S_x) from cathodes to anodes and the formation of "dead" Li_2S particles, which leads to arbitrary precipitation and aggregation of insoluble solid Li_2S on cathode surfaces.[147,148] 2D materials show great potential for solving these problems.[149] For example, Cui's group calculated that 2D layered transition metal oxides, sulfides, and chlorides can adhere Li_2S_x *via* both physical adsorption (van de Waals interaction) and chemical bonding before and after lithiation, respectively.[150] Different materials have distinct adsorption features controlled by the binding energy between Li_2S_x species and anchoring 2D materials. The binding forces follow the sequence of

oxides>sulfides>chlorides from strong to weak. This Li_2S_x-binding strategy can effectively prevent the dissolution of Li_2S_x in electrolytes. Moreover, they proved that 2D transition metal sulfides, such as VS_2, TiS_2, and CoS_2, have catalytic capability to reduce the activation energy barrier for the transformation from Li_2S to sulfur, and therefore boosting the decomposition kinetics of solid Li_2S and fostering the reversible conversion between soluble and insoluble Li_2S_x species.[151]

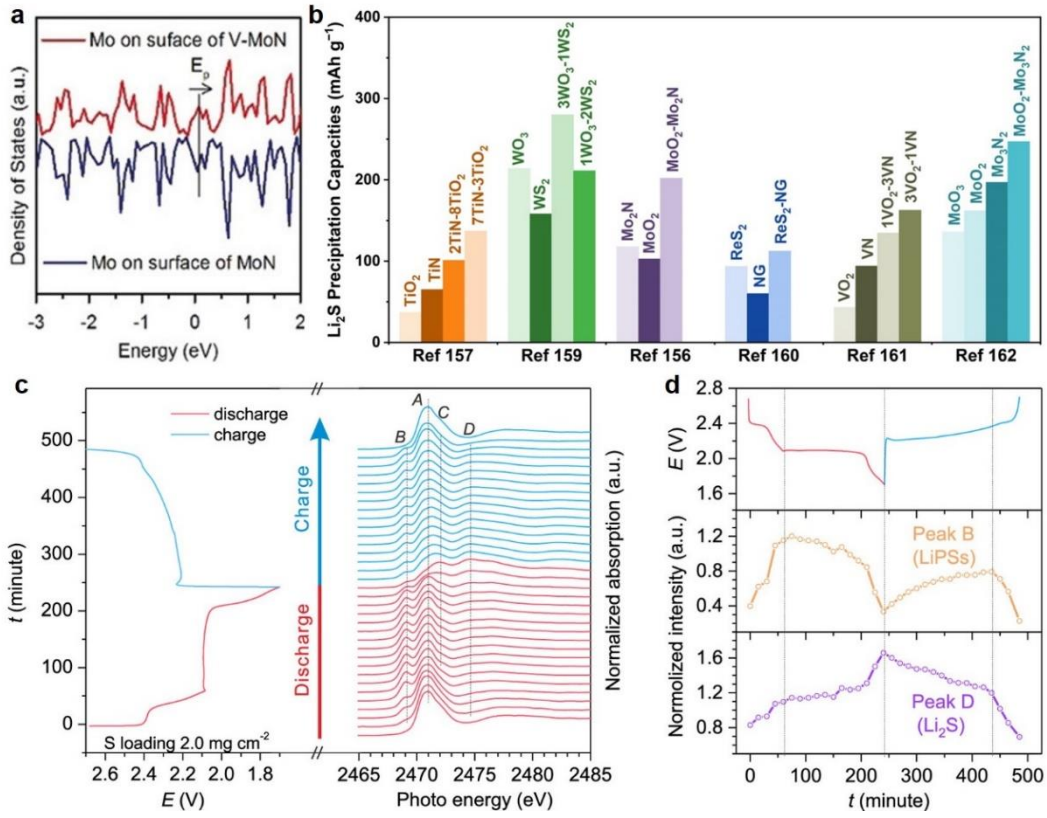

Figure 1.11 Increased electrochemical reactivity of 2D material-based heterostructures in Li-S batteries. a) DOS of Mo on surfaces of V-MoN and MoN, the black line is a visual guide.[152] b) Li_2S precipitation capacities of various heterostructures with associated configurations reported in publications (NG represents N-doped graphene). c) Evolution of S K-edge XANS during electrochemical cycling. d) Evolution of the intensities of peak B (2469.0 eV, representing the concentration of LiPSs) and peak D (2474.7 eV, representing Li_2S concentration) during electrochemical cycling.[153]

The adsorption and catalysis effects of 2D material-based heterostructures can be further enhanced by modifying electronic structures. Qiao's group theoretically and experimentally investigated the adsorption of Li_2S_x species in an in-plane 2D MoN-VN heterostructure.[152] Compared with bare MoN, Mo *L*-edge near-edge X-ray absorption fine structure (NEXAFS) results show that Mo in MoN-VN heterostructure is in a higher oxidation state due to the reduced electron density of Mo associated with the strong coupling between MoN and VN. When immersed in Li_2S_x-rich solutions, both heterostructure and bare MoN show an obvious peak shift of Mo^{3+} $3d_{5/2}$ signals corresponding to the charge transfer from S_x^{2-} to Mo^{3+} in XPS. The MoN-VN heterostructure exhibited a much better adsorption capability. From DFT calculations, the good adsorption of Li_2S_x species for MoN-VN heterostructures is ascribed to the tailoring of surface Mo electronic states by the introduction of V atoms. MoN-VN heterostructures possess a higher E_p (nearest peak to Fermi Level) and subsequently lower occupancy of the anti-bonding states (σ^*) in the adsorption states, compared with the pure MoN counterpart (**Figure 1.11a**). This leads to a stronger interaction between adsorbate and catalyst surface. Therefore, the application of MoN-VN heterostructure cathodes loaded with 3.0 mg cm^{-2} sulfur shows a low capacity fading of 0.068% per cycle during 500 cycles.

Interestingly, the adsorption of polysulfides is also detected in some anode materials in alkali-ion batteries, especially in TMDs-based heterostructures. In an Sb_2S_3-FeS_2 heterostructure, the calculated adsorption energy of Na_2S on the heterointerface is only −1.34 eV (much lower than on the surface of bare Sb_2S_3 with −0.50 eV), suggesting the favorable adsorption effect of heterostructures for the discharge product Na_2S.[154] Therefore, Sb_2S_3@FeS_2 heterostructures demonstrate enhanced reaction reversibility and reduced electrode pulverization.

Further research found that the adsorption and catalysis functions co-exist in heterostructures, where transition metal oxides or carbonaceous materials (like graphene, MXene) tend to adsorb Li_2S_x species; while transition metal dichalcogenides, phosphides, and nitrides perform the role of catalysis.[155,156] In oxides-nitrides heterostructures, first-principle calculations prove that oxides have a better affinity for soluble Li_2S_x, corresponding to a higher binding energy than nitrides, for example, −4.65 eV and −2.97 eV as the adherent energy of Li_2S_4 on MoO_2 and Mo_2N surfaces, respectively.[157] Once the dissolved Li_2S_x species are trapped by oxides, they may be transferred to the interface close to nitrides for further catalytic reactions due to the low diffusion barrier on oxides surfaces (the Li_2S_4 diffusion barrier on TiO_2(110) is only 1.04 eV).[158] Besides these effects, a strong-charge-polarization effect in the oxides-nitrides heterostructure was found to facilitate electron transfer from hosts to Li_2S_x, and thus increase the conversion reactivity.[159]

Potentiostatic discharge techniques are usually employed to quantify the promotion of conversion reaction activity in heterostructures. This method is carried out in half cells consisting of a catalyst (embedded on carbon cloth) cathode, metal anode, and polysulfide electrolyte, which are galvanostatically discharged to the potential plateau levels of the conversion reaction from polysulfide, such as Li_2S_8/Li_2S_6 to Li_2S_2/Li_2S and then potentiostatically discharged at a similar voltage. The obtained precipitation current and conversion capacity illustrates the catalytic activity of cathode materials.[160] Numerous studies have applied this approach to verify the enhanced conversion efficiency in heterostructures.[157,158,160-163] Here we listed some representatives in **Figure 1.11b**.

In recent years, a special 0D-2D heterostructure, namely a single-atom embedded 2D heterostructure, has attracted extensive interest in energy conversion fields due to their

high utilization of catalysts.[88] This sort of architecture can also improve the efficiency of conversion catalysis in Li-S batteries as well. Du *et al.* embedded ~0.77 *at.* % Co single atoms on N-doped graphene nanosheets as a high-sulfur content (90 *wt.* %) host for Li-S batteries.[153] During the conversion reactions between soluble Li_2S_x and the insoluble Li_2S_2/Li_2S, the host with Co−N−C centers exhibited the largest current density in CV profiles in symmetric cells and the lowest overpotentials in discharge/charge profiles. From the *operando* XANES measurement (**Figure 1.11c, d**), the formation of Li_2S species has been detected earlier than in other cathodes, strongly proving the increase of electrochemical reactivity. This improvement is ascribed to the increased electrical conductivity around Co−N−C centers and the subsequent catalytic effect for reducing energy barriers of redox reactions of Li_2S_x species, especially the reduction of Li_2S_2 to Li_2S (1.43 eV vs. 2.29 eV for bare N-dope graphene). Although the heterostructure has a lower specific surface area than their 2D component, the heterostructure cathode still delivered a high areal capacity of 5.1 mAh cm^{-2} at 0.2 C over 100 cycles with a capacity decay rate of 0.029% per cycle even at a high S mass loading of 6.0 mg cm^{-2}.

Additionally, the 0D-2D heterostructures consisting of conductive 2D matrixes and catalytic noble nanoparticles are widely employed for other types of recharge batteries based on the conversion reactions, such as Li-O_2, Na-O_2, and Li-CO_2 batteries.[164] The 2D materials with high surface area are ideal hosts for accommodating the solid discharge products (such as Li_2O_2 and Li_2CO_3). Meanwhile, the loaded 0D catalysts can accelerate the conversion reaction kinetics, or even mediate the structure of discharge products and enable them to be decomposed more easily during charging.[165] The enhanced electrochemical reactivity was also demonstrated in 2D-2D heterostructures through interface engineering. For example, Liu *et al.* revealed that the oxygen evolution reaction (OER) and oxygen reduction reaction (ORR) activity in Na-O_2 batteries were boosted

simultaneously owing to the interpenetration of P−O at the interfaces of CoO/CoP heterostructured nanosheets.[166] Similarly, an improved OER and ORR activities were achieved by the $CoSe_2$@$NiSe_2$ heterostructures because of the disordered atomic arrangement and lattice distortion at the heterointerface.[167] The significantly increased electrochemical reactivities are effective for lowering the round-trip efficiency and prolonging the cycle life of these metal-oxygen batteries, which makes 2D material-based heterostructures more attractive in conversion-type batteries.

Chapter 2 Experiments and Methodology

The overall investigation route of each experimental chapter is presented in **Figure 2.1**. Based on the previous literature review, we can confirm the research aims for the investigation target materials in the certain applied battery systems and find out the research gaps and the possible solutions. Next, material design will be conducted to achieve the functional improvement and then corresponding 2D material-based heterostructures are synthesized following the designed strategies. Some basic characterizations, like X-ray diffraction (XRD), scanning electron microscopy (SEM), transmission electron microscopy (TEM), X-ray photoelectron spectroscopy (XPS), Raman spectra, thermogravimetric analysis (TGA), *etc.*, need to be carried out to confirm the fabrication of the desired heterostructures and also study some fundamental physicochemical properties. The electrochemical performance of heterostructures, such as cyclic voltammetry (CV), galvanostatic charge/discharge (GCD), rate performance, electrochemical impedance spectra (EIS), *etc.*, will be compared with original building blocks. To further study the reason of the electrochemical improvement, we may need to employ some advanced techniques, including *in-situ* XRD, *ex-situ* SEM, *ex-situ* TEM, theoretical calculations. Finally, we must analyze the obtained data to get the crucial information before finishing the manuscript, like phases, bonding states, specific morphology, ion storage mechanism, kinetics, *etc.*

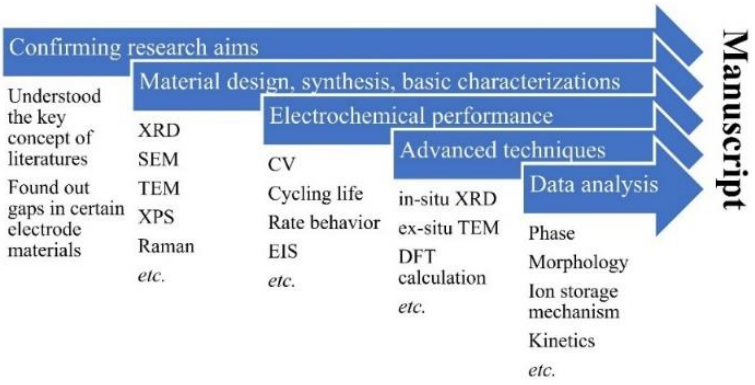

Figure 2.1 Overview schematic illustration of experiments and methodology.

2.1 Chemicals

A list of the names of materials and chemicals used in the thesis with corresponding formula, purity, and supplier, is shown below in **Table 2.1**. All chemicals are directly used without further purification in all experiments.

Table 2.1 Chemical details in this thesis.

Chemicals	**Formula**	**Purity**	**Supplier**
MAX ceramic powder	Ti_3AlC_2	99%	11 Tech. Co. Ltd.
Lithium fluoride	LiF	99%	Sigma Aldrich
Hydrochloric acid	HCl	37%	Chem Supply
Graphite flake	C	99%	Sigma Aldrich
Sodium nitrate	$NaNO_3$	99%	Chem Supply
Sulfuric acid	H_2SO_4	98%	Chem Supply
Potassium permanganate	$KMnO_4$	99%	Sigma Aldrich
Hydrogen peroxide	H_2O_2	50%	Sigma Aldrich
Citric acid	$C_6H_8O_7$	99%	Sigma Aldrich
Antimony chloride	$SbCl_3$	99.99%	Sigma Aldrich

PEG-400	$H(OCH_2CH_2)_nOH$	99%	Sigma Aldrich
Selenium powder	Se	99.5%	Sigma Aldrich
Sodium borohydride	$NaBH_4$	98%	Sigma Aldrich
Dopamine hydrochloride	$C_8H_{12}NO_2 \cdot HCl$	99%	Sigma Aldrich
Tris(hydroxymethyl)aminomethane	$C_4H_{11}NO_3$	99.8%	Sigma Aldrich
Ethanol	CH_3CH_2OH	95%	Chem Supply
Tetramethylammonium hydroxide	$(CH_3)_4N(OH)$	25%	Sigma Aldrich
Manganese chloride hexahydrate	$MnCl_2 \cdot 6H_2O$	98%	Sigma Aldrich
Poly(diallyldimethylammonium chloride)	$(C_8H_{16}NCl)_n$	20%	Sigma Aldrich
Hydrazine hydrate	$N_2H_4H_2O$	50~60%	Sigma Aldrich
Carbon black	C	100%	Sigma Aldrich
Carboxymethyl cellulose sodium salt	$C_8H_{15}NaO_8$	–	Sigma Aldrich
Polyvinylidene fluoride	$(C_2H_2F_2)_n$	–	Sigma Aldrich
N-methyl-2-pyrrolidone	C_5H_9NO	99.5%	Sigma Aldrich
Potassium trifluoromethanesulfonimide	$KN(CF_3SO_2)_2$	97%	Sigma Aldrich
Ethylene carbonate	$C_3H_4O_3$	99%	Sigma Aldrich
Propylene carbonate	$C_4H_6O_3$	99.7%	Sigma Aldrich
Zinc sulfate heptahydrate	$ZnSO_4 \cdot 7H_2O$	99%	Sigma Aldrich
Manganese sulfate monohydrate	$MnSO_4H_2O$	99%	Sigma Aldrich
Potassium	K	99.5%	Sigma Aldrich

Zinc	Zn	99.9%	Sigma Aldrich

2.2 Materials Synthesis

2.2.1 Hydrothermal/solvent-thermal method

The hydrothermal method refers to a method of preparing materials by dissolving and recrystallizing powder in a sealed pressure vessel, using water as a solvent. Compared with other synthesis approaches, the powder prepared by the hydrothermal method has the advantages of complete grain development, small particle size, uniform distribution, lighter particle agglomeration. Besides cheaper raw materials can be used, and suitable stoichiometry and crystal form can be easily obtained. The solvothermal method is a development of the hydrothermal method, which differs from the hydrothermal method in that the solvent used is an organic solvent instead of water. In a solvothermal reaction, by dissolving one or more precursors in a non-aqueous solvent, under liquid or supercritical conditions, the reactants are dispersed in the solution and become more active, the reaction occurs, and the product is slowly formed. The process is relatively simple and easy to control and can effectively prevent the volatilization of toxic substances and prepare air-sensitive precursors in a closed system. In this thesis, hydrothermal/solvent-thermal methods are employed to synthesize 0D-2D heterostructures in one pot (Chapter 3) and 1D Sb_2Se_3 nanorods (Chapter 4).

2.2.2 Preparation of $Ti_3C_2T_x$ MXene nanosheets

MXenes are a class of 2D inorganic compounds in materials science. These materials consist of transition metal carbides, nitrides or carbonitrides several atomic layers thick. It was originally reported in 2011 by Prof. Yury Gogotsi from Drexel University that MXene materials possess the metallic conductivity of transition metal carbides due to the presence of hydroxyl groups or terminal oxygens on their surfaces. Unlike traditional

electrode materials, this material provides more channels as pathways for ions, which greatly improves ion diffusion. Initially, hydrofluoric acid (HF) was applied to etch Al layers in a typical ceramic MAX phase Ti_3AlC_2. During etching process, the generated H_2 gas enlarges interspacing of $Ti_3C_2T_x$ layers, facilitating the exfoliation and resulting few-layer or multi-layer 2D MXene nanosheets. Due to the high operating risk of pure HF, the mixture of LiF salt and hydrochloric acid (HCl) was employed as an alternative for the etching process, which will release HF in solution slowly and mildly, improving the operating safety. Meanwhile, the intercalation of Li ions can promote the enlargement of interspacing. A more safety method to etch MAX phase has been put forward recently via a molten salt technique using Lewis acids, like $CuCl_2$, $NiCl_2$, $ZnCl_2$, $CuBr_2$, *etc.* The Al or Si layer in MAX phase will react with Lewis acids to be exchanged by Cu, Ni, Zn, *etc.* atoms at high temperatures and the by-products AlX_3 or SiX_4 (X = halogen ions) evaporate facilitating the etching process. The poor stability of MXene, especially in oxygen and water environments, is related to the sufficient terminal groups and large exposed metastable metallic surfaces. Therefore, an inert environment is definitely required to storage or apply MXenes, such as in N_2 purged solutions, as freeze-dried powders and so on. Therefore, in this thesis, we use the mild etching method with the mixture of LiF salt and HCl to prepare $Ti_3C_2T_x$ MXene nanosheets in Chapter 3.

2.3 Characterization

2.3.1 X-ray diffraction (XRD)

XRD is a non-destructive and rapid technique employed for determining the basic crystal structure of materials. It is mainly based on qualitative phase analysis, but quantitative analysis can also be performed. By comparing the XRD pattern of the sample to be tested and the XRD pattern of the standard material, the phase composition of the

sample can be qualitatively analyzed; by analyzing and calculating the diffraction intensity data of the sample, the quantitative analysis of the phase composition of the sample can be completed. In this thesis, XRD technique is conducted by Bruker D8 Discover XRD machine, which is applied to identify the phase of every component in the prepared heterostructures.

2.3.2 Scanning electron microscopy (SEM)

SEM is an electron microscope that produces an image of the surface for samples by scanning the sample surface with a focused electron beam. When a narrow focused high-energy electron beam scanning the sample, various physical information is excited through the interaction between the beam and the material. The characterization the microscopic morphology of the material is achieved by collecting, amplifying, and re-imaging this information. The resolution of the novel scanning electron microscope can reach 1 nm and its magnification can reach 300,000 times with large depth of field, field of view, and good imaging stereo effect. In addition, the combination of scanning electron microscope and other analytical instruments such as energy-dispersive X-ray spectroscopy (EDXS) can be used to observe the microscopic morphology and simultaneously carry out the analysis of material micro-area composition. In this thesis, two SEM machines, in terms of Zeiss Supra 55VP and EVO, are employed to demonstrate 3D high-resolution images of the heterostructure surface getting morphology information.

2.3.3 Transmission electron microscopy (TEM)

In TEM, an accelerated and focused beam of electrons is projected onto a very thin sample. The electrons collide with atoms in the sample and change direction, resulting in solid angle scattering. The size of the scattering angle is related to the density and thickness of the sample, so different light and dark images can be formed, and the image

will be displayed on the imaging device (such as phosphor screen, film, and photosensitive coupling components) after magnification and focusing. Since *de* Broglie wavelength of electrons is very short, the resolution of transmission electron microscopy is much higher than that of optical microscopy, which can reach 0.1 to 0.2 nm, and the magnification is tens of thousands to millions of times. Therefore, the utilization of transmission electron microscopy can be varied from observing the fine structure of a sample, to even the structure of just a column of atoms, which is tens of thousands of times smaller than the smallest structures that can be detected by optical microscopy. At lower magnifications, the contrast in TEM imaging is mainly associated with the specific electron absorption to the different thickness and composition of materials. When the magnification is high, the complex fluctuation will cause the difference in the brightness of the image, so professional knowledge is needed to analyze the obtained image. By using different modes of TEM, a sample can be imaged by its chemical properties, crystallographic orientation, electronic structure, electronic phase shift caused by the sample, and generally by electron absorption. In thesis, TEM technique is used not only to obtain micro- and nano-field morphology of heterostructures, but also to identify the crystal structure and chemical components via specific modes, like high-angle annular dark-field scanning transmission electron microscopy (HADDF-STEM), selected-area electron diffraction (SAED) and elemental mapping using energy-dispersive X-ray spectroscopy (EDXS).

2.3.4 X-ray photoelectron spectroscopy (XPS)

XPS, also known as electron spectroscopy for chemical analysis (ESCA) is an extremely surface-sensitive quantitative elemental chemical analysis tool used to solve material problems in a variety of fields. XPS is based on the photoelectric effect. By detecting the kinetic energy of the electrons excited by X-rays on the surface of the

material, the intrinsic electron binding energy information inside the material can be retrospectively obtained. This information reflects the fingerprint information of various elements and their valence states in the material. Only electrons very close to the surface of the material can escape without losing too much energy, so the information of XPS comes from the scale of several nanometers on the surface of the material. It is the extreme surface sensitivity and chemical quantitative analysis capability of this technology that makes XPS an important surface analysis method. In this thesis, XPS is an important chemical analysis approach to determine the elemental component and valence states for nano-sized heterostructures, whose results can be further applied to analyze the interaction information between atoms.

2.3.5 Raman spectra

Raman spectroscopy is a non-destructive analytical technique based on the interaction of light and materials. Raman spectroscopy can provide detailed information of chemical structure, phase and morphology, crystallinity, and molecular interactions in samples. Raman is a light scattering technique. When high-intensity incident light from a laser light source is scattered by molecules, most of the scattered light has the same wavelength (color) as the incident laser light. This scattering is called Rayleigh scattering. However, there is also a very small part (about 1/109) of the scattered light whose wavelength (color) is different from the incident light, and the change of its wavelength is determined by the chemical structure of the test sample (the so-called scattering material). This part of the scattered light is called pull-in Mann scattering. A Raman spectrum is usually composed of a certain number of Raman peaks, and each Raman peak represents the wavelength position and intensity of the corresponding Raman scattered light. Each spectral peak corresponds to a specific molecular bond vibration, which includes both single chemical bonds, such as C−C, C=C, N−O, C−H, *etc.*, and vibrations of groups composed of several

chemical bonds, such as benzene ring Breathing vibrations, vibrations of long polymer chains, and lattice vibrations, *etc.* In this thesis, Raman spectra are the crucial technique to study the bonding states, including the type features and the variation modes of bonds in inorganic heterostructures.

2.3.5 Thermogravimetric analysis (TGA)

TGA refers to a thermal analysis technique that measures the relationship between the mass of the sample to be tested and the temperature change under programmed temperature conditions and can be used to study the thermal stability and composition of materials. From its principle, we know that TGA analyzes the relationship between temperature and sample quality, so in the process of temperature change, there is a mass change reaction, which can basically be expressed by TGA. In practice such reactions include: (1) physical changes such as evaporation, sublimation, absorption, adsorption and desorption, *etc.*; (2) chemical reactions, TGA can also provide information about chemical phenomena such as chemisorption, desolvation (especially dehydration), decomposition, and solid-gas phase reactions (such as oxidation or reduction), *etc.* Here, we employ TGA to quantify the mass proportion of every component in heterostructures.

2.4 Electrode Preparation, Battery Assembly and Electrochemical Tests

2.4.1 Preparation of electrodes

The active materials are manually mixed in a mortar with conductive additives and polymer binders in solvents to form a homogeneous slurry as the first step for the preparation of electrodes, where carbon black is usually applied as the conductive additive, the selection of polymer binders ranges from CMC to PVDF, depending on the usage of solvent from water to NMP, respectively. The mass ratios among active materials, conductive additives and polymer binders are 7: 2: 1 or 7: 1.5: 1.5 in this thesis. Next, the

obtained slurry will be uniformly painted on current collectors, normally using Cu foils for anodes in potassium-ion batteries and carbon papers for cathodes in aqueous zinc-ion batteries. After drying under vacuum with heating, the electrodes are cut into small discs with a diameter of 12 mm, corresponding to an electrode area of 1.13 cm^2.

2.4.2 Battery assembly

Battery assembly for potassium-ion batteries must be conducted in an Ar gas protected glovebox with O_2 and H_2O contents both less than 0.1 ppm to avoid the decomposition of organic electrolytes and counter electrodes K flakes. The assembly starts from working electrodes, covered by separators soaking with electrolytes, and then fresh K flakes are added. All electrodes are assembled in CR2032 coin cells with leaf spring and stainless-steel gasket to increase the contact among electrodes and electrolytes. Finally, the coin cells are sealed under the certain pressure in a machine. As for aqueous zinc-ion batteries, the battery assembly procedures are the same as potassium-ion batteries, but they are just proceeded in air conditions without requirement for inert atmosphere.

2.4.3 Cyclic voltammetry (CV)

CV is a commonly used electrochemical research method. This method controls the electrode potential to scan one or more times with a triangular waveform at different rates over time. The potential range is to enable different reduction and oxidation reactions to occur alternately on the electrode, and the current-potential curve is recorded. According to the shape of the curve, the degree of reversibility of the electrode reaction, the possibility of intermediates, phase boundary adsorption or new phase formation, and the nature of the coupling chemical reaction can be judged. It is often used to measure electrode reaction parameters, determine its control steps and reaction mechanism, and observe which reactions can occur in the entire potential scanning range and what their

properties are. For a new electrochemical system, the preferred research method is often cyclic voltammetry.

2.4.4 Galvanostatic charge/discharge (GCD)

GCD method, also known as chronopotentiometry, is one of the very important methods in studying the electrochemical properties of materials. Charge and discharge the tested electrode under constant current conditions, record its potential variation with time, and study the variation of potential as a function of time. Its basic working principle is that charge and discharge the tested electrode under constant current conditions, record the variation law of its potential with time, then study the charge and discharge performance of the electrode, and calculate its actual specific capacity. In the process of charge and discharge experiments under constant current conditions, the electrochemical response signal of the control current, when the control signal of the current is applied, the potential is the measured response signal, and the law of the potential change as a function of time is mainly studied.

2.4.5 Electrochemical impedance spectrum (EIS)

Typically, EIS measurements apply a small-amplitude AC signal with different frequencies to the electrochemical system and measure the ratio of the voltage to the current of the AC signal (this ratio is the impedance of the system) with the change of the sine wave frequency ω, or the phase angle of the impedance Φ with ω. Then, the kinetics of electrode process, electric double layer and diffusion are analyzed, and the mechanisms of electrode materials, solid electrolytes, conductive polymers and corrosion protection are studied. The electrochemical system is regarded as an equivalent circuit, which is composed of basic elements such as resistance (R), capacitance (C) and inductance (L) in different ways such as series and parallel. Through EIS, the composition of the equivalent

circuit and the size of each element can be measured, and the electrochemical meaning of these elements can be used to analyze the structure of the electrochemical system and the properties of the electrode process.

Chapter 3 0D-2D Heterostructures: MXene-Based Aerogel Anchored with Antimony Single Atoms and Quantum Dots for High-Performance Potassium-Ion Batteries

3.1 Introduction

The global landscape toward a low carbon economy has triggered the substantial growth in rechargeable batteries for electric vehicles (EVs) and smart grids. Nevertheless, the scarcity and uneven distribution of lithium reserves stimulate a compelling motivation to develop alternatives to state-of-the-art lithium-ion batteries.[1]-3 Potassium-ion batteries (PIBs) offer great promise because of the abundant potassium natural reserves, high ionic conductivity in conventional electrolytes, and similar chemistry to lithium.[4, 5] However, the large radius of K^+ causes large volume expansion and sluggish kinetics upon potassiation process, which become even more severe for alloying-type electrode materials.[168-170]

Antimony (Sb) as a typical alloying-type material has attracted increasing interest for potassium storage owing to its high theoretical capacity (660 mAh g^{-1}) compared to the intercalation-type anodes. However, the exceptional volume expansion derived from alloying reaction between K and Sb would pulverize the electrode and result in poor cycling performance.[171-173] Nanoengineering and further hybridizing the alloy-based nanomaterials with two-dimensional (2D) conductive matrix is a widely employed strategy to accommodate the volume change and improve the reaction kinetics.[174] A great number of zero-dimensional (0D) alloy-based nanoparticles (e.g., Si, Sb, Sn, Ge, P) dispersed on 2D substrates (e.g., graphene, MXene, C_3N_4) to form 0D/2D nanocomposites have been fabricated for high-performance alkali-ion batteries.[175-179]

In such circumstances, the 0D alloy-based nanoparticles mainly contribute to the high specific capacity and simultaneously offer space to buffer the volume change of individual nanoparticles.[180-182] Meanwhile, the 2D conductive matrixes provide continuous conductive networks for the anchored nanoparticles. Thus, the charge transfer between alloy-based nanoparticles and the support matrixes plays a critical role in the overall electrochemical performance.[183] Unfortunately, minimal attention has been paid to modulating the interaction between 0D active nanoparticles and 2D substrate. Inspired by the high efficiency for tuning the electronic metal-support interaction of electrocatalysts,[184-186] we proposed a similar strategy to accelerate the charge transfer in the 0D-2D connections to improve the potassium storage performance.

Herein, we designed and synthesized a hierarchical nanocomposite with antimony single atoms (SAs) and quantum dots (QDs) anchored on the $Ti_3C_2T_x$ MXene-based aerogel (Sb SQ@MA). The $Ti_3C_2T_x$ nanosheets with extensively exposed basal planes, abundant surface functional groups, and superior electronic conductivity and mechanical properties are ideal hosts for immobilizing 0D Sb SAs and QDs.[88,187-189] The Sb QDs contribute to the high potassium storage capacity while shortening the Na^+ transfer paths. More importantly, the incorporation of Sb SAs could enhance the interaction between Sb QDs and $Ti_3C_2T_x$ MXene, boost the charge transfer kinetics and improve the potassium adsorption capability at the interfaces. Besides, to further reinforce the electrode structural stability and conquer the inevitable restacking tendency of $Ti_3C_2T_x$ MXene, a graphene oxide (GO)-assisted 3D porous $Ti_3C_2T_x$-based aerogel is ingeniously constructed.[31] As a result, the Sb SQ@MA composite anode delivers a high reversible capacity of 521 mAh g^{-1} at 0.1 A g^{-1} and high capacity retention of 94% at 1 A g^{-1} even after 1,000 cycles.

3.2 Experimental

3.2.1 Materials synthesis

Synthesis of few-layered MXene ($Ti_3C_2T_x$). The $Ti_3C_2T_x$ was obtained by etching the MAX Ti_3AlC_2 material. Typically, 1 g of LiF was added into 10 ml of 9 M HCl solution under stirring. After the salt absolutely dissolved in the solution, 1 g of Ti_3AlC_2 powder was slowly added into the mixture. The reaction mixture was kept stirring for 24 h, then centrifuged and washed by distilled water several times until the pH of the supernatant arrived at 6. Subsequently, the sediment was re-dispersed in 200 ml DI water, which was sonicated under bubbling Ar for 1 h. Thereafter, the suspension was centrifuged at 3500 rpm for 1 h, and the supernatant was collected for further experiment. The supernatant was a stable colloidal solution of few-layered $Ti_3C_2T_x$ flakes; the concentration of the colloidal was evaluated by vacuum-assisted filtration of a certain volume of solution and measuring the weight after drying at room temperature overnight.

Synthesis of graphene oxide (GO). The GO was prepared by a modified Hummer method. Typically, natural graphite fakes (1.0 g, Sigma-Aldrich), $NaNO_3$ (1.0 g), and H_2SO_4 (98 wt%, 48 mL) were mixed and stirred in an ice bath, and 6 g of $KMnO_4$ was slowly added into the mixture. After mixing for 30 min, the ice bath was removed, and the mixture was further stirred for 48 h. Next, distilled water (90 mL) was added under stirring while the temperature was rose to 60 ^oC. Finally, H_2O (240 mL, 60 ^oC) was added, followed by the slow addition of H_2O_2 (15 mL, 30%). The final suspension was centrifuged, washed, and dialyzed with water to obtain graphene oxide. The as-synthesized graphene oxide was dispersed into distilled water and sonicated for 2 h to form a homogeneous colloidal solution.

Preparation of the Sb SQ@MA composite. 5 ml of $Ti_3C_2T_x$ MXene (3 mg ml^{-1}) colloidal solution and 10 ml of dissolved citric acid solution (0.1 M) were homogenously mixed under magnetic stirring. Then 0.4 mmol $SbCl_3$ (97%, Sigma-Aldrich) ethanol solution was dropwise added into the mixture to form a transparent solution, which was kept stirred for 1 h. Secondly, 5 ml of few-layer GO (3 mg ml^{-1}) was poured into the solution, and the mixture was sonicated for 10 mins under Ar bubbling before transferring to a Teflon-lined stainless-steel autoclave. Subsequently, the sealed reactor was placed at 120 ºC for 12 h to obtain a cylindrical precursor, which was washed by DI water and then freeze-dried under vacuum. Lastly, the dried material was calcined at 450 °C for 2 h under the 10% H_2/Ar atmosphere to get the final product.

Preparation of the Sb NP@MA composite, pure Sb nanoparticles, and $Ti_3C_2T_x$/graphene. The SbNPs@$Ti_3C_2T_x$ composite sample was synthesized *via* a similar route without the addition of citric acid as the chelating agent. Pure Sb nanocrystals were synthesized by the same procedures but using an equaling volume of DI water to substitute the $Ti_3C_2T_x$ and GO colloidal solution.

3.2.2 Materials characterization

The structure of samples was observed by the field-emission scanning electron microscopy (FE-SEM, Zeiss Supra 55VP) and scanning transmission electron microscopy (STEM, JEOL JEM-ARM200F). The XRD patterns were collected *via* a Bruker D8 Discovery X-ray diffractometer, and Raman spectra were obtained by a Renishaw inVia Raman spectrometer system (Gloucestershire, UK) using a 633 nm wavelength laser. Nitrogen-sorption measurements were conducted with a Micromeritics 3Flex surface characterization analyzer. XPS analysis was performed through an

ESCALAB250Xi (Thermo Scientific, UK) spectroscopy equipped with mono-chromated Al K alpha (energy 1486.68 eV).

3.2.3 Electrochemical measurements

The electrochemical performance of the materials was evaluated in CR2032-type coin cells with K metal foil as the counter/reference electrode, 40 μL of 1 M KFSI in ethylene carbonate (EC), and propylene carbonate (PC) (1:1, v/v) as the electrolyte and Celgard 2400 as the separator. The working electrodes were prepared by pasting a uniform aqueous slurry consisting of 70 wt% active material, 20 wt% carbon black, and 10 wt% carboxymethyl cellulose (CMC) onto a copper foil, and then vacuum drying at 80 ºC for 12 h. The typical loading of the tailored round electrode (14 mm in diameter) was around 1 mg cm^{-2}. Galvanostatic discharge/charge measurements were performed on a Neware battery testing system. The current densities and specific capacities were all calculated based on the mass of Sb in the electrodes. Cyclic voltammograms were collected in the voltage range of 0~2.5 V using a Biologic VMP3 workstation. Moreover, electrochemical impedance spectroscopy (EIS) analyses were performed by applying a potential amplitude of 5 mV to the cells in the frequency range from 100 kHz to 10 mHz.

3.2.3 Computational methods

All the theoretical calculations are performed within the Vienna Ab initio Simulation Package (VASP) based on density functional theory.[190,191] The electronic exchange-correlation interaction is described within the generalized gradient approximation (GGA) of optimized-Perdew–Burke–Ernzerhof (optPBE-vdW) calculation.[192] The interactions between the ion core and the valence electrons are modeled with projector augmented wave (PAW) potentials.[193] A plane-wave basis set with a kinetic cutoff energy of 400 eV is employed. The Brillouin zone (BZ) is sampled using 1×1×1 and 2×2×1 gamma

centered Monkhorst–Pack grids for the calculation of structural relaxation and electronic structures, respectively. The criteria for energy and atom force convergence are set to 10^{-4} eV per unit cell and 0.1 eV $Å^{-1}$, respectively. We consider two heterojunctions consisting of Sb (101) and (012) slabs on the $Ti_3C_2T_x$. For $Ti_3C_2T_x$/Sb (101), a 3×6 supercell of $Ti_3C_2T_x$ layer and a 2×4 supercell of Sb (101) layer is used, which lattice constants are 15.84 Å and 18.29Å along with *a* and *b* directions, respectively. In this model, 72 of C, 108 of Ti, and 64 of Sb atoms are included and different terminations of the $Ti_3C_2T_x$ (x=−O, −F, and −OH groups) were considered separately in the systems. For the Sb SAs incorporated model, two Sb atoms were used to substitute Ti atoms in the $Ti_3C_2T_x$ configuration. As for Ti_3C_2/Sb (012), a 4×4 supercell for the Ti_3C_2 layer and 1×4 supercell of Sb (012) slab is used with a lattice parameter of 21.93Å and 13.84Å along with *a* and *b* directions, respectively.

3.3 Results and Discussion

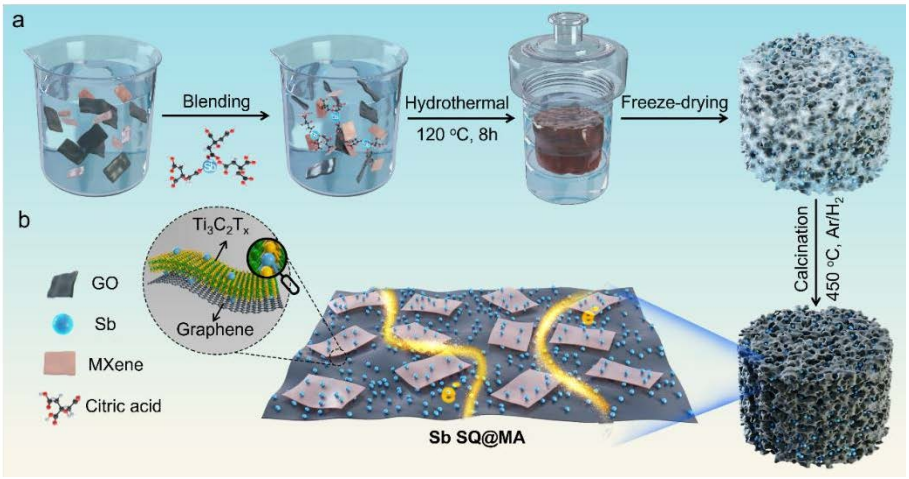

Figure 3.1 Schematic illustration of the (a) synthetic procedures and (b) structure features of Sb SQ@MA composite.

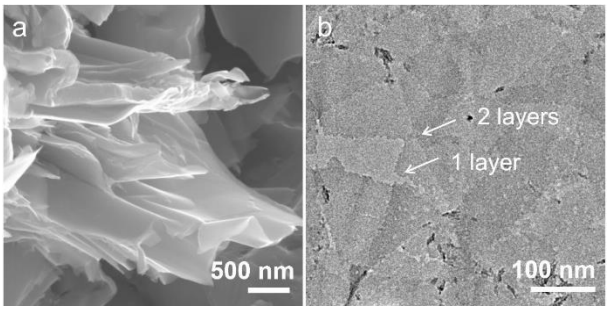

Figure 3.2 (a) SEM and (b) TEM images of the as-prepared $Ti_3C_2T_x$.

Figure 3.1a illustrates the synthetic route of the Sb SQ@MA composite. The facile one-pot hydrothermal strategy includes the following procedures: (i) homogeneous blending the raw materials and then (ii) preparation of the integrated 3D MXene based composite through the spatial confined hydrothermal procedure, (iii) followed by freeze-drying and calcination step. The $Ti_3C_2T_x$ nanosheets derived from an LiF/HCl-etching method possess Ti vacancies and rich surface functional groups (−OH, −F, and =O), which are favorable for electrostatically adsorbing Sb^{3+} and anchoring the single atoms (**Figure 3.2**).[194] The citric acid can prevent the instant formation of insoluble antimony hydroxides, and the strong chelation/complexation effect with Sb^{3+} results in a well-controlled Sb nucleation and growth, ensuring the co-existence of Sb single atoms and quantum dots.[195] In the hydrothermal strategy, graphene oxide (GO)-assisted 3D porous $Ti_3C_2T_x$ MXene hydrogel incorporated all the active materials via a self-convergence process, and an aerogel skeleton was obtained after freeze-drying.[196] The calcination treatment was conducted to decompose the citric acid, remove the excess surface terminations of the 2D matrix, and achieve the Sb single atoms and quantum dots (Sb SQ) homogenously decorated 3D porous MXene-based aerogel (MA) architecture (**Figure 3.1b**).

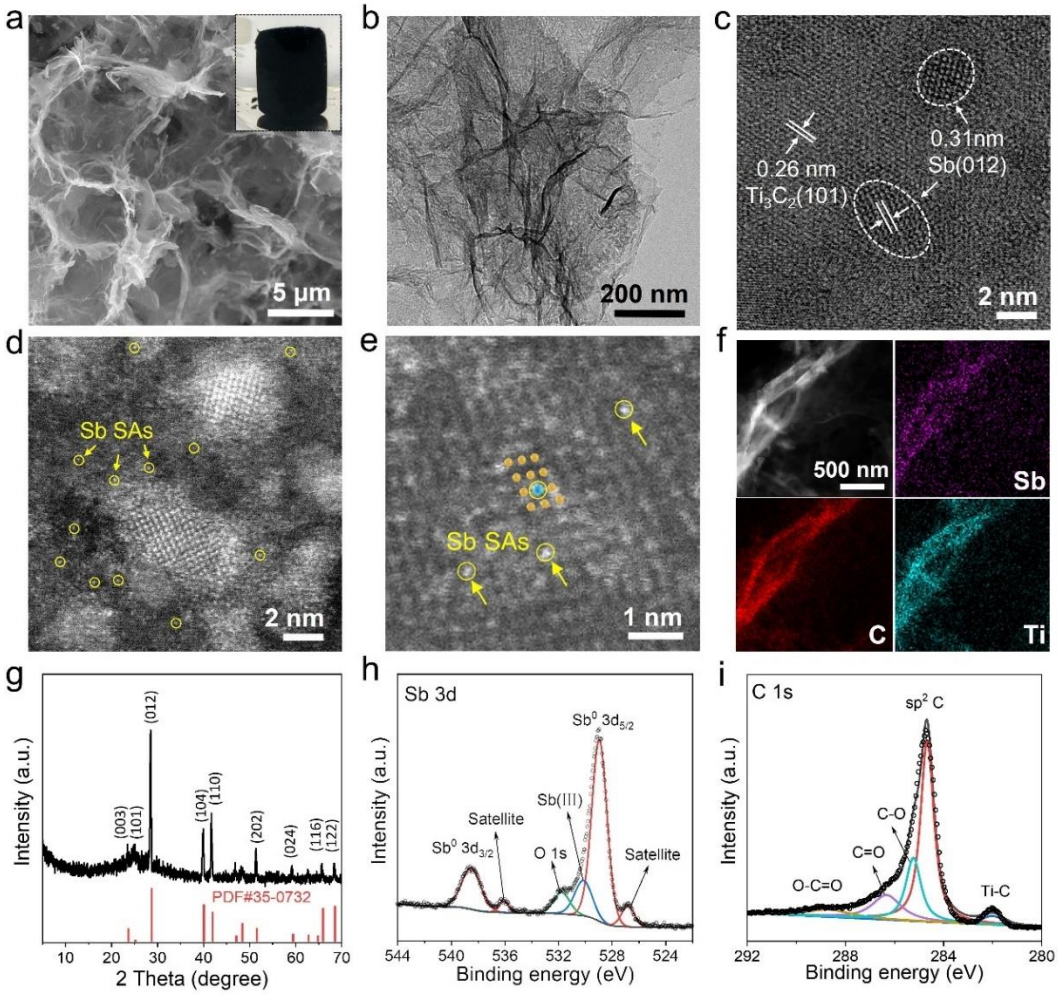

Figure 3.3 Physical characterizations of the Sb SQ@MA composite. (a) SEM image and (b) TEM image of the composite; the inset in Fig. 3.3a is the digital photo of the as-prepared composite aerogel. (c) HRTEM image and (d, e) High-angle annular dark-field (HAADF) images of the composite; the inset in Fig. 3.3e is schematic columns of atoms overlaid on the experimental image (orange and cyan balls represent Ti and Sb atoms, respectively). (f) STEM image and elemental mapping analysis of Sb, Ti, and C distribution. (g) XRD pattern and fitted high-resolution (h) Sb 3d and (i) C 1s XPS spectra.

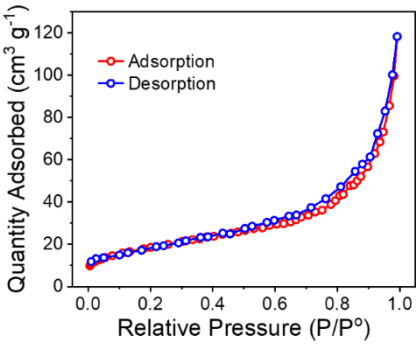

Figure 3.4 Nitrogen adsorption/desorption isotherms of the Sb SQ@MA composite. The surface area is calculated by Brunauer-Emmett-Teller (BET) method.

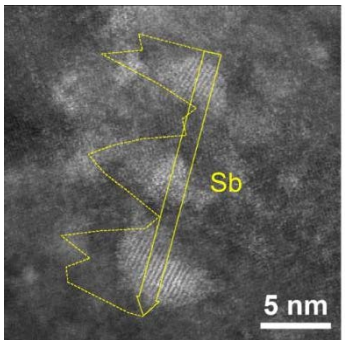

Figure 3.5 HAADF-STEM images of the Sb SQ@MA composite and the corresponding line profile of the Sb element (yellow arrow).

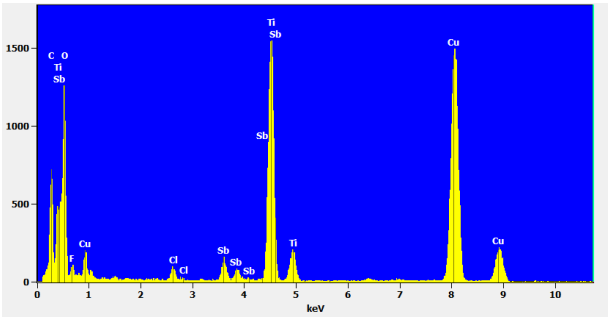

Figure 3.6 EDX spectrum of the Sb SQ@MA composite.

The scanning electron microscopy (SEM) and transmission electron microscopy (TEM) were conducted to investigate the structural features of the as-prepared Sb SQ@MA nanocomposite. As shown in **Figure 3.3a**, a classical macroporous structure of aerogel can be observed in the Sb SQ@MA composite. The porous architecture with a large

surface area of 67.2 m^2 g^{-1} would benefit electrolyte penetration (**Figure 3.4**). The low-magnification TEM image exhibits crumpled and grainy 2D nanosheets morphology, corresponding to the porous construction of aerogel decorated by the uniformly dispersed quantum dots (**Figure 3.3b**). The high-resolution TEM (HRTEM) image in **Figure 3.3c** reveals that the tiny quantum dots with adjacent lattice fringes of 0.31 nm belong to the (012) facet of the hexagonal Sb phase, and the substrate with a *d*-spacing of 0.26 nm corresponds to the (101) plane of $Ti_3C_2T_x$. Furthermore, Sb single atoms can be clearly detected in the corresponding high-angle annular dark-field scanning TEM (HAADF-STEM) image (marked by yellow circles in **Figure 3.3d**). The energy-dispersive X-ray (EDX) line profile confirms the existence of both crystalline and amorphous Sb quantum dots in average particle sizes of ~5 nm (**Figure 3.5**). Notably, the magnified HAADF image exhibits that Sb single atoms partially occupy Ti-vacancy sites and stay within the Ti_3C_2 lattice fringes (**Figure 3.3e**). This unique construction would tune the electronic properties of the composite and boost the charge transfer at the interface. The corresponding STEM and EDX elemental mapping images of Sb SQ@TA composite confirm the existence of Sb, Ti, O, C, F, and Cl components, further demonstrating the homogeneous distribution of Sb on the $Ti_3C_2T_x$-based aerogel matrix (**Figure 3.3f** and **Figure 3.6**).

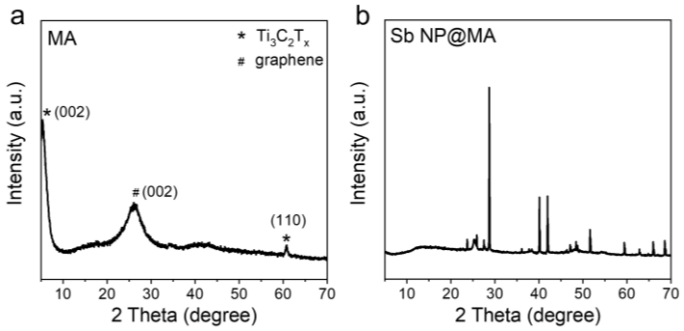

Figure 3.7 XRD patterns of the (a) MA ($Ti_3C_2T_x$ MXene based aerogel) and (b) Sb NP@MA materials.

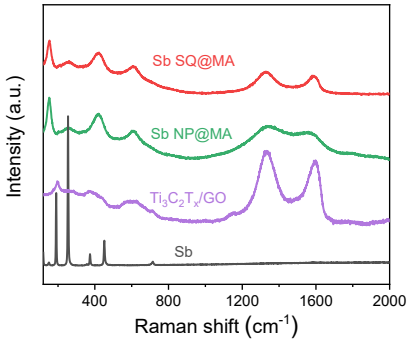

Figure 3.8 Raman spectra of the Sb, MA, Sb NP@MA, and Sb SQ@MA materials.

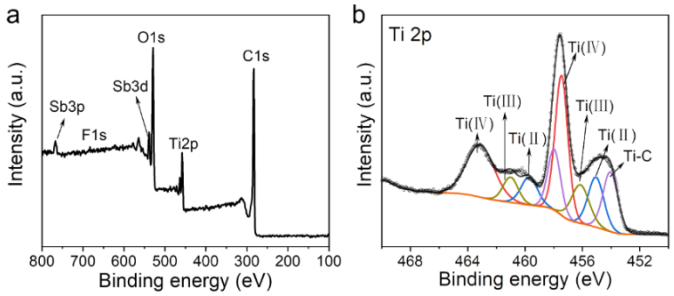

Figure 3.9 (a) Full survey and (b) Ti 2p XPS spectra of the Sb SQ@MA composite.

Table 3.1 XPS quantitative analysis results of the detected elements in the Sb SQ@MA composite.

Elements	C	Ti	Sb	O	F
Atomic%	60.86	9.12	17.18	12.38	0.46

The X-ray diffraction (XRD) pattern of the Sb SQ@MA composite exhibits that all the predominant peaks are well-matched with the standard PDF card of the hexagonal antimony (**Figure 3.3g**). The small peak at 5.3° corresponds to the (002) plane of $Ti_3C_2T_x$ MXene, and the broad peak at around 25° belongs to the graphitic carbon of reduced graphene oxide (**Figure 3.7a**). The Raman spectrum of Sb SQ@MA also displays combined characteristic peaks of Sb, $Ti_3C_2T_x$, and graphene (**Figure 3.8**). However, the peak intensity of Sb in the composite was remarkably reduced compared to bare Sb NPs, which can be attributed to the quantum effects of Sb SQ and the existence of MXene-

based aerogel at the outer surface. X-ray photoelectron spectroscopy (XPS) was employed to unravel the composition and valence state of component elements. As shown in **Figure 3.9a**, the full XPS survey of Sb SQ@MA composite presents the characteristic signals of Sb, O, Ti, C, and F elements. The quantified Sb element account is 17.18 at%, corresponding to 60.3 wt% in the Sb SQ@MA composite (**Table 3.1**). This value is very close to the computed theoretical value based on the experiment parameters (62 wt%). **Figure 3.3h** presents the high-resolution Sb spectrum of Sb SQ@MA, and the two major peaks at 528.9 and 538.5 eV can be ascribed to the Sb $3d_{5/2}$ and Sb $3d_{3/2}$ of metallic Sb, respectively. Additionally, the peak at 530.2 eV corresponds to the oxidation state of Sb(III), manifesting the presence of Sb single atoms. According to the peak area integral, it can be deduced that the atomic Sb in the composite is about 1.42 at% (4.9 wt%). In the C 1s spectrum, the peaks at 282.0 eV can be assigned to the Ti−C or Sb−C bonds of the Sb single atoms decorated $Ti_3C_2T_x$ MXene, and the C=C, C−O, and C=O bonds can be attributed to the reduced graphene oxide. Besides, some Ti^{4+} species were also detected in the high-resolution Ti 2p spectrum (**Figure 3.9b**), which may originate from the partial oxidation of $Ti_3C_2T_x$ during the hydrothermal treatment.

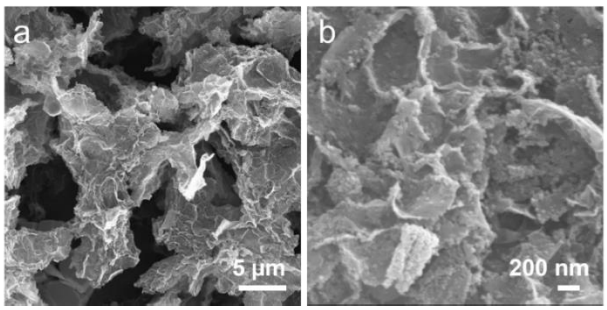

Figure 3.10 (a) Low-magnification and (b) high-magnification SEM images of the Sb NP@MA composite.

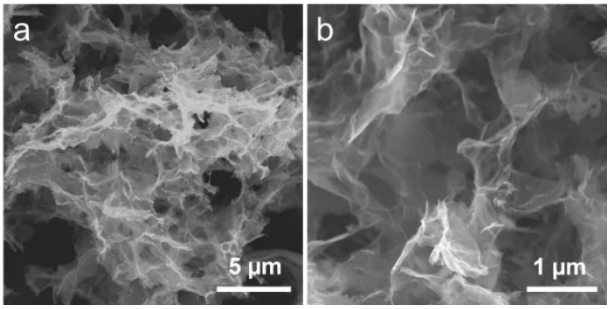

Figure 3.11 (a) Low-magnification and (b) high-magnification SEM images of the MA.

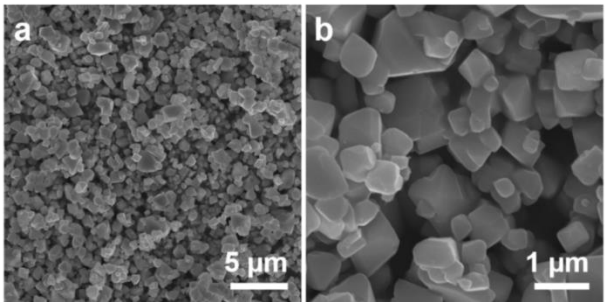

Figure 3.12 (a) Low-magnification and (b) high-magnification SEM images of the pure Sb nanoparticles.

For comparison, pure Sb nanoparticles anchored on $Ti_3C_2T_x$ MXene aerogel (Sb NP@MA) were synthesized through the same route without citric acid as the chelating agent. The Sb NP@MA presents a similar macroporous structure with Sb nanoparticles uniformly dispersed on the MXene nanosheets (**Figure 3.7b** and **3.10**). Besides, bare MA and Sb NPs were also prepared as references (**Figure 3.11-12**). Notably, the average nanoparticle size of Sb NPs is much larger than that in both Sb NP@MA and Sb SQ@MA due to the lack of double confinement from citric acid and $Ti_3C_2T_x$ MXene.

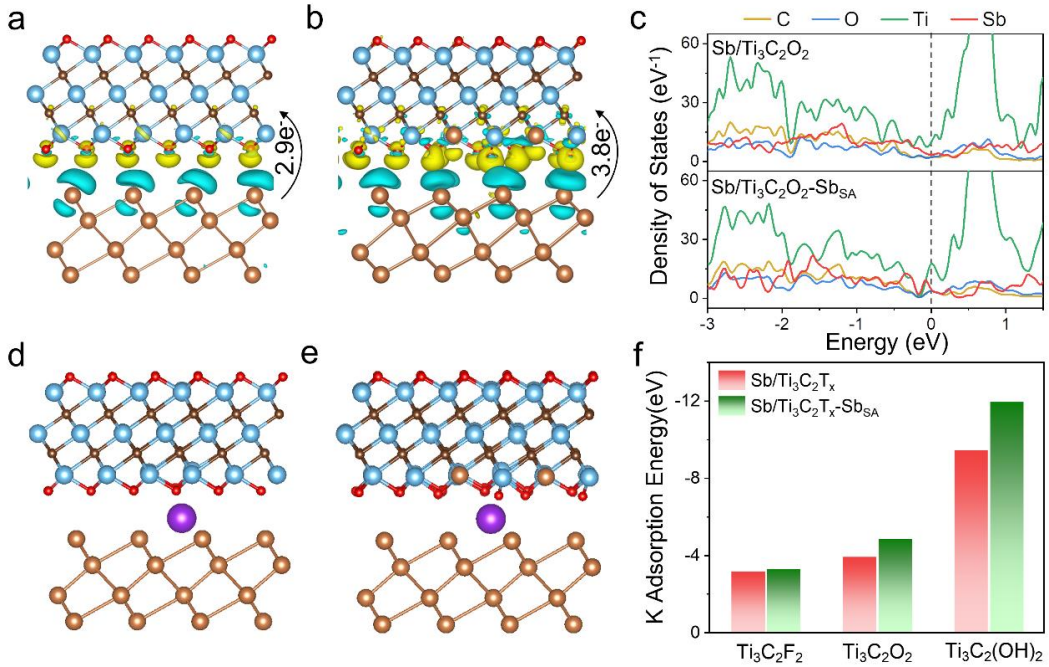

Figure 3.13 Charge density difference of (a) the $Sb/Ti_3C_2O_2$ and (b) $Sb/Ti_3C_2O_2$-Sb_{SA}. (c) Calculated DOS of the $Sb/Ti_3C_2O_2$ and $Sb/Ti_3C_2O_2$-Sb_{SA}. Side views of the most stable K adsorption positions at the interface of (d) $Sb/Ti_3C_2O_2$ and (e) $Sb/Ti_3C_2O_2$-Sb_{SA}; (f) the corresponding K adsorption energies. The cyan, dark brown, light brown, red, and purple balls represent Ti, C, Sb, O, and K atoms, respectively.

Till now, few reports have unravelled the roles of single atoms within such composite in determining the electrochemical energy storage performance. Thus, density functional theory (DFT) calculations were first applied to investigate the effects of single atoms on the electronic properties of the Sb SQ@MA composite. $Ti_3C_2T_x$ MXene terminated with =O, −F, and −OH groups were considered separately to simplify the computing system.[197] **Figure 3.13a** and **b** show the optimized structure configurations and charge density difference (CDD) of the $Sb/Ti_3C_2O_2$ and $Sb/Ti_3C_2O_2$-Sb_{SA}, respectively. The results display that charge mainly distributes near the interface of both heterostructure systems. Meanwhile, the Barder charge analysis exhibits that 3.8 e^- is transferred from Sb to $Ti_3C_2O_2$-Sb_{SA} substrate, higher than the charge transfer numbers in the $Sb/Ti_3C_2O_2$

model (2.9 e^- transferred from Sb to $Ti_3C_2O_2$). Similar improved charge transfer phenomena were disclosed in the Sb/$Ti_3C_2F_2$-Sb_{SA} and Sb/$Ti_3C_2(OH)_2$-Sb_{SA} models as well (**Figure 3.14**). Moreover, the density of states (DOS) in **Figure 3.13c** displays that the presence of single atoms alters the Ti and Sb states near the Fermi level, manifesting the enhanced interaction between Sb and $Ti_3C_2O_2$.

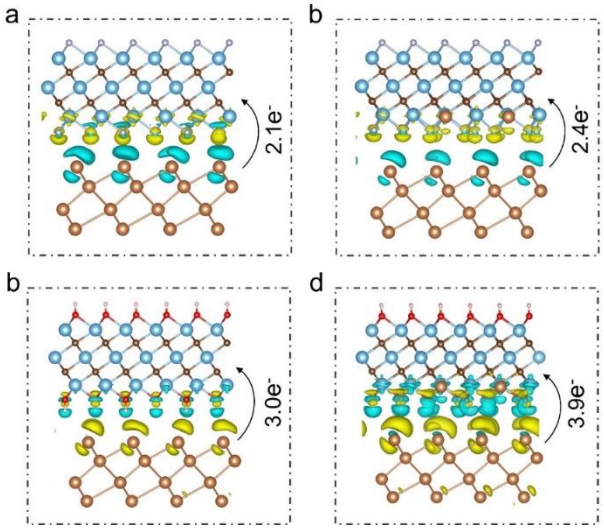

Figure 3.14 Charge density difference of (a) Sb/$Ti_3C_2F_2$, (b) Sb/$Ti_3C_2F_2$-Sb_{SA}, (c) Sb/$Ti_3C_2(OH)_2$ and (d) Sb/$Ti_3C_2(OH)_2$-Sb_{SA}. The cyan, light cyan, dark brown, light brown, red, and white balls represent Ti, F, C, Sb, O, and H atoms, respectively.

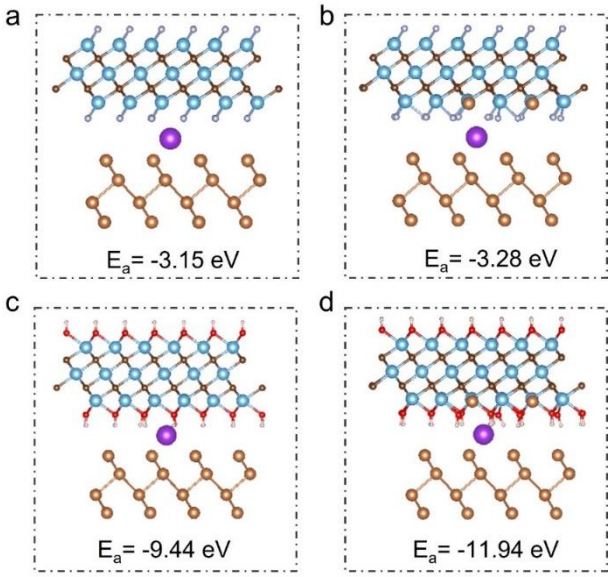

Figure 3.15 Side views of the most stable K adsorption positions and corresponding adsorption energies at the interface of (a) $Sb/Ti_3C_2F_2$, (b) $Sb/Ti_3C_2F_2$-Sb_{SA}, (c) $Sb/Ti_3C_2(OH)_2$ and (d) $Sb/Ti_3C_2(OH)_2$-Sb_{SA}. The cyan, light cyan, dark brown, light brown, red, white, and purple balls represent Ti, F, C, Sb, O, H, and K atoms, respectively.

The impact of Sb single atoms on the K^+ storage capability was also evaluated from an atomic viewpoint. **Figures 3.13d** and **e** display the most stable K adsorption positions at the interfaces of $Sb/Ti_3C_2O_2$ and $Sb/Ti_3C_2O_2$-Sb_{SA}, respectively. The K adsorption configurations in the −F and −OH terminated MXene-based hybrids are exhibited in **Figure 3.15**. The computed adsorption energies are −3.28 eV ($Sb/Ti_3C_2F_2$-Sb_{SA}), −4.80 eV ($Sb/Ti_3C_2O_2$-Sb_{SA}) and −11.94 eV ($Sb/Ti_3C_2(OH)_2$-Sb_{SA}), which are lower than the SAs-free counterparts (**Figure 3.13f** and **3.14**). The results indicate that the decoration of Sb single atoms enhances the K absorption capability of the composite, thereby benefiting the K uptake during the electrochemical reaction. Therefore, the incorporation of Sb single atoms is expected to positively influence accelerating the reaction kinetics of Sb SQ@MA nanocomposite and contribute to the overall electrochemical performance in PIBs.

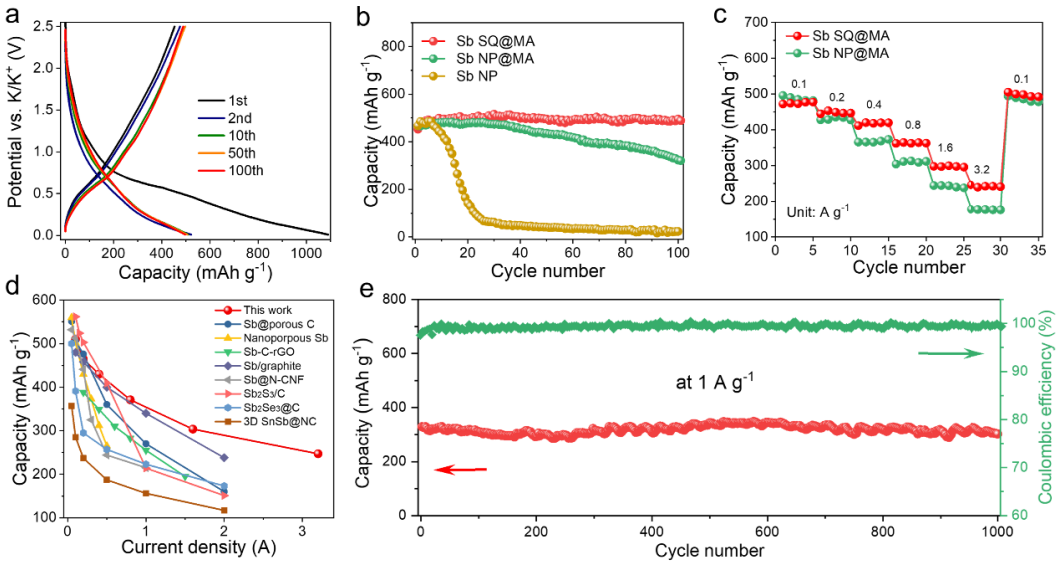

Figure 3.16 Potassium storage performance of the as-prepared electrode materials. (a) Selected charge-discharge curves of the Sb SQ@MA composite anode at 0.1 A g^{-1}. (b) Cycling performance of the Sb, Sb NP@MA, Sb SQ@MA anodes at 0.1 A g^{-1}. (c) Rate performance of the Sb NP@MA, Sb SQ@MA electrode. (d) Comparison of the rate performance of the Sb SQ@MA with other reported Sb-based anodes in PIBs. (e) Long-term cycling performance of the Sb SQ@MA.

The potassium storage performances of the as-prepared materials were evaluated combining with the electrolyte consisting of 1 M KFSI in ethylene carbonate (EC) and propylene carbonate (PC) (1:1, v/v) due to its positive effects on the forming stable solid-electrolyte interface (SEI) in alloy-based anodes.[198-200] As shown in **Figure 3.16a**, the Sb SQ@MA electrode delivered a high reversible capacity of 521 mAh g^{-1} at a current density of 0.1 A g^{-1}. While the pristine $Ti_3C_2T_x$/graphene anode only presents a negligible capacity of 62 mAh g^{-1} at the same current (**Figure 3.17**), suggesting that the Sb component makes a major contribution to the high capacity of Sb SQ@MA. Additionally, the discharge and charge curves of Sb SQ@MA are nearly consistent from the 2nd to 100th cycles, indicating the good structural stability of the composite. On the contrary, despite the bare Sb electrode achieving a charge capacity of 486 mAh g^{-1} at the first cycle

(**Figure 3.18**), the capacity rapidly degraded to 69 mAh g^{-1} after only 20 cycles owing to the severe pulverization of the Sb electrode during cycling. Although the Sb NP@MA anode exhibits a better cycling performance than the bare Sb nanocrystals, an evident capacity dropping was observed starting from the 40th cycle (**Figure 3.16b**).

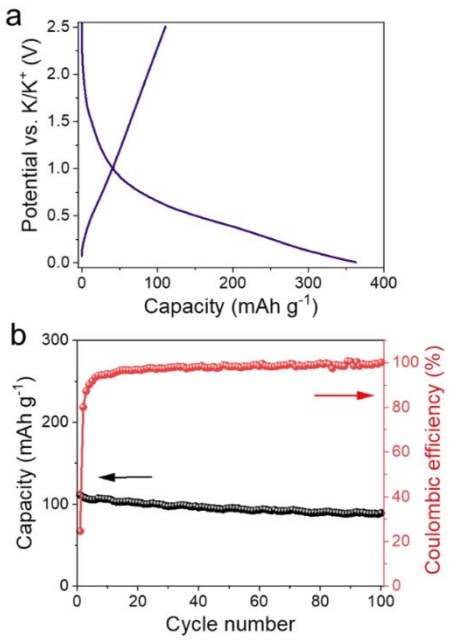

Figure 3.17 (a) First discharge and charge profiles and (b) cycling performance of the $Ti_3C_2T_x$/graphene electrode at a current density of 0.1 A g^{-1}.

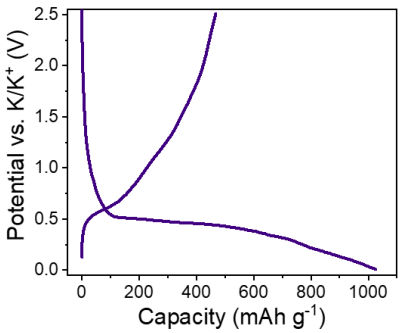

Figure 3.18 First discharge and charge profiles of Sb electrode at 0.1 A g^{-1}.

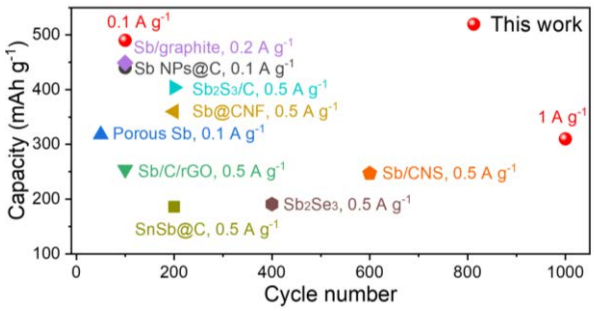

Figure 3.19 Comparison long-term cycling performance of the Sb SQ@MA with some other reported Sb-based anodes, including Sb/graphite,[201] Sb NPs@C,[173] Sb_2S_3/C,[202] Sb@CNF,[203] porous Sb,[204] Sb/C/rGO,[205] Sb_2Se_3,[206] Sb/CNS,[207] and SnSb@C[100] composites.

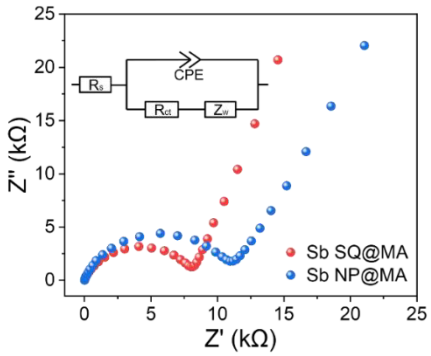

Figure 3.20 Nyquist plots of the Sb SQ@MA and Sb NP@MA composites; inset is the corresponding equivalent circuit to fit the results. R_s reflects the resistance of cell components and the electrolyte, R_{ct} represents the charge transfer impedance; CPE is a constant-phase element of the electrolyte and electrode interface, which accounts for the depressed semicircle in the measured spectra; and Z_w is Warburg impedance, which accounts for the inclined line and reflecting sodium ion transfer process in the electrode materials.

Figure 3.16c shows the rate performance of Sb SQ@MA and Sb NP@MA composite, and the Sb SQ@MA anode delivered a capacity of 447, 419, 364, 299, and 246 mAh g^{-1} at the current density of 0.2, 0.4, 0.8, 1.6, and 3.2 A g^{-1}, respectively. When the current

reverses to 0.1 A g^{-1}, the capacity fully recovers to 499 mAh g^{-1}. The high-rate performance of Sb SQ@MA not only exceeds the Sb NP@MA but also outperforms most of the previously reported Sb-based nanocomposites, such as Sb@porous carbon composite,[208] nanoporous Sb,[204] Sb carbon spheres with graphene (Sb-C-rGO),[209] Sb/graphite,[210] Sb@N-doped carbon nanofiber (Sb@N-CNF),[211] Sb_2S_3/C,[212] Sb_2Se_3/C,[213] and 3D SnSb@NC (**Figure 3.16d**).[214]

Figure 3.16e presents the cycling performance of the Sb SQ@MA anode, which retains a capacity of 314 mAh g^{-1} at 1 A g^{-1} after 1,000 cycles (94% of capacity retention). The high capacity and excellent cycling performance are competitive compared to other Sb-based anode materials (**Figure 3.19**). Electrochemical impedance spectroscopy (EIS) analysis was performed to evaluate the charge transfer kinetics of the composite electrodes (**Figure 3.20**). The Sb SQ@MA anode shows a smaller charge transfer resistance (R_{ct} = 8.16 kΩ) than that of the Sb NP@MA electrode (10.94 kΩ), which is consistent with the theoretical predictions.

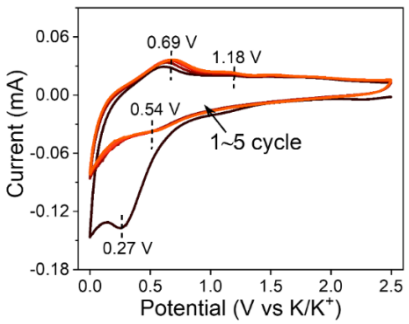

Figure 3.21 Initial five cyclic voltammetry curves of the Sb SQ@MA electrode at a scan rate of 0.1 mV s^{-1}.

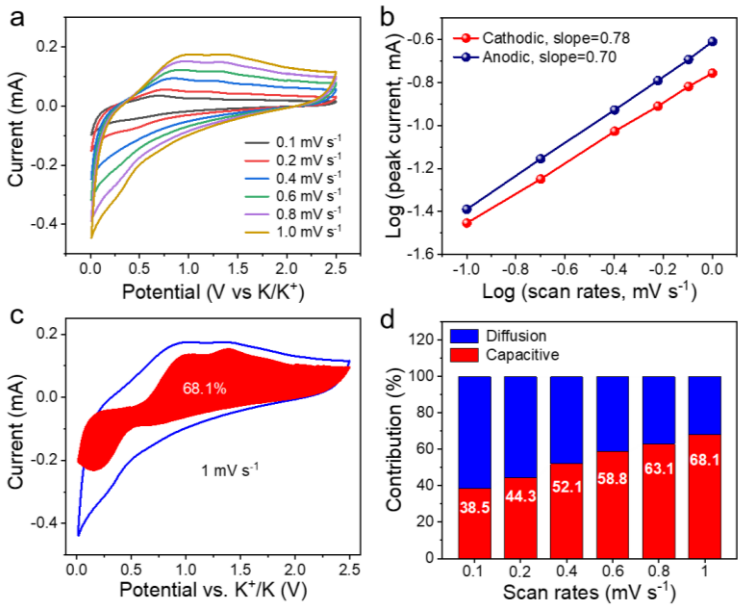

Figure 3.22 Electrochemical reaction kinetics analysis of the Sb SQ@MA composite. (a) CV curves at different scan rates. (b) Relationship between peak currents and scan rates. (c) CV profile collected at 1 mV s^{-1} and illustration of capacitive (red area). (d) Chart of capacitance- and diffusion-controlled contribution ratios at different scan rates.

Cyclic voltammetry (CV) profiles were collected to understand the electrochemical properties of the composite electrode. **Figure 3.21** presents the CV curves of Sb SQ@MA anode in the initial five cycles at a scan rate of 0.1 mV s^{-1}. The prominent reduction peak at around 0.27 V in the first scan disappeared in the subsequent cycles, assigned to the electrode material activation and formation of the solid-electrolyte interface (SEI). In the following cycles, the CV curves are almost overlapped, suggesting the good reversibility of the electrochemical reactions. The broad reduction peaks centered at 0.54 V can be attributed to the alloying reaction between Sb nanoparticles and K^+, and the oxidation peaks at 0.69 V and 1.18 V can be ascribed to the stepwise dealloying processes. Additionally, the CV curves at various scan rates were measured to study the electrochemical behaviors of the composite electrode, and the results indicate that Sb SQ@MA is subject to a mixed diffusion and capacitance dominated reaction kinetics

(**Figure 3.22**). Based on the relationship between the peak currents (i) and scan rates (v), $i = av^b$, the b value representing the charge storage mechanism can be obtained from **Figure 3.22a**. When b=0.5, the reaction is completely a diffusion-controlled process; when b=1, it is a capacitance-controlled process. As shown in **Figure 3.22b**, the b value of Sb SQ@MA is 0.78, indicating a mixed diffusion and capacitance-dominated reaction kinetics.

The specific diffusion and capacitance contribution at a fixed scan rate can be quantified through the following equation: $i(V) = k_1v + k_2v^{1/2}$, where $i(V)$, k_1v and $k_2v^{1/2}$ represent the current at a fixed voltage, capacitive current, and ion-diffusion current, respectively. **Figure 3.22c** exhibits a typical CV curve for capacitive current (red region) in comparison to total current (blue line) at 1 mV s^{-1}. It can be seen that the diffusion process becomes predominant at around 0.51 V, corresponding to the alloying-dealloying process of Sb quantum dots. By contrast, the capacitive process dominants the charge storage behavior at other voltage regions. The capacitive contribution at a fixed scan rate can be obtained by computing the capacitive current area percentage in the total CV region. The capacitive contributions of the composite electrodes gradually grow along with the increased scan rates, and it reaches 68.2% at 1 mV s^{-1}, implying a pseudocapacitance-dominated behavior of Sb SQ@MA composite at high rates (**Figure 3.22d**).

DFT calculation was further utilized to understand the structural evolution of Sb upon potassiation. According to the binary phase diagram of K−Sb alloy, the formation energies of four intermediate phases (KSb_2, KSb, K_5Sb_4, and K_3Sb) were evaluated. As shown in **Figure 3.23a**, the formation energies show an inverse correlation with the atomic ratio of K in K−Sb alloys. The lowest formation energy of −1.43 eV (per Sb atom) is obtained at the K_3Sb phase, which indicates that K_3Sb is the thermodynamically stablest phase as

well as the most favorable final discharge product.

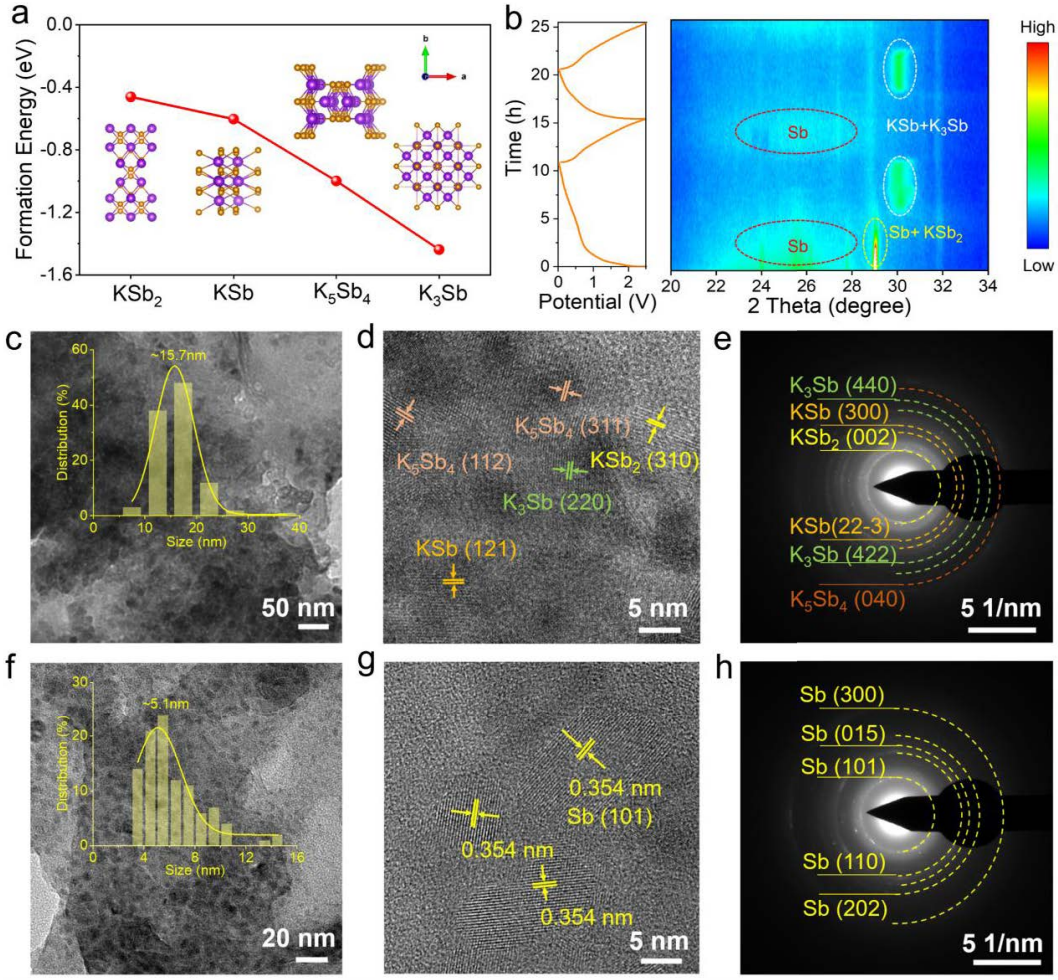

Figure 3.23 Mechanism analysis of the Sb SQ@MA anode. (a) DFT calculated the formation energies (per Sb atom) of different Sb−K alloys. (b) *In-situ* XRD patterns of the composite electrode with the corresponding discharge-charge profiles. *Ex-situ* TEM, HRTEM with corresponding SAED patterns of the composite electrode at (c-e) fully discharged and (f-h) charged states. The insets in Figures c and f are statistics of the particle size in the corresponding images.

The phase evolution of the Sb SQ@MA electrode was also revealed by *in-situ* XRD technique. **Figure 3.23b** shows the galvanostatic discharge-charge profiles of the composite electrode in the first two cycles and the contour plot of the corresponding XRD patterns in the 2θ range of 20°~34°. During the initial discharge process, the peak

intensities of the hexagonal Sb phase became weaker and weaker along with the potassiation process and disappeared at around 0.3 V, indicating that Sb quantum dots fully transformed to K_xSb alloys. At the same time, a broad peak centered at 30.1° was emerged, which can be assigned to the (11-4) facet of KSb phase and (220) facet of K_3Sb alloy. The HRTEM image and the corresponding SAED pattern of discharged Sb SQ@MA electrode exhibit a mixture of K−Sb alloys, including KSb_2, KSb, K_5Sb_4, and K_3Sb (**Figure 3.23d, e**).[59] The above results suggest that the potassiation of Sb SQ@MA is a stepwise alloying process from K-deficient alloys to K-rich K_xSb alloys, which is in accordance with the theoretical calculation results.

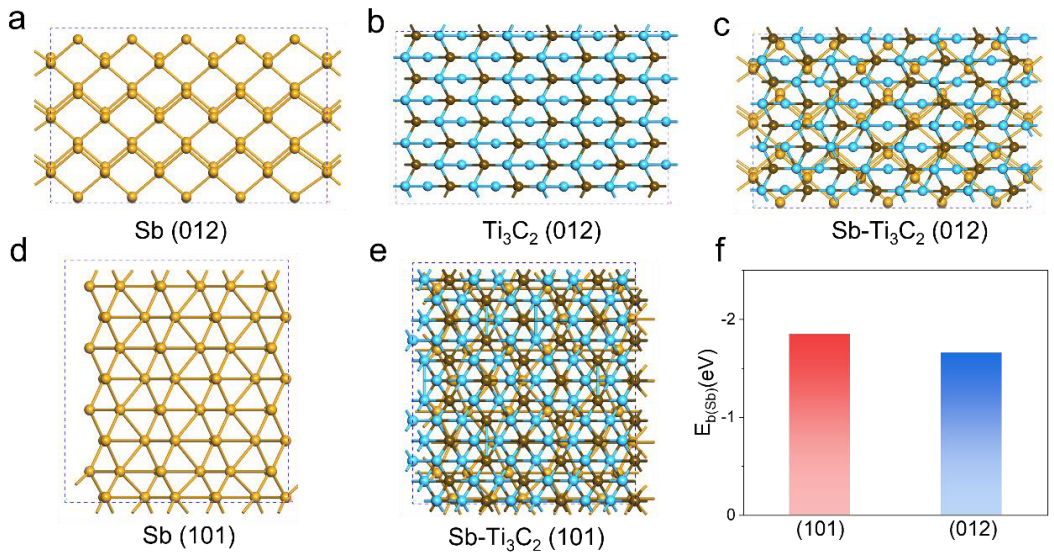

Figure 3.24 Theoretical study of the structural stability of Sb-Ti_3C_2 composite in (101) and (012) planes. Top views of the (a) Sb, (b) Ti_3C_2 and (c) Sb-Ti_3C_2 in (012) plane. Top views of the (d) Sb and (e) Sb-Ti_3C_2 in (101) plane. (f) Formation energies per Sb atom of the Sb-Ti_3C_2 in (012) and (101) plane, respectively.

During charging, the peaks belonging to K_xSb alloys gradually vanished, but no sharp peaks belonging to the (012) plane of hexagonal Sb were detected anymore. Instead, a broad peak in the range of 22°~29° appeared thereafter, implying that the Sb crystals were converted to amorphous phase or low crystallinity species after

potassiation/depotassiation. The (101) planes of Sb instead of (012) planes in the original composite were observed in the HRTEM image of the charged electrode (**Figure 3.23g**), which could be ascribed to the different orientation growth of Sb crystals during the dealloying process. This assumption was verified by the theoretical calculation, where the (101) facet of Sb in the Sb SQ@MA composite has lower formation energy compared to the (012) facet (**Figure 3.24**). **Figure 3.23e** exhibits the SAED pattern of the charged electrode, which can be well indexed as hexagonal Sb phase.

In the second discharge cycle, the broad peak belonging to Sb gradually disappeared with the appearance of K_xSb alloys, and the phase evolution in the charge process is nearly the same as the first cycle. These results further demonstrate the good reversibility of Sb SQ@MA upon cycling. Additionally, the statistics on particle size exhibit that the discharged K_xSb NPs have an average size of 15.7 nm (**Figure 3.23c**), which is three times than the charged Sb NPs (~5.1 nm, **Figure 3.23f**). This result is within the range of theoretical prediction, where 400% of volume expansion occurs when 100% of Sb crystals are converted to K_3Sb. The large surface area of MXene-based aerogel ensures ample room for the structural variation of the monodispersed Sb quantum dots, thereby maintaining the structural integrity and leading to the excellent cycling performance of PIBs.

3.4 Conclusions

A hierarchical 3D nanocomposite with antimony single atoms and quantum dots embedded in $Ti_3C_2T_x$ MXene-based aerogel (Sb SQ@MA) was synthesized via a facile one-pot hydrothermal route. Due to the double confinement from the MXene-based aerogel and chelation effects between citric acid and Sb^{3+}, the Sb single atoms and quantum dots were achieved simultaneously. The DFT calculations reveal that atomic

dispersed Sb can effectively promote the charge transfer between Sb quantum dots and MXene substrate and enhance K adsorption capabilities at the interface. Meanwhile, the 3D porous GO-assisted MXene-based aerogel not only offers fast electron transport pathways but also facilitates the electrolyte impregnation and reinforces the structural stability of the composite electrode. Benefited from these synergistic effects, the Sb SQ@MA anode exhibits superior electrochemical performance in PIBs. In addition, *in-situ* XRD and *ex-situ* TEM characterizations unravel the reaction mechanism and confirm the advantages of the rationally designed architecture. Our findings shed light on the design and development of unique structured single atom-based materials for electrochemical energy storage and conversion.

Chapter 4 1D-2D Heterostructures: A Stable Conversion and Alloying Anode for Potassium-Ion Batteries – A Combined Strategy of Encapsulation and Confinement

4.1 Introduction

The ever-increasing demands in electronic devices, electric vehicles, and large-scale electrical power systems have promoted the development of high-energy-density, low-cost, and large-scale energy storage devices.[7,215,216] Potassium-ion batteries (PIBs) are considered as a low-cost energy storage system owing to the natural abundance of potassium resources and close redox potential of K/K^+ to that of Li/Li^+ in the counterpart lithium-ion batteries (LIBs).[217-221] In particular, the successful intercalation of K^+ ions into graphitic anodes further promotes the practical development of PIBs.[222-224] Whereas, the obtained capacity is usually limited to less than 250 mA h g^{-1}, due to the intercalation mechanism.[225,226] Compared to intercalation-type anodes, the conversion/alloying-based anodes can deliver much higher capacities owing to their multi-electron transfer reactions.[227-232] However, the inherent large volume variations result in the pulverization of materials, leading to a poor cycling performance.[233] Considering a much larger size of K^+ ions (1.38 Å) than Li^+ ions (0.68 Å), the pulverization issue of conversion/alloying-based anodes is more severe in PIBs (**Figure 4.1a**).[234] For example, antimony (Sb) anodes suffer from a vast volume expansion of 407 % by forming a potassiated K_3Sb alloy. This value is nearly 3 times larger than that in the lithiation process with a comparable lithiation product of Li_3Sb alloy.[235] Thus, the main challenge for stable conversion/alloying-based anodes in high-performance PIBs is to buffer the unavoidable volume expansion and maintain the structural integrality during the repeated insertion and extraction of K^+ ions.

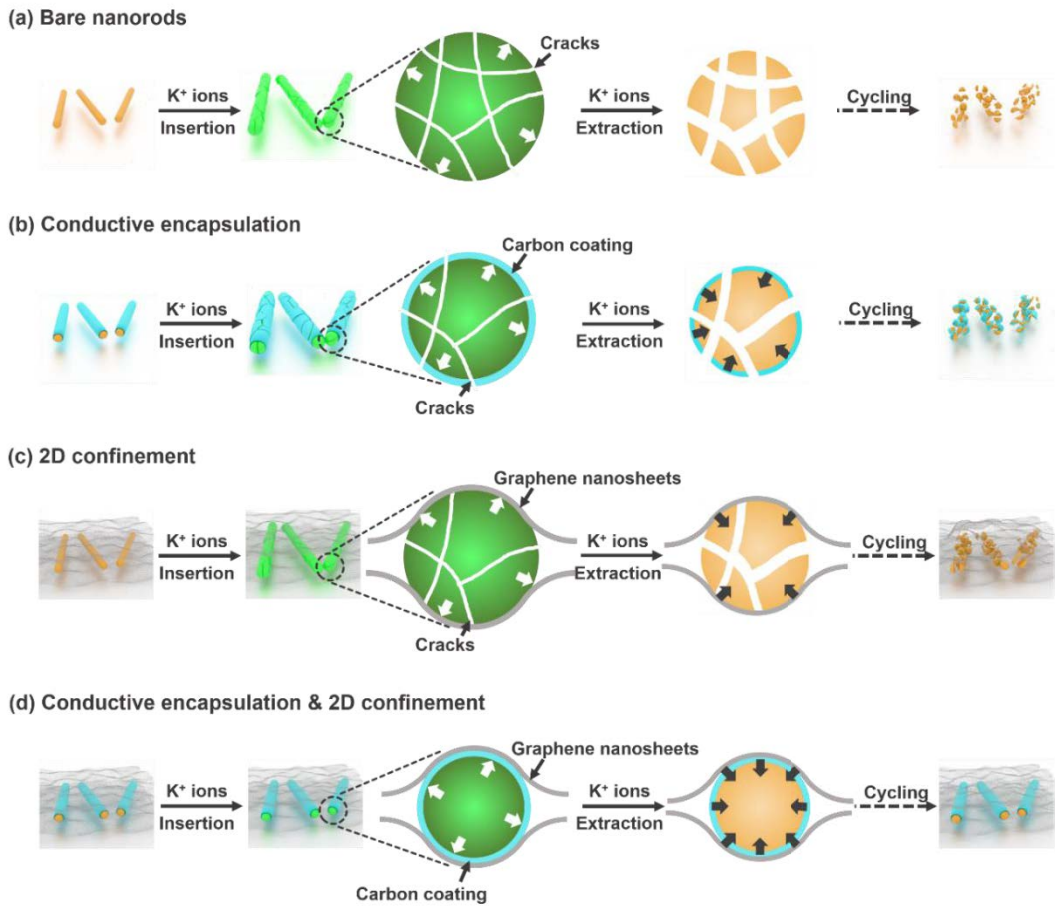

Figure 4.1 Schematics of the electrochemical process in various configurated conversion/alloying anode. (a) Bare nanorods undergo large volumetric change and tend to pulverize during cycling. (b) Conductive encapsulation provides a protective coating. However, the huge volume changes still induce cracking of the carbon layer and further structural damage. (c) Confinement between flexible graphene nanosheets could accommodate the volume change. However, the structure collapse is still unavoidable. (d) By combining the encapsulation and confinement, both the carbon coating layer and graphene nanosheets help to buffers volume expansion, resulting in well-maintained structural stability within cycling.

To this end, conductive encapsulation, mostly through carbon coating, is one of the most effective approaches to enhance the cycling performance of electrode materials. The surfaces of conversion/alloying-based anodes are coated by a rigid layer of conductive

carbon, which can decrease the interfacial resistance and improve the overall electronic conductivity.[228,236] However, the considerable volume changes originated from the insertion of bulky K^+ ions still induce cracking of the carbon layer and structural damage, which further lead to the electrochemical performance fading (**Figure 4.1b**).[237,238] To overcome the large volume change of conversion/alloying-based anodes, many efforts have been focused on the two-dimensional (2D) confinement strategy.[239-242] For example, stabilization of the nanomaterials between the interlayer galleries of graphene nanosheets has been successfully implemented.[243-245] The volume change could be accommodated by the flexible graphene nanosheets to some extent.[246-249] However, the structure collapse of the electrode materials is still unavoidable due to the phase transitions via conversion and/or alloying processes.[250] The pulverized nanostructures further aggregated, leading to a capacity fading (**Figure 4.1c**). To realize a robust and high structural stability of the large-volume-change electrode materials, combination of conductive encapsulation and 2D confinement could be an efficient strategy. The conversion/alloying-based anode materials are not only encapsulated by a conductive carbon layer but also confined between the interlayer of graphene nanosheets. Both the carbon coating and graphene layers are integrated via chemical interactions, forming a multifunctional protective buffer to improve the overall conductivity, prevent the aggregation of nanosized anodes and maintain the structural integrity. Consequently, a superior stable PIB is expected to be achieved (**Figure 4.1d**).[251-253] There are some successful examples of the combination strategy to solve the volumetric variation for conversion-type anode materials in LIBs and sodium-ion batteries (SIBs). Dou *et al.* designed a 3D porous electrode consisted of N-doped graphene scrolls encapsulated 1D MnO nanowires with the confinement of 2D N-doped graphene ribbons.[254] This architecture well accommodated the volume expansion of MnO in LIBs. Mai *et al.*

prepared a multidimensional synergistic nanoarchitecture (0D⊂1D⊂3D) to restrict the volume change of V_2O_3 anodes in SIBs.[255] Nevertheless, there was no report for conversion/alloying anode materials in PIBs.

In this work, we demonstrated a superior stable cycling performance of a conversion/alloying anode material, antimony selenide (Sb_2Se_3), for PIBs through combining conductive encapsulation of an N-doped carbon (NC) and 2D confinement of reduced graphene oxide (rGO) nanosheets. The obtained NC-encapsulated and rGO-confined Sb_2Se_3 nanorod composites (Sb_2Se_3@NC@rGO) exhibited significantly improved cycling stability and rate capability as anodes for PIBs. Further, *in-situ* X-ray diffraction (XRD) and *ex-situ* electron microscopy observations were conducted to reveal the structural revolution and understand the fundamental mechanisms of the improved high performance.

4.2 Experimental Section

4.2.1 Materials synthesis

All chemical reagents, including antimony (III) chloride ($SbCl_3$), PEG-400, selenium powder (Se), sodium borohydride ($NaBH_4$), dopamine hydrochloride, tris(hydroxymethyl)aminomethane (tris-buffer) and absolute ethanol were purchased from Sigma Aldrich and used directly without further purification. Graphene oxide (GO) was purchased from Sinocarbon Co Ltd in China. Deionized water was self-made in our lab.

i) Bare antimony selenide (Sb_2Se_3) nanorods. A modified typical solvothermal method was applied for synthesis of uniform Sb_2Se_3 nanorods. 2 mmol $SbCl_3$ was dissolved in 20 mL deionized water via constant stirring until obtaining a clear solution A. For solution B, firstly, 6 mmol $NaBH_4$ was added into 10 mL nitrogen-purged absolute ethanol to form

a suspension, and then 3 mmol Se powder was slowly put in to form a clear solution under nitrogen protection. Next, solution B was dropwise transferred into solution A under intense stirring. The mixture was treated through a solvothermal method at 200 °C for 12 h in a Teflon reactor. The obtained dark brown sediment was collected by filtration and washed several times using absolute ethanol and deionized water before dried overnight at 80 °C under vacuum. The prepared pure Sb_2Se_3 was used as a precursor for coated composites.

ii) N-doped carbon (NC)-encapsulated Sb_2Se_3 nanorod composites (Sb_2Se_3@NC). In the beginning, a 10 mM Tris-buffer solution was prepared, and its pH value was adjusted to about 8.50 using concentrated hydrochloric acid. The as-prepared pure Sb_2Se_3 (100 mg) was dispersed in 150 mL Tris-buffer solution by sonication. Then 50 mg dopamine hydrochloride powder was quickly added, and the mixture was continuously stirred for 16 h. The poly(dopamine) coated Sb_2Se_3 was collected by filtration and washed using deionized water and absolute ethanol, and Sb_2Se_3@NC was obtained via a following calcining procedure at 550 °C under Argon for 6 h with a heating rate of 2 °C /min.

iii) Reduced graphene oxide (rGO)-confined Sb_2Se_3 nanorod composite (Sb_2Se_3@rGO). 60 mg as-prepared pure Sb_2Se_3 and 20 mg GO nanosheets were dispersed in 20 mL and 10 mL deionized water separately by sonication. Then the mixture of two solutions was sequentially sonicated for over 2 h before frozen drying at −50 °C for 36 h. Sb_2Se_3@rGO was prepared by following a similar calcining procedure as Sb_2Se_3@NC.

iv) NC-encapsulated and rGO-confined Sb_2Se_3 nanorod composites (Sb_2Se_3@NC@rGO). Using poly(dopamine) coated Sb_2Se_3 as the precursor and repeating the synthesis procedure of Sb_2Se_3@rGO, we gained Sb_2Se_3@NC@rGO.

4.2.2 Materials characterization

X-ray diffraction (XRD) via a Bruker D8 Discover was applied to analyze the crystalline structure. Scanning electron microscopy (SEM) was performed with a Zeiss Supra 55VP and field-emission transmission electron microscopy (TEM) with a Tecnai G2 F30 S-TWIN system to elucidate morphology. X-ray photoelectron spectroscopy (XPS) via an ESCALAB 250Xi was used to identify energy states of component elements. Thermogravimetric analysis (TGA) was tested by an SDT-2960 system in air condition from room temperature to 700 °C.

4.2.3 Cell assembly and electrochemical measurements

All electrochemical tests were carried out within CR2032 coin cells. For assembling symmetric cells, firstly, electrode slurries were prepared by manually mixing the active material, carbon black and carboxymethyl cellulose (CMC) with a mass ratio of 8: 1: 1 in a mortar, adding deionized water as solvent, before uniformly spreading on a copper foil and dried at 80 ºC under vacuum overnight. The electrodes were punched into discs (diameter 12 mm) with the average active material mass loading of 0.6 ~ 0.8 mg cm^{-2} and pressed under 10 MPa. The half-cell potassium-ion coin cells were assembled in an Argon-filled MBraun glove box (O_2 <0.1 ppm, H_2O <0.1 ppm) applying fresh K foil as counter electrodes and glass fiber filter as separators. The electrolyte was 5 M potassium trifluoromethanesulfonimide (KFSI) dissolved in ethylene carbonate (EC) and dimethyl carbonate (DMC) in a volumetric ratio 1: 1. For the electrochemical measurement, cyclic voltammetry (CV) at the scanning rate of 0.1 mV s^{-1} in a voltage window of 0.01 ~ 3 V, and electrochemical impedance spectroscopy (EIS) with an amplitude of 5 mV in the frequency range of 0.01 Hz to 100 kHz was performed on a Bio-Logic VMP3 workstation.

All galvanostatic tests, including cyclic and rate performance at various current densities between 0.01 and 3 V, were accomplished on Neware battery testers.

4.3 Results and Discussion

4.3.1 Synthesis and characterizations

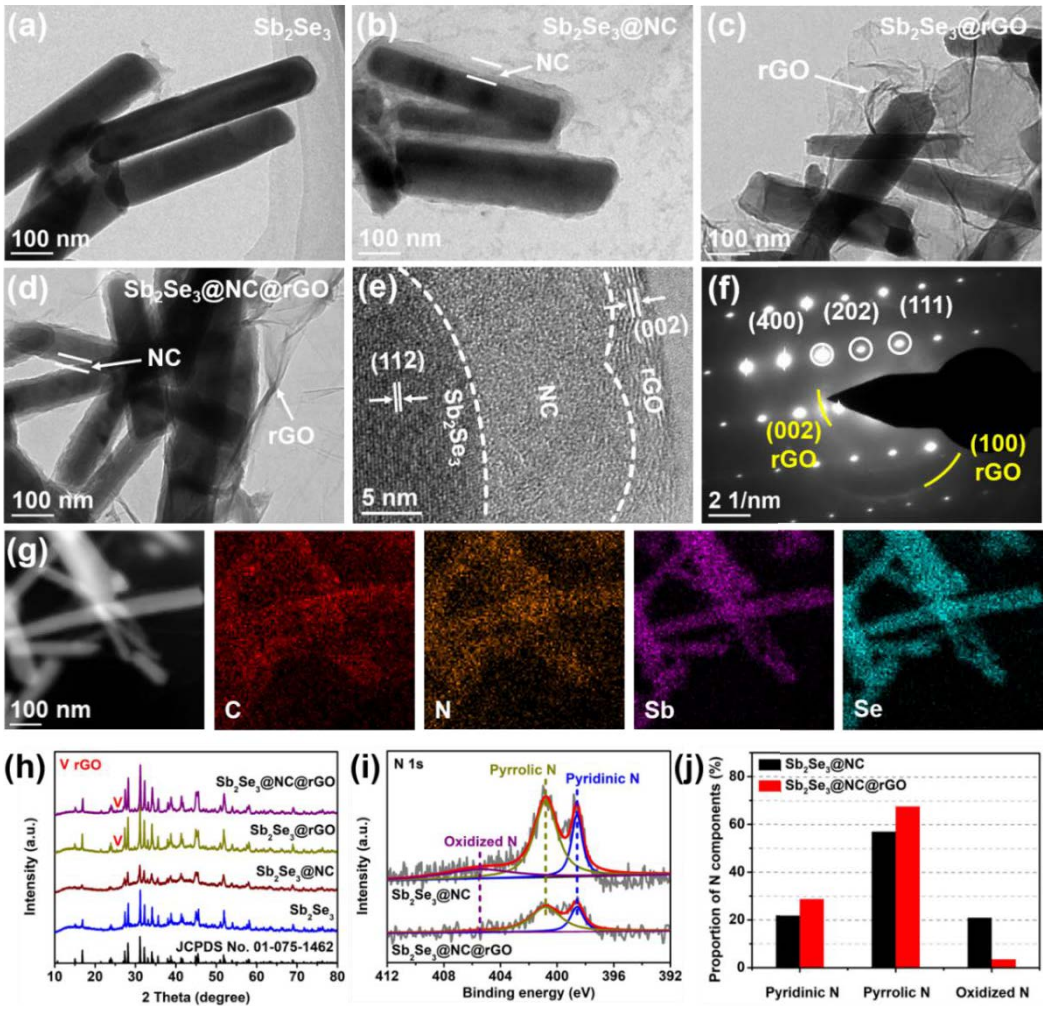

Figure 4.2 Synthesis and characterization of electrode materials. TEM images of (a) bare Sb_2Se_3 nanorods, (b) Sb_2Se_3@NC, (c) Sb_2Se_3@rGO, and (d) Sb_2Se_3@NC@rGO. (e) HRTEM image of Sb_2Se_3@NC@rGO. (f) SAED pattern of Sb_2Se_3@NC@rGO, where white facets correspond to the Sb_2Se_3 phase, and yellow facets are related with rGO. (g) HAADF-STEM and elemental mapping images for Sb_2Se_3@NC@rGO. (h) XRD patterns of bare Sb_2Se_3 nanorods, Sb_2Se_3@NC, Sb_2Se_3@rGO, and Sb_2Se_3@NC@rGO with

standard patterns of Sb_2Se_3 (JCPDS no. 01-075-1462). (i) High-resolution N 1s XPS spectra of Sb_2Se_3@NC and Sb_2Se_3@NC@rGO. (j) Proportion of nitrogen components in pyridinic, pyrrolic and oxidized N calculated by N 1s XPS spectra of Sb_2Se_3@NC and Sb_2Se_3@NC@rGO.

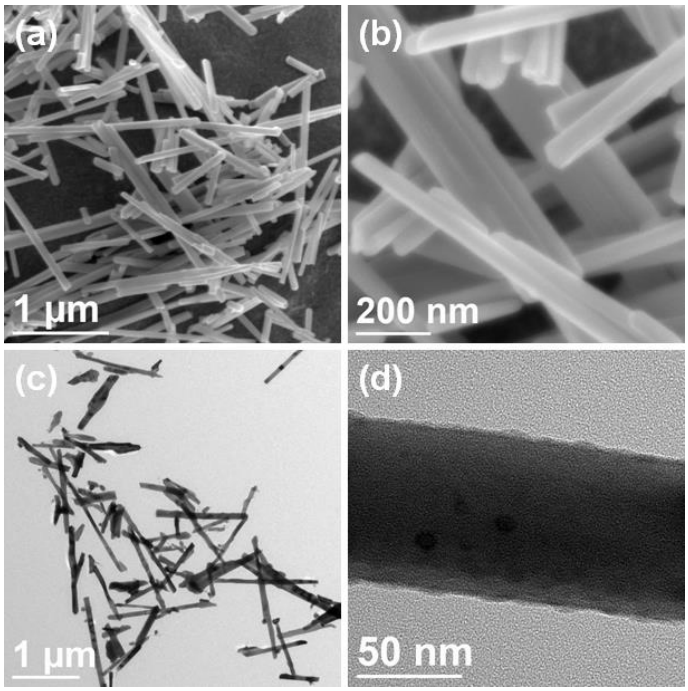

Figure 4.3 (a, b) SEM images and (c, d) TEM images of pure Sb_2Se_3 nanorods.

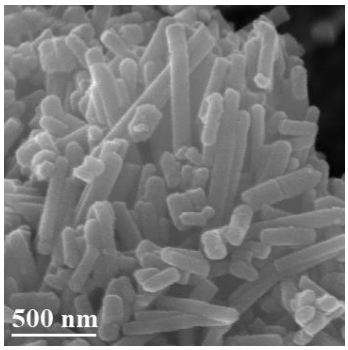

Figure 4.4 SEM images of Sb_2Se_3@NC.

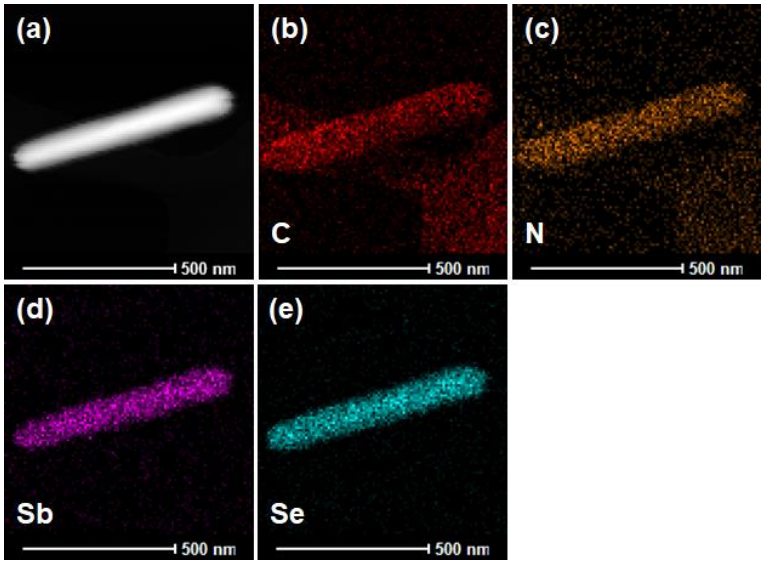

Figure 4.5 (a) HADDF-STEM image and (b-e) elemental mapping images of Sb_2Se_3@NC.

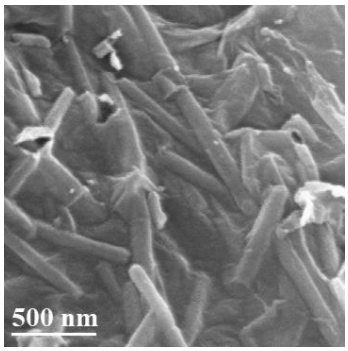

Figure 4.6 SEM images of Sb_2Se_3@rGO.

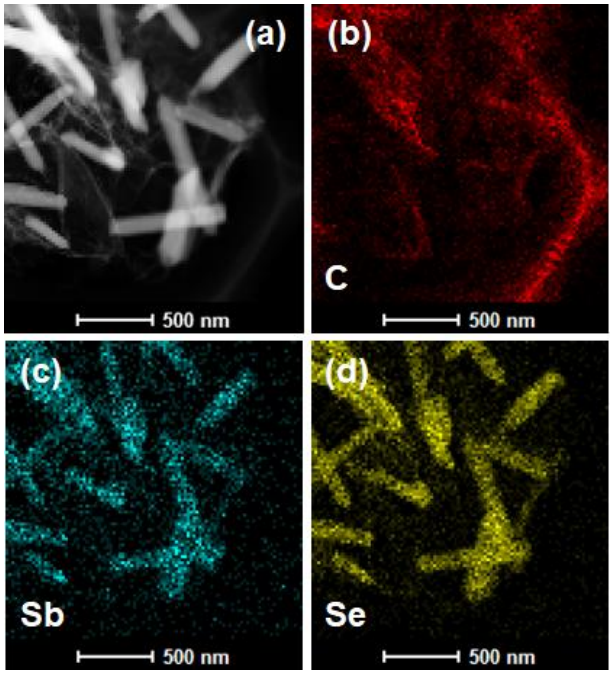

Figure 4.7 (a) HADDF-STEM image and (b-d) elemental mapping images of Sb_2Se_3@rGO.

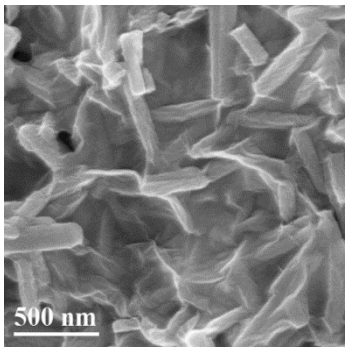

Figure 4.8 SEM images of Sb_2Se_3@NC@rGO.

Bare Sb_2Se_3 nanorods were prepared via a typical solvothermal method.[256] Homogeneous nanorods with a uniform width of ~80 nm and an average length of ~1 μm were obtained, as shown in **Figure 4.2a** and **Figure 4.3**. The NC-encapsulated Sb_2Se_3 nanorod composite (Sb_2Se_3@NC) was prepared by an *in-situ* polymerization and a post-calcination treatment. In the first step, the surfaces of Sb_2Se_3 nanorods were first coated by a uniform polydopamine layer via *in-situ* polymerization of dopamine precursors. Then, upon a post-calcination process in the Ar atmosphere, the polydopamine was

carbonized, forming an N-doped carbon layer on the surfaces of Sb_2Se_3 nanorods. Compared with bare Sb_2Se_3 nanorods, a coating layer of amorphous N-doped carbon with an average thickness of ~15 nm was observed on Sb_2Se_3 nanorods (**Figure 4.2b** and **Figure 4.4**). High-angle annular dark-field scanning transmission electron microscope (HADDF-STEM) and elemental mapping images (**Figure 4.5**) further demonstrate the uniform coating of N-doped carbon onto the Sb_2Se_3 nanorods. The rGO-confined Sb_2Se_3 nanorod composite (Sb_2Se_3@rGO) was synthesized via a solution-phase assembly process of Sb_2Se_3 nanorods and GO nanosheets, followed by a calcination treatment in the Ar atmosphere. Well-distributed Sb_2Se_3 nanorods were confined between ultrathin rGO nanosheets, as shown in **Figure 4.2c** and **Figures 4.6** and **4.7**. The Sb_2Se_3@NC@rGO composite was merely synthesized by freeze-drying solution-phase assembled polydopamine-coated Sb_2Se_3 nanorods and GO nanosheets, and a post-calcination treatment in Ar atmosphere. As shown in **Figure 4.2d** and **Figure 4.8**, both the N-doped carbon coating layer and rGO nanosheets were observed for the Sb_2Se_3@NC@rGO composites. HRTEM image (**Figure 4.2e**) further revealed a triple-layered structure of Sb_2Se_3@NC@rGO composites. The Sb_2Se_3 nanorods were directly encapsulated by a uniform layer of amorphous NC, and few-layered rGO nanosheets tightly covered the NC layers, which act as a flexible outer shell. The selected area electron diffraction (SAED) pattern in **Figure 4.2f** illustrated the high crystallinity of Sb_2Se_3 nanorods in Sb_2Se_3@NC@rGO composites. HAADF-STEM and elemental mapping images in **Figure 4.2g** also confirmed the hierarchical triple-layered architecture. Besides, the distribution of nitrogen is close to the carbon locations rather than antimony or selenium, which indicates the nitrogen doping in both carbon layers and rGO nanosheets.

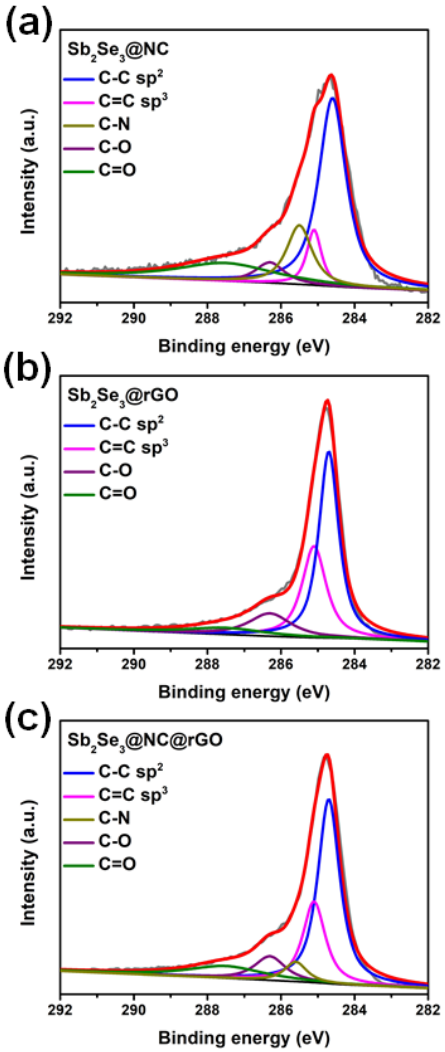

Figure 4.9 High-resolution C 1s XPS spectra of (a) Sb_2Se_3@NC, (b) Sb_2Se_3@rGO, and (c) Sb_2Se_3@NC@rGO.

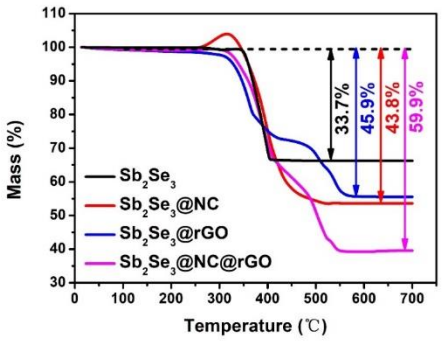

Figure 4.10 TGA results of Sb_2Se_3, Sb_2Se_3@NC, Sb_2Se_3@rGO, and Sb_2Se_3@NC@rGO.

Figure 4.2h shows XRD patterns of Sb_2Se_3, Sb_2Se_3@NC, Sb_2Se_3@rGO, and Sb_2Se_3@NC@rGO. All XRD patterns match the Sb_2Se_3 phase (*Pnma*, JCPDS No. 01-075-1462), confirming the good crystallinity of Sb_2Se_3 nanorods. A small peak at 25.4° was observed in the XRD patterns of Sb_2Se_3@rGO and Sb_2Se_3@NC@rGO, corresponding to the (0 0 2) planes of rGO nanosheets.[256] **Figure 4.2i** compares the high-resolution N 1s XPS spectra of Sb_2Se_3@NC and Sb_2Se_3@NC@rGO, which can be fitted to three types of nitrogen, in terms of, pyridinic N (398.6 eV), pyrrolic N (400.8 eV) and oxidized N (405.5 eV).[257] **Figure 4.2j** shows the proportions of nitrogen components in the three types of nitrogen in the Sb_2Se_3@NC and Sb_2Se_3@NC@rGO composites. With the introduction of rGO nanosheets, the percentage of oxidized N component dramatically decreases (by 17.5 %); whereas the amount of both pyridinic N and pyrrolic N increase by 7.9 % and 10.6 %, respectively, suggesting the conversion of oxidized N to pyridinic and pyrrolic N. This further gives the evidence that rGO nanosheets are doped by nitrogen derived from close contact with nitrogen-rich polydopamine. Furthermore, in the high-resolution C 1s spectra (**Figure 4.9**) of Sb_2Se_3@NC and Sb_2Se_3@NC@rGO, the C−N bond with a binding energy of 285.7 eV can be distinguished, in addition to the C−C sp^2 and C=C sp^3 bonds.[253] These results imply the intimate interaction between rGO and NC through a possible C−N bonding. The percentage of carbon materials (N-doped carbon and graphene nanosheets) in composites was determined to be ~10.1, 12.2 and 26.2 wt.% for Sb_2Se_3@NC, Sb_2Se_3@rGO, and Sb_2Se_3@NC@rGO, respectively, by thermogravimetric analysis (TGA) (**Figure 4.10**). The Sb_2Se_3, Sb_2Se_3@NC, Sb_2Se_3@rGO, and Sb_2Se_3@NC@rGO composites were tested from room temperature to 700 °C under air condition. The weight losses of composites are mainly attributed to the combustion of carbon components and the oxidation of Sb_2Se_3 into solid Sb_2O_4 and

evaporated SeO_2.[1] The carbon contents in all Sb_2Se_3 based composites are calculated by the following equation:[2]

$$\text{The weight loss percentage}=\frac{[M(Sb_2Se_3,480.4)-M(Sb_2O_4,307.5)]}{M(Sb_2Se_3,480.4)} \quad (1)$$

As a result, the carbon contents of the Sb_2Se_3@NC, Sb_2Se_3@rGO, and Sb_2Se_3@NC@rGO composites are ~10.1, 12.2, and 26.2 wt.%.

4.3.2 Electrochemical performance

The performances of the as-prepared bare Sb_2Se_3, Sb_2Se_3@NC, Sb_2Se_3@rGO, and Sb_2Se_3@NC@rGO anode materials were tested using a metallic potassium flake as counter electrode and 5M KFSI in EC: DMC= 1: 1 electrolyte in CR2032 coin cells. Concentrated KFSI based electrolytes have been proven to promote the rate performance and especially cycling stability of anode materials in PIBs.[258,259] **Figure 4.11a** shows galvanostatic charge-discharge (GCD) curves of Sb_2Se_3@NC@rGO at a current density of 50 mA g^{-1}. In the first cathodic cycle, two discharge plateaus at around 1.2 and 0.8 V were observed and could be corresponded to a two-step conversion reaction.[260-262] A plateau at 0.2 V was associated with the alloying reaction between Sb and K^+.[263,264] From the second cycle, one of the conversion plateaus increased to about 1.5 V, due to the activation of Sb_2Se_3.[247] During the first anodic scan, three plateaus at about 0.6, 1.4 and 2.3 V were observed and could be assigned to the de-alloying and reversed conversion reactions. The GCD curves of Sb_2Se_3@NC@rGO electrodes closely overlapped during the first 10 cycles, and there was almost no shift in plateaus, indicating a negligible polarization. A large reversible capacity of ~580 mA h g^{-1} was obtained for the Sb_2Se_3@NC@rGO at the end of the 10^{th} cycle. The potential over 0.8 V contributed more than half of the discharging capacities for the Sb_2Se_3@NC@rGO electrode, which may cause a relatively low gravimetric energy density. However, the high density (5.8 g cm^{-3})

[265] of Sb_2Se_3 results in a practical volumetric specific capacity of about 2025 mA h cm^{-3}. This value is much higher than those of some reported anodes,[266,267] suggesting a large volumetric energy density. **Figure 4.12** shows the GCD curves of Sb_2Se_3@rGO, Sb_2Se_3@NC, and Sb_2Se_3 within the first 10 cycles. For the Sb_2Se_3@rGO electrode, the discharge plateaus started to shift to lower voltages, whereas the charge curves shifted to higher voltages from the 5th cycle. A similar trend occurred in the Sb_2Se_3@NC electrode from the 3rd cycle and was even worse for Sb_2Se_3 from the 2nd cycle. Reversible capacity of ~85, 140, 295 mA h g^{-1} were obtained for the Sb_2Se_3, Sb_2Se_3@NC and Sb_2Se_3@rGO electrodes at the end of the 10th cycle, respectively, much smaller than that of the Sb_2Se_3@NC@rGO electrode.

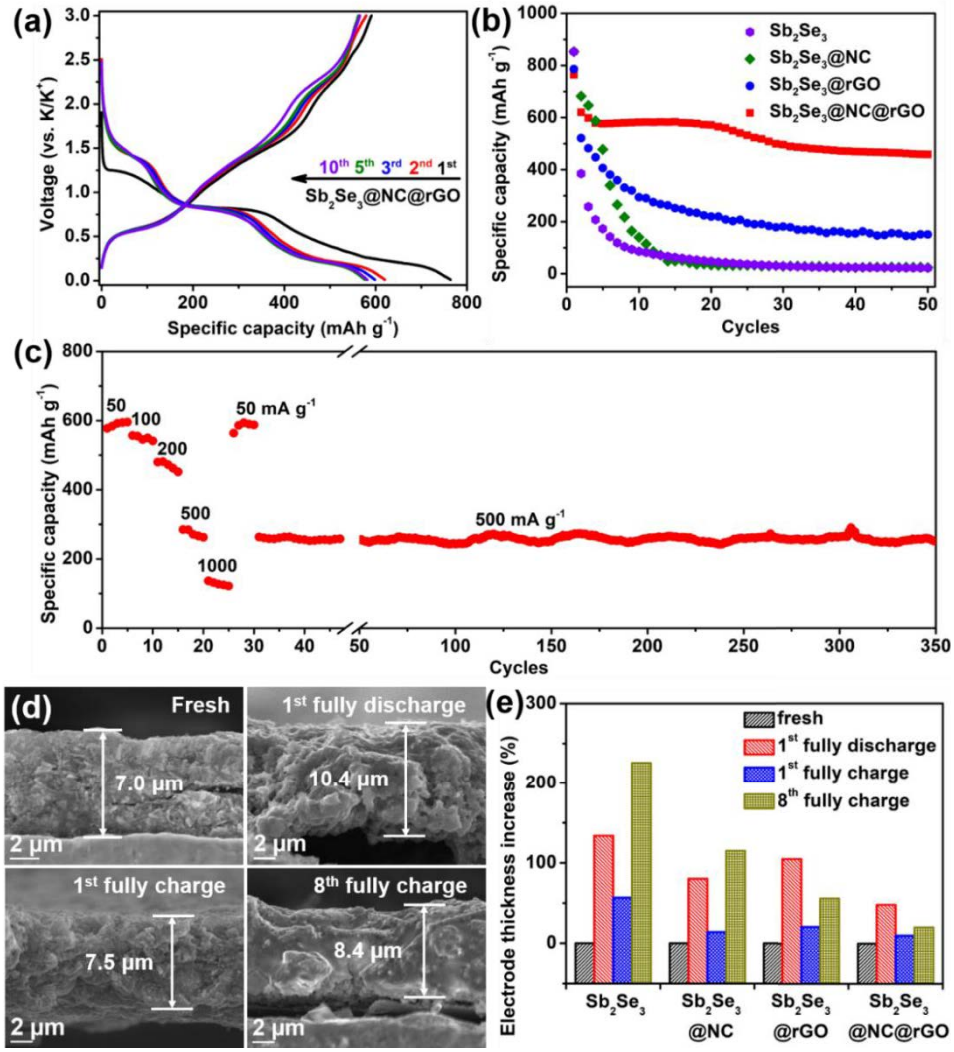

Figure 4.11 Electrochemical performance and electrode thickness change before and after charge/discharge cycles. (a) GCD curves of the Sb_2Se_3@NC@rGO electrode for the 1st, 2nd, 3rd, 5th, and 10th cycles. (b) Cycling performance of the Sb_2Se_3, Sb_2Se_3@NC, Sb_2Se_3@rGO, and Sb_2Se_3@NC@rGO electrodes at a current density of 50 mA g^{-1}. (g) Rate and long-term cycling performances of the Sb_2Se_3@NC@rGO electrode. (d) The cross-section SEM images of the fresh and charged/discharged Sb_2Se_3@NC@rGO electrodes. (d) Electrode thickness increases of the Sb_2Se_3, Sb_2Se_3@NC, Sb_2Se_3@rGO, and Sb_2Se_3@NC@rGO electrodes during the charge and discharge cycles.

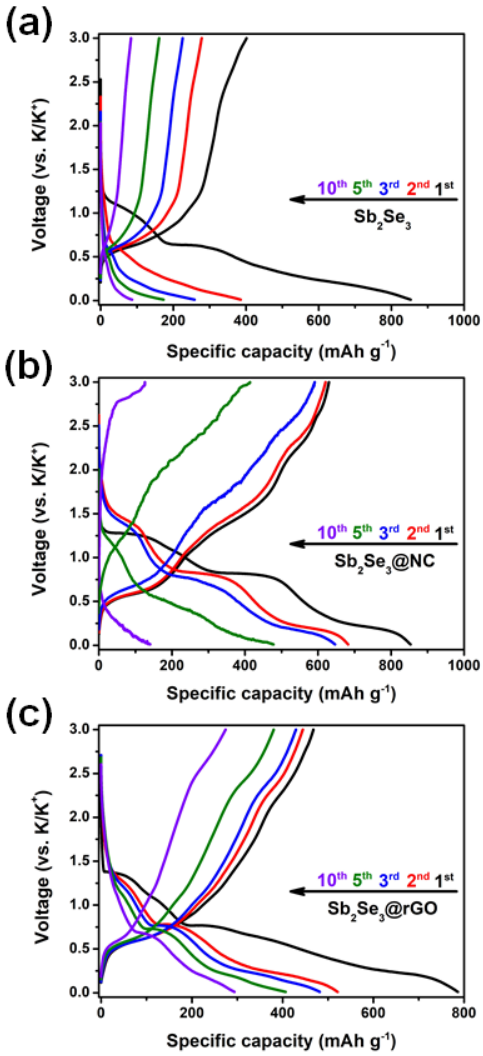

Figure 4.12 GCD curves of (a) Sb_2Se_3, (b) Sb_2Se_3@NC, and (c) Sb_2Se_3@rGO at a current density of 50 mA g^{-1} for the 1st, 2nd, 3rd, 5th and 10th cycles.

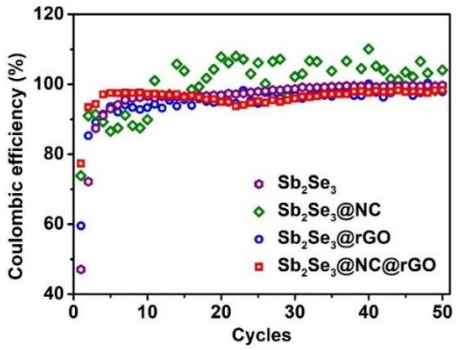

Figure 4.13 Coulombic efficiency of Sb_2Se_3, Sb_2Se_3@NC, and Sb_2Se_3@rGO during the cycling test at a current density of 50 mA g^{-1}.

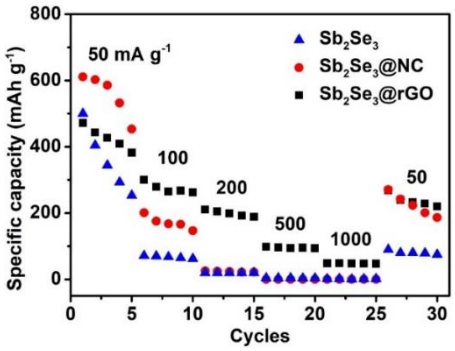

Figure 4.14 Rate performance of Sb_2Se_3, Sb_2Se_3@NC, and Sb_2Se_3@rGO tested at various current densities from 50 to 1000 mA g^{-1}.

Figure 4.11b compares the cycling performance of all-studied anodes. The Sb_2Se_3@NC@rGO anode delivered a discharge and charge specific capacity of ~765 and 590 mA h g^{-1}, respectively, resulting in a high initial Coulombic efficiency of 77.3 %. In contrast, the Sb_2Se_3, Sb_2Se_3@NC and Sb_2Se_3@rGO electrodes showed lower initial Coulombic efficiencies of 47.1 %, 73.8 % and 59.5 %, respectively (**Figure 4.13**). After several initial cycles, the specific capacities of the bare Sb_2Se_3, Sb_2Se_3@NC, and Sb_2Se_3@rGO electrodes remarkably faded. Particularly, the bare Sb_2Se_3 and Sb_2Se_3@NC electrodes almost failed after 10 cycles, while the Sb_2Se_3@NC@rGO electrode remained stable without capacity fading for over 20 cycles. Eventually, the Sb_2Se_3@NC@rGO electrodes maintained a high capacity retention ratio of 76.2 % for 50 cycles with a corresponding reversible specific capacity of ~450 mA h g^{-1}. The Sb_2Se_3@NC@rGO electrode was further cycled at various current densities (**Figure 4.11c**). Compared with the other three electrodes (**Figure 4.14**), the Sb_2Se_3@NC@rGO anodes showed the best rate properties with reversible capacities of ~595, 545, 475, 270 and 130 mA h g^{-1} at various current densities of 50, 100, 200, 500 and 1000 mA g^{-1}, respectively. Upon a continuous long-term cycling test at a current density of 500 mA g^{-1}, the Sb_2Se_3@NC@rGO still maintained a high reversible capacity of 250 mA h g^{-1} over 350 cycles.

Ex-situ SEM characterizations were performed to investigate the structural stability of all anodes before and after cycling. All anodes with a similar mass loading (~1.0 mg cm^{-2}) of active materials were cycled under a current density of 50 mA g^{-1}. **Figure 4.11d** shows the cross-sectional SEM images of Sb_2Se_3@NC@rGO electrodes in fresh, after the 1st discharge, after the 1st charge, and after the 8th charge cycles, respectively. Those for Sb_2Se_3, Sb_2Se_3@NC, and Sb_2Se_3@rGO electrodes are shown in **Figure 4.15**. The increases of electrode thickness were shown in **Figure 4.11e**. During the 1st discharge process (K^+ ions insertion), all Sb_2Se_3-based anodes showed an apparent increase of the thickness. The thickness of the Sb_2Se_3, Sb_2Se_3@NC, Sb_2Se_3@rGO and Sb_2Se_3@NC@rGO electrodes increased by 133.8 %, 80.3 %, 105.8 % and 48.6 %, respectively. After the 1st charge (K^+ ions extraction), the thickness of the Sb_2Se_3@NC, Sb_2Se_3@rGO, and Sb_2Se_3@NC@rGO electrodes reverses back the values close to the original state, except for the Sb_2Se_3 electrode. The Sb_2Se_3@NC@rGO electrode retained a low thickness expansion (~10 %) within 8 cycles, while the thickness of the Sb_2Se_3@NC and Sb_2Se_3@rGO electrodes were ~2.2 and ~1.5 times thicker than that of the fresh samples. The top-view SEM images were presented to directly illustrate the morphology changes of electrodes (**Figure 4.16**). The Sb_2Se_3 nanorods in the cycled Sb_2Se_3, Sb_2Se_3@NC, and Sb_2Se_3@rGO electrodes were entirely broken and aggregated. Only the Sb_2Se_3@NC@rGO electrode retained the long nanorod-like architecture. These strongly confirmed the combined advantages of encapsulation of NC coating and 2D confinement of rGO nanosheets for retaining the electrode integrity of Sb_2Se_3 nanorods.

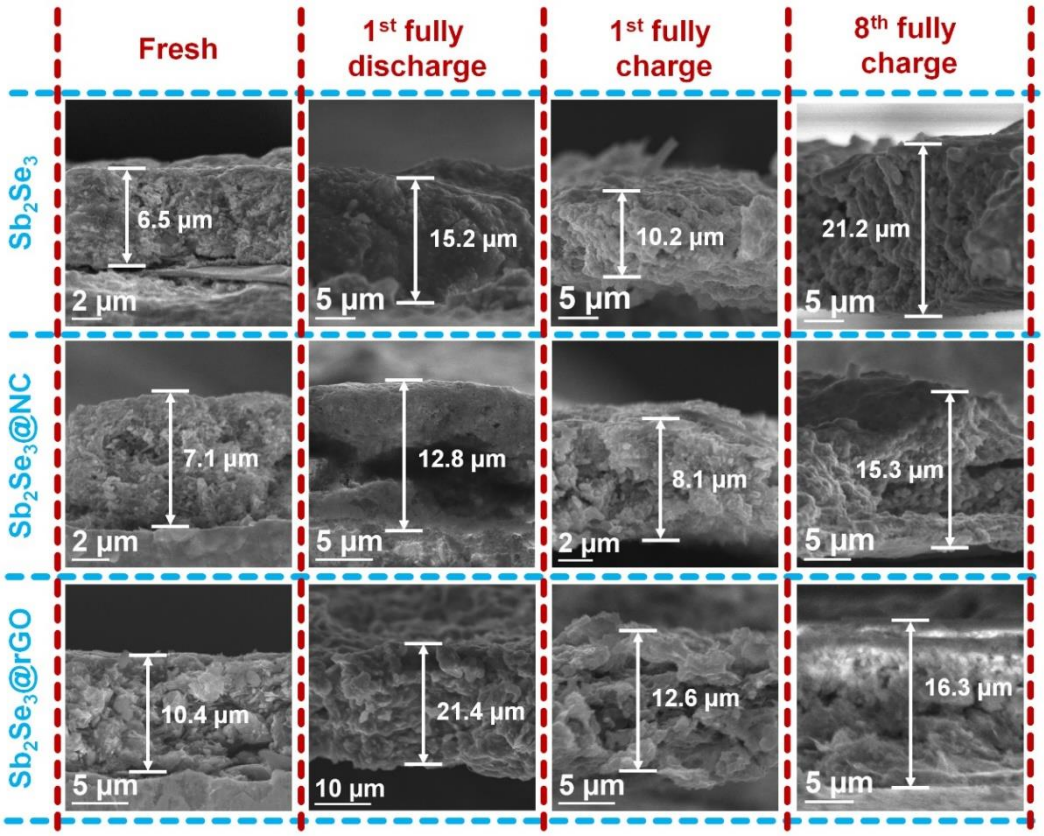

Figure 4.15 Cross-section SEM images of Sb_2Se_3, Sb_2Se_3@NC, and Sb_2Se_3@rGO anodes before cycling, after the 1st fully discharge, the 1st fully charge, and the 8th fully charge.

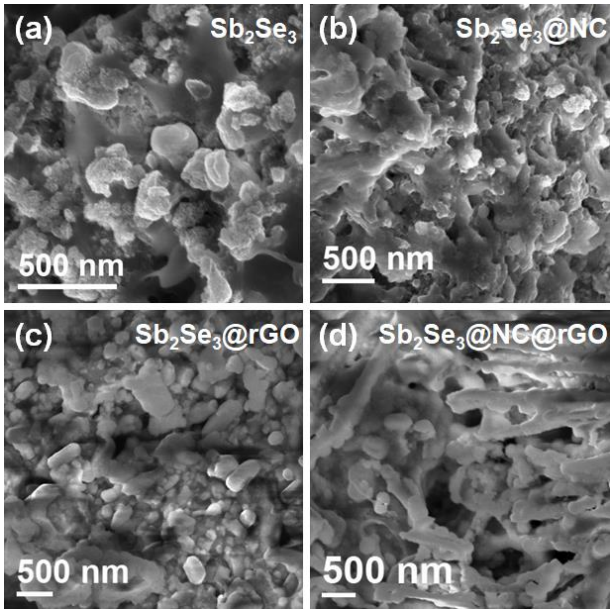

Figure 4.16 SEM images of Sb_2Se_3, Sb_2Se_3@NC, Sb_2Se_3@rGO, and Sb_2Se_3@NC@rGO electrodes after 8 cycles.

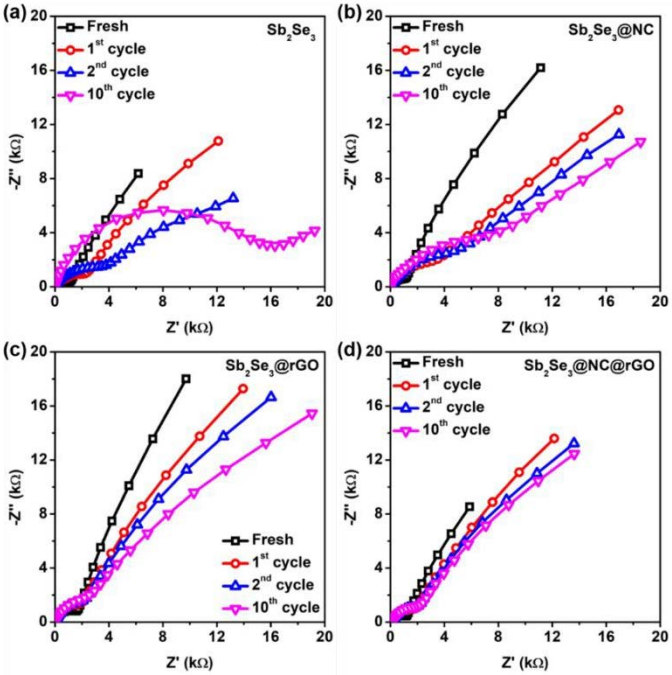

Figure 4.17 EIS of the (a) Sb_2Se_3, (b) Sb_2Se_3@NC, (c) Sb_2Se_3@rGO, and (d) Sb_2Se_3@NC@rGO electrodes.

Electrochemical impedance spectroscopy (EIS) was measured to examine the structural stability of the Sb_2Se_3, Sb_2Se_3@NC, Sb_2Se_3@rGO, and Sb_2Se_3@NC@rGO

electrodes after different cycles (**Figure 4.17**). All the EIS curves show a depressed semicircle in the high-frequency range with a similar size for the fresh electrodes, which corresponds to the charge-transfer resistance of the electrode/electrolyte interfaces.[268] After the initial potassiation process, the radii of all semicircles increased due to the formation of SEI. The increase of semicircles was apparent for the Sb_2Se_3 and Sb_2Se_3@NC electrodes from the 2nd cycle, corresponding to the continuous growth of SEI films. It could be caused by the pulverization of anode materials.[269,270] After 10 cycles, the semicircle of the Sb_2Se_3@NC electrodes was smaller than that of the Sb_2Se_3 electrodes, because of the relatively better volumetric restriction benefited from NC coating. Particularly, the Sb_2Se_3@rGO and Sb_2Se_3@NC@rGO electrodes maintained a small and stable radius of the semicircle over 10 cycles, demonstrating the good stability of formed SEI film. This clearly proved that the combination of NC coating encapsulation and rGO nanosheet confinement could effectively prevent the pulverization of Sb_2Se_3 nanorods.

4.3.3 Potassium-ion storage mechanism

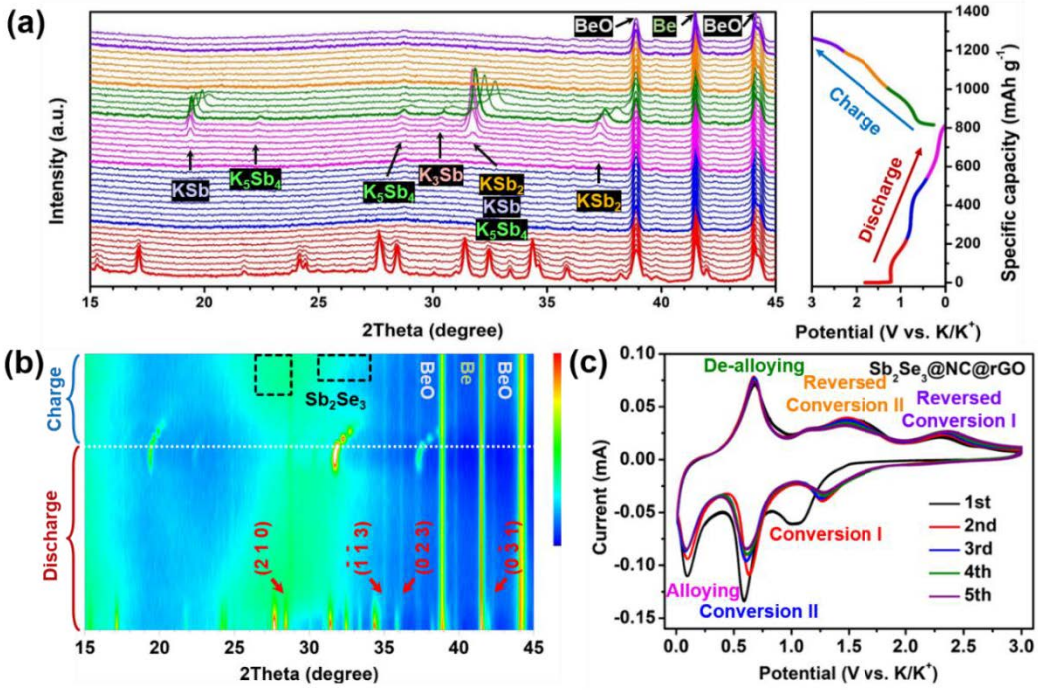

Figure 4.18 Analysis of potassium storage mechanism of Sb_2Se_3@NC@rGO. (a, b) *In-situ* XRD patterns of the Sb_2Se_3@NC@rGO electrode with a corresponding GCD curve. The black frames and red facets in (b) correspond to the Sb_2Se_3 and KSb_2Se_4 phases, respectively. (c) CV curves of Sb_2Se_3@NC@rGO during the initial five cycles.

The stable potassium storage mechanism of Sb_2Se_3@NC@rGO was verified by *in-situ* XRD techniques. **Figures 4.18a** and **b** show the XRD patterns measured from 15° to 45° and the corresponding GCD curves. Upon the insertion of K^+ ions, the intensity of all peaks of Sb_2Se_3 phase gradually decreased and disappeared; meanwhile, several new peaks at 28.7°, 35.0°, 36.2°, and 42.3° were observed, corresponding to the (2 1 0), ($\bar{1}$ $\bar{1}$ 3), (0 2 3) and (0 $\bar{3}$ 1) facets of a KSb_2Se_4 phase (JCPDS no. 04-010-2313). During the discharge process between 0.8 and 0.4 V, few obvious peaks related to Sb and K_2Se were detected. During the further discharge process, a series of K_xSb alloys were formed. The first detected K_xSb alloy is KSb_2 (JCPDS no. 04-007-2281) with a weak signal at 37.3°

and then a stronger signal at 31.8°. At the same time, a diffraction peak corresponding to a KSb phase (JCPDS no. 00-042-0791) was detected at 19.4°. As the reaction proceeded, more K^+ ions reacted with the K_xSb alloy to form K-rich K_xSb alloys such as K_5Sb_4 (JCPDS no. 04-010-4048), which showed diffraction peaks at 22.6° and 28.7°. At the end of the discharge process to 0.01 V, a diffraction peak at 30.3° was observed, attributing to the formation of the final product of K_3Sb (JCPDS no. 00-019-0935). The above observations suggest a multi-step alloying reaction from K-deficient K_xSb alloys to K-rich K_xSb alloys (**Figure 4.19**).[228,229,271] During the charge process, all peaks associated with K_xSb alloys shifted to higher angles and eventually vanished. No sharp characteristic peaks related to the primary Sb_2Se_3 phase were detected. Instead, broad peaks in the range 27° ~ 29° and 31° ~ 34° were observed. These suggest that the initial Sb_2Se_3 crystals were converted into amorphous species or species with a low crystallinity after the extraction of K^+ ions. The standard XRD patterns of all mentioned compounds, including beryllium (Be, at 41.5°) and beryllium oxide (BeO, at 38.9° and 44.2°) backgrounds from the XRD transmission window in the *in-situ* cell, are shown in **Figure 4.20**. In addition to the Sb_2Se_3, a reversible change of a broad peak of rGO nanosheets between 23° and 29° was also observed. This may suggest that the rGO nanosheets could restrain the large volume changes of Sb_2Se_3 during the potassiation process via changing their interlayer spaces. Upon insertion of K^+ ions (discharge process), an expansion force perpendicular to the rGO layers originated from the large volume expansion of Sb_2Se_3 dramatically presses the rGO layers, leading to a reduced interlayer spacing, as shown in the revised **Figure 4.21**.

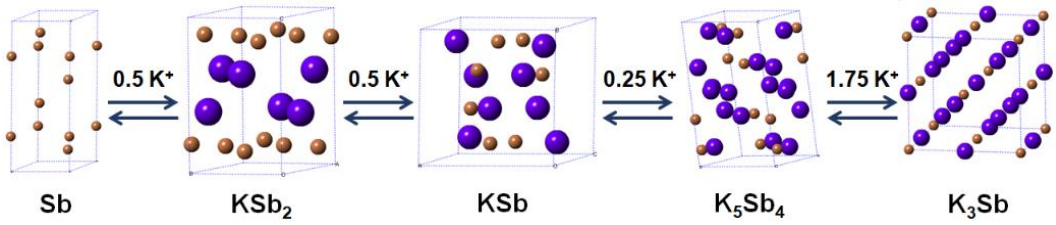

Figure 4.19 Schematic illustration of multi-step alloying reaction from Sb to K_3Sb during the discharge process and reversely multi-step dealloying reaction during the charge process. Brown and violet balls represent Sb and K atoms, respectively.

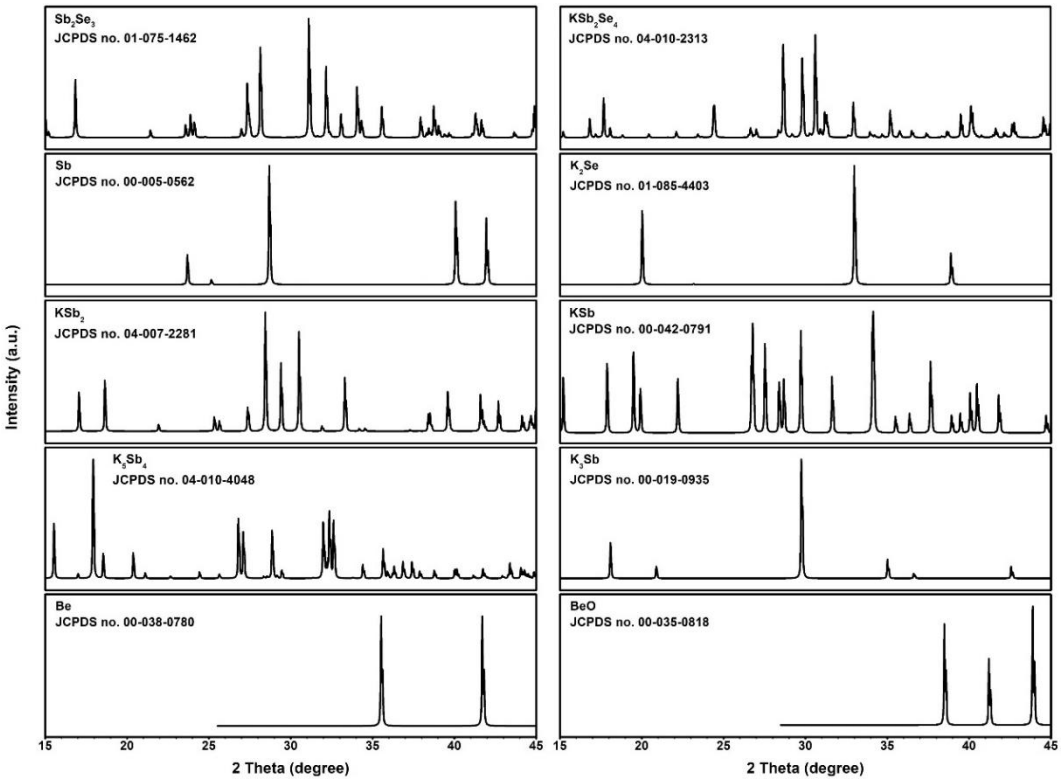

Figure 4.20 Standard XRD patterns associated with all compounds appeared at the *in-situ* XRD test, including background (Be and BeO), original compound (Sb_2Se_3), intercalation product (KSb_2Se_4), conversion products (Sb and K_2Se), and alloying production (KSb_2, KSb, K_5Sb_4, and K_3Sb).

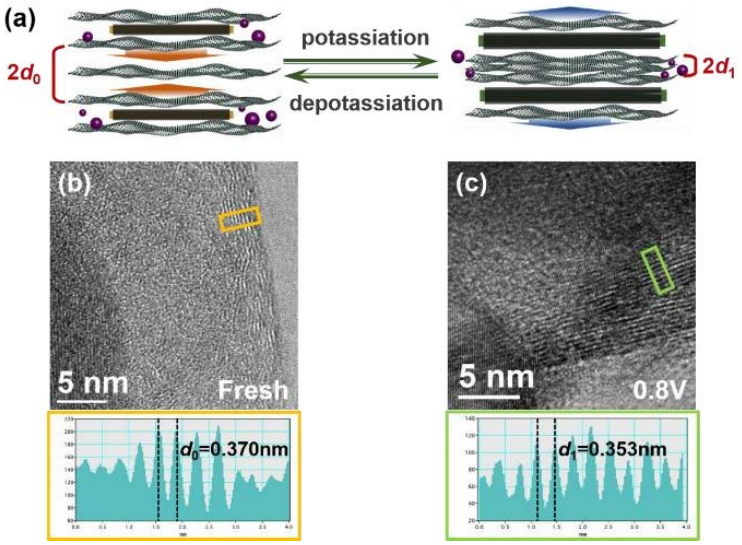

Figure 4.21 (a) Schematic illustration of the functional mechanism that rGO nanosheets restrain the volume expansion via changing interlayer spacings during K^+ ion intercalation and deintercalation. The *ex-situ* TEM images of the Sb_2Se_3@NC@rGO electrode (b) before cycle and (c) discharged to 0.8 V.

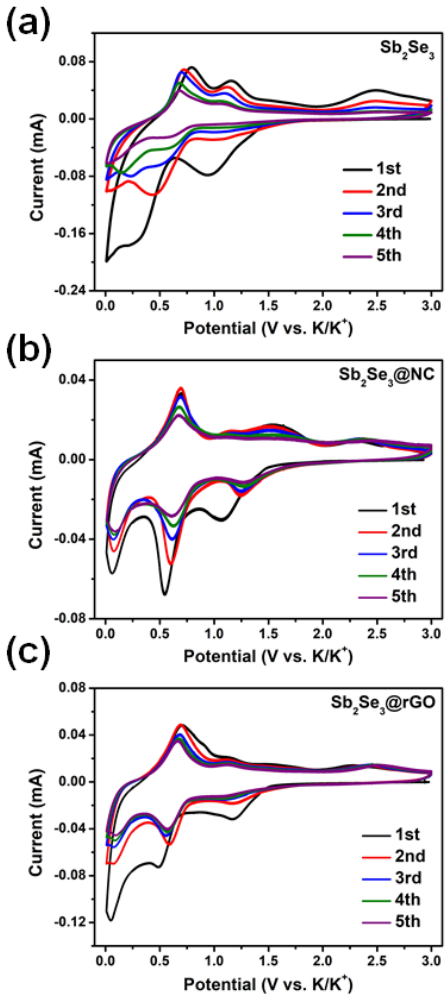

Figure 4.22 CV curves of (a) Sb_2Se_3, (b) Sb_2Se_3@NC, and (c) Sb_2Se_3@rGO at 0.1 mV s^{-1} during the initial five cycles.

Figure 4.18c shows the cyclic voltammograms (CVs) curves of the Sb_2Se_3@NC@rGO electrode during the initial five scans. A reduction peak at about 1.0 V could be described to the conversion reaction of forming the KSb_2Se_4 and Sb phase (conversion I). The second reduction peak at 0.6 V was associated with the further conversion reaction between K^+ and KSb_2Se_4, along with the formation of Sb embedded in K_2Se (conversion II). The last peak at 0.1 V was ascribed to the multi-step alloying reactions from metallic Sb to K_3Sb alloys. Besides, this reduction peak also included contributions from the intercalation of K^+ ions into carbon-based species. During the first anodic scan, a sharp oxidation peak at 0.7 V indicated the multi-step de-alloying reactions from K_3Sb to Sb.

Two broad oxidation peaks located at around 1.1 and 1.5 V signified a reversed conversion II reaction of Sb and K_2Se into KSb_2Se_4. The last broad oxidation peak at about 2.3 V was attributed to a reversed conversion I reaction of formation of Sb_2Se_3 from Sb and KSb_2Se_4. From the second scan, all redox peaks were overlapped, illustrating the good reversibility of the potassiation/depotassiation processes in the Sb_2Se_3@NC@rGO anode. The CV analysis of the Sb_2Se_3, Sb_2Se_3@NC, and Sb_2Se_3@rGO electrodes were also performed (**Figure 4.22**). Although, similar redox peaks to those of the Sb_2Se_3@NC@rGO were observed, the intensities of all redox peaks gradually decreased within five cycles, suggesting a large pulverization and a low structural stability. Based on the above results, the potassium-ion storage mechanism for the Sb_2Se_3@NC@rGO is proposed as below, which includes two-step conversion reactions and a multi-step alloying process:

Conversion I reaction:

$$4Sb_2Se_3 + 3K^+ + 3e^- \rightarrow 3KSb_2Se_4 + 2Sb \quad (1)$$

Conversion II reaction:

$$KSb_2Se_4 + 7K^+ + 7e^- \rightarrow 4K_2Se + 2Sb \quad (2)$$

Multi-step alloying reactions:

$$Sb + xK^+ + xe^- \rightarrow K_xSb_2 \ (x = 1, 2, 2.5 \text{ and } 6) \quad (3)$$

Multi-step de-alloying reactions:

$$K_xSb_2 \rightarrow Sb + xK^+ + xe^- \ (x = 1, 2, 2.5 \text{ and } 6) \quad (4)$$

Reversed conversion II reaction:

$$4K_2Se + 2Sb \rightarrow KSb_2Se_4 + 7K^+ + 7e^- \quad (5)$$

Reversed conversion I reaction:

$$3KSb_2Se_4 + 2Sb \rightarrow 4Sb_2Se_3 + 3K^+ + 3e^- \quad (6)$$

Figure 4.23 shows the *ex-situ* TEM observations of the Sb_2Se_3@NC@rGO electrode at different potentials within the first cycle. Low-resolution TEM images showed the well maintained nanorod-like morphology of Sb_2Se_3 during the whole charge/discharge processes. As shown in **Figure 4.23a**, products of both KSb_2Se_4 and Sb as expressed in Reaction 1 and K_2Se and Sb as expressed in Reaction 2 were observed when the Sb_2Se_3@NC@rGO electrode was discharged to 0.8 V. After further discharging to 0.01 V, both lattice fringes in HRTEM image and electron diffraction rings in the SAED patterns (**Figure 4.23b**) suggested a mixture of K−Sb alloys was formed, including KSb_2, KSb, K_5Sb_4 and K_3Sb, as expressed in Reaction 3. This confirmed the multi-step alloying reaction mechanisms of the Sb_2Se_3@NC@rGO electrode, in agreement with the *in-situ* XRD results. In **Figure 4.23c**, during the charge process to 1.5 V, a mixture of KSb_2Se_4, K_2Se, and Sb was formed, implying the completed de-alloying reaction of K−Sb alloys (Reaction 4) and the occurrence of the reversed conversion II reaction (Reaction 5). At a fully charged state of 3.0 V, the lattice fringes and SAED patterns (**Figure 4.23d**) can be indexed into Sb_2Se_3, as expressed by Reaction 6. All the above observations confirming the high reversibility of the Sb_2Se_3@NC@rGO anode for K^+ storage.

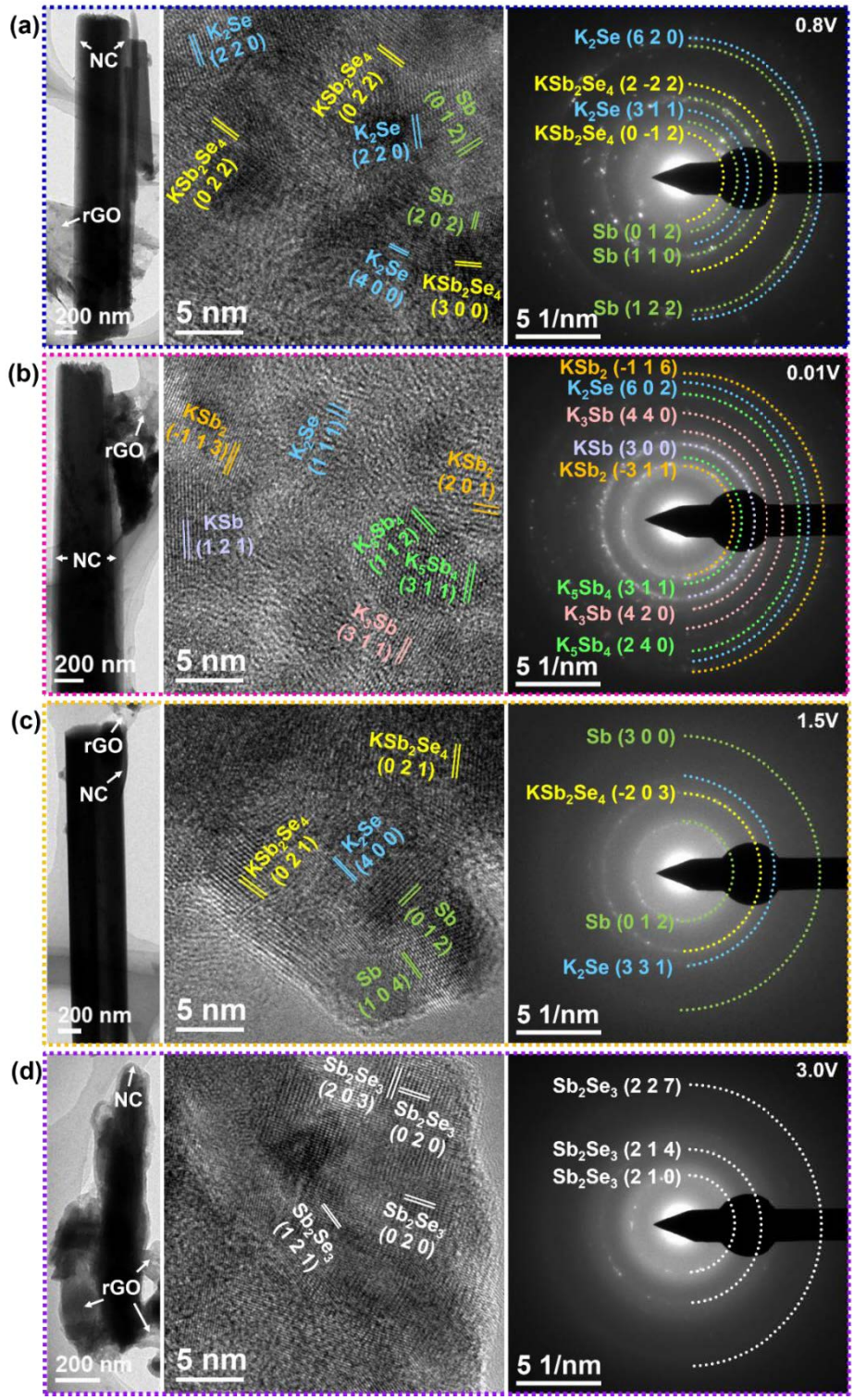

Figure 4.23 *Ex-situ* observations of the Sb_2Se_3@NC@rGO during the charge and discharge processes. *Ex-situ* TEM and HRTEM images with corresponding SAED patterns of Sb_2Se_3@NC@rGO electrodes (a) discharged to 0.8 V and (b) 0.01 V, and charged to (c) 1.5 V and (d) 3.0 V.

4.4 Conclusion

In summary, a Sb_2Se_3@NC@rGO composite was synthesized through the combination of conductive NC encapsulation and 2D rGO confinement. When applied as anodes for PIBs, the Sb_2Se_3@NC@rGO composite delivered a high reversible specific capacity of ~590 mA h g^{-1} at a current density of 50 mA g^{-1} and 250 mA h g^{-1} at a large current density of 500 mA g^{-1} for over 350 cycles. *In-situ* and *ex-situ* characterizations proved a well-maintained morphology and a high structural stability of the Sb_2Se_3@NC@rGO anode during a specific two-step conversion and multi-step alloying reaction mechanism. The synergistic effect between N-doped carbon coating and rGO nanosheets protective layers could contribute to the improvement of electrochemical performance. The NC coating layers help to protect Sb_2Se_3 nanorods from pulverization and flexible rGO nanosheets maintain the overall structural integrity. This work provided an efficient strategy to design high-performance conversion/alloying-based electrodes for advanced energy storage applications.

Chapter 5 2D-2D Heterostructures: Pre-Introduced Strain Enhancing Structural Stability of δ-MnO_2 in Aqueous Zinc-Ion Batteries

5.1 Introduction

In the past two decades, alkali-ion batteries, especially the most representative lithium-ion batteries, developed rapidly and realized industrialization, but they still suffer from severe flaws, like potentially risky organic electrolyte systems, strict requirements to assembly techniques and working environments, and high cost. Recently, the rejuvenated aqueous zinc-ion batteries have become competitive in large-scale energy storage and attracted many research interests, relying on their excellent safety, cost affordability, manufacturing feasibility, and environmental adaptability. The direct usage of metallic Zn anodes in aqueous electrolytes also brings very high volumetric capacity (5858 mAh m^{-3}) and capacity density (5855 mAh cm^{-2}) for zinc-ion batteries, over 2.8 times than those for lithium counterparts.[272] To achieve an excellent overall electrochemical performance, the selection of cathode materials appears to be particularly important. Manganese-based oxides with a typical representative of MnO_2 can be a most promising candidate due to the high theoretical capacity (~308 mAh g^{-1}) and average working potential (~1.35V vs. Zn/Zn^{2+}), thus exhibiting an overwhelming energy density than other competitors, including vanadium-based oxides, transition metal dichalcogenides, organic materials, and metal-organic frameworks.[273] However, the Mn dissolution and the subsequent structural degradation are the biggest challenges to the practical utilization of manganese-based oxides, especially for δ-phase MnO_2 possessing the largest planar channels.[274]

Typically, the optimization of electrolytes via the "common-ion effect" is a widespread solution to the Mn dissolution that the increase of soluble ionic compound can change the equilibrium reaction of ionic association/dissociation.[275] For Mn-based oxides, the most convenient method is the additive of Mn^{2+} coupling with appropriate anions in electrolytes, such as the introduction of $MnSO_4$ into $ZnSO_4$ electrolytes and $Mn(CF_3SO_3)_2$ into $Zn(CF_3SO_3)_2$ electrolytes.[276,277] Other cationic ions like Na^+ can also be applied to restrict the sodium-containing manganese oxides, for example, Birnessite-phase $Na_{0.55}Mn_2O_4 \cdot 1.5H_2O$.[278] However, introducing Mn^{2+} additive may complicate the Zn storage and MnO_2 conversion mechanism and bring in many side reactions on the other hand.[279,280] Surface coating is another accessible method, and the coating species often range from but are not limited to carbonaceous materials and Zn-affinity polymers (like polypyrrole, polyaniline, *etc.*).[102,281-283] Some inorganic candidates, for example, dense inorganic $CaSO_4 \cdot 2H_2O$ coating on Ca_2MnO_4 surface *in-situ* generated during the electrochemical deposition process, also effectively inhibit Mn dissolution without sacrificing ion diffusion.[284] Nevertheless, surface modification cannot entirely protect the materials from the penetration of water molecules. Transition metal dopants, especially Co and Ni with good compatibility with MnO_6 units, are able to work as "structural pillars" to stabilize the lattice from "Jahn-Teller" effects,[285,286] while their unexpected electrocatalytic properties may facilitate oxygen evolution reaction at high working potentials. Pre-intercalating alkali ions or organic molecules are usually employed to layered δ-MnO_2 for alleviating structural variation during cycling,[287-289] but actually, their electrostatic interactions with MnO_6 sheets are not strong enough to overcome the lattice distortion induced by "Jahn-Teller" effects, and meanwhile, they may be easy substituted by high-concentrated H^+ or Zn^{2+} ion within cycles.

Strain engineering is an emerged and promising strategy to solve the issues of electrodes in various alkali-ion batteries. In cathode materials, introducing strain at surface area via lattice mismatching of P2-OP4 phase transformation can suppress the crack generation and propagation of layered P2-type sodium layer oxide cathodes.[290] Otherwise, the activity and stability of lattice oxygen in lithium-rich layered oxides demonstrate high relevance with the feature of strains in terms of tensile or compressive strain originated from lattice expansion or shrinkage controlled by modifications.[291,292] Our group also found that coupling graphene with $VOPO_4$ to form a 2D multi-layered heterostructure can generate ~4.0% strain at the interface, which improved the diffusion of alkali ions and released the ion insertion induced stress.[118] In anode materials, the local strain is able to optimize electrochemical and kinetics behaviors.[293-295] For example, the tuneable *c*-axis strains in V_2O_5 continuously modulated Li intercalation potentials as well as the diffusion coefficients.[294] Moreover, the interface strain among carbon and MoS_2 nanosheets can even catalyze MoS_2 conversing into Mo and Li_2S_n species, different from the conventional Li intercalation mechanism for MoS_2.[295] Besides, in lithium metal anodes, the distinct lattice distortion triggered mechanical strains in high-entropy MXene regulated the lithium nucleation and growth homogeneously.[296] However, no report mentioned the strain engineering in aqueous zinc-ion batteries yet, although the widely employed Mn-based and V-based cathodes have suffered from the strain provoked by "Jahn-Teller" effects within electrochemical reactions. The pre-introduction of strain could be a profitable strategy to offset the influence of "Jahn-Teller" effects and subsequently prohibit Mn dissolution in layered δ-MnO_2.

Herein, we employed a facile electrostatic self-assembly method to construct an ABAB-type MnO_2@rGO superlattice structure with pre-introduced strain, which was verified by geometric phase analysis and theoretical calculations. Various

characterizations and calculations have been applied to trace the resource of the generated strain that originated from the strong interaction between unilamellar MnO_2 and rGO nanosheets and the consequently induced lattice distortion within MnO_2 layers. Under the strain reinforcement, the MnO_2@rGO superlattice electrodes exhibited excellent cycling stability. *In-situ* static UV-vis spectra and *in-situ* synchrotron XRD were applied to investigate the function of pre-introduced strain in electrochemical processes. The advantageous build-in strain essentially suppressed the Mn dissolution during H^+/Zn^{2+} co-insertion reactions through synergistic effects of two types of strains, in terms of in-plane tensile and out-of-plane compressive strains and meanwhile improved kinetics in aqueous zinc-ion batteries.

5.2. Experimental

5.2.1 Materials syntheses

Preparation of δ-MnO_2 nanosheets: Typically, two solutions were prepared in advance. Solution A consists of 0.6M tetramethylammonium hydroxide (TMAOH) and 3 wt.% H_2O_2, and solution B is a fresh-made 0.3M $MnCl_2$ solution. Under stirring at room temperature, 20 mL solution A was dropwise added into 10 mL solution B. The resulted dark brown mixture was continuously stirred in the air for 12h. After centrifugation at 10000 rpm over 30 min, the collected precipitation was washed with DI water three times at the same speed and time by centrifugation to remove excess TMA^+ ions. Finally, the obtained sediment was redispersed in DI water and centrifugated at 5000 rpm for 10 min to collect a reddish-brown supernatant as the colloid δ-MnO_2 nanosheet solution.

Preparation of positive-charged rGO nanosheets: Poly(diallyldimethylammonium chloride) (PDDA) was applied to modified rGO nanosheets from negatively charged to positively charged. 500 mL GO suspension with a 0.2 mg/mL concentration, prepared by

the Hummer's method, was refluxed with 3.75 mL PDDA solution (20 wt.%) and 100 μL $N_2H_4H_2O$ solution (50~60 wt.%) at 90°C for 3h. The obtained dark mixture was centrifugated at 10000 rpm over 30 min to remove the excess PDDA in the supernatant. After another centrifugation of the redispersed sediment at 5000 rpm for 10 min, a stable suspension of positive-charged rGO nanosheets was recovered.

Preparation of δ-MnO_2@rGO superlattices: The as-prepared suspension of δ-MnO_2 nanosheets and positive-charged rGO nanosheets was stirred at room temperature with a mass ratio of m(δ-MnO_2): m(rGO)≈ 2.8: 1, calculated by the reported hypothetical area-matching model.[242] The electrostatic self-assembled δ-MnO_2@rGO superlattices presented flocculent precipitates within seconds that positive-charge rGO nanosheets with larger lateral sizes accommodate small negative-charged δ-MnO_2 nanosheets on surfaces, breaking the charge balance of colloid solutions, and units of MnO_2@rGO are continuously formed and accumulated until heavy particles precipitated. Then the sediments were separated by centrifugation and dried under vacuum at room temperature.

5.2.2 Materials characterization

A Bruker D8 Discover performed X-ray diffraction (XRD) to analyze the crystal structure. Atom force microscopy (AFM) via a Park XE7 was applied to characterize the thickness and lateral size. Scanning electron microscopy (SEM) was performed with a Zeiss Supra 55VP and field-emission transmission electron microscopy (TEM) to elucidate morphology with a Tecnai G2 F30 S-TWIN system. X-ray photoelectron spectroscopy (XPS) via an ESCALAB 250Xi was used to identify the energy states of component elements. A Renishaw inVia Raman microscopy carried out Raman spectra. An Agilent UV-Vis spectroscopy tested Ultraviolet-visual spectra. An SDT-2960 system

tested thermogravimetric analysis (TGA) in air condition from room temperature to 800 °C.

5.2.3 Cell assembly and electrochemical measurements

To prepare electrode slurries, active materials, carbon black and polyvinylidene fluoride (PVDF) were manually ground at a mass ratio of 7: 2: 1 in N-methyl-2-pyrrolidone (NMP) solvent. The mixture was then coated on hydrophobic carbon cloth current collectors and dried under vacuum at 100 °C overnight. The diameter of carbon cloth is 12 mm, and the average active material mass loading is ~1.2 mg cm^{-2}. The Zn-MnO_2 coin cells were assembled by Zn foil counter electrodes, glass fiber separators, and working electrodes with the electrolyte of 2M $ZnSO_4$+0.1M $MnSO_4$. For the electrochemical measurement, cyclic voltammetry (CV) at various scanning rates in a voltage window of 0.8 ~ 1.8 V was performed on a Bio-Logic VMP3 workstation. All galvanostatic tests, including cyclic and rate performance at various current densities between 0.8 and 1.8 V, were accomplished on Landt battery testers.

5.2.4 Computational methods

DFT calculations were presented with a plane-wave basis set as implemented in the Vienna ab initio simulation package, using the projector augmented-wave (PAW) method and DFT-D2 method for the multilayered systems considering van der Waals (vdW) interaction. For the exchange-correlation functional, we used the generalized gradient approximation in Perdew−Burke−Ernzerhof format with inclusion of van der Waals corrections. The energy cutoff for the plane-wave basis was set to 400 eV. 2D heterostructures were modeled by using a 5 × 7 supercell of MnO_2 on top of 6 × 8 supercell of graphene. All atoms were fully relaxed until the forces on each atom were

smaller than 0.01 eV/Å. A vacuum space of 25Å along the *z* direction is adopted to avoid the interaction between the neighboring layers.

5.3 Results and Discussion

5.3.1 Fabrication of MnO_2@rGO superlattice

The δ-MnO_2 nanosheets were synthesized via a modified wet-chemistry method, as reported.[297] Compared with the traditional procedures, the high-speed centrifugation was applied to separate monolayered δ-MnO_2 nanosheets from restacked or multi-layered counterparts. The obtained reddish-brown colloid solution shows a noticeable Tyndall effect (**Figure 5.1a**), suggesting the homogeneous dispersion of δ-MnO_2 nanosheets in water. After the freeze-drying process, δ-MnO_2 nanosheets are restacked with good flexibility, as shown in SEM images (**Figure 5.2**). To clearly identify the thickness of δ-MnO_2 monolayers, XRD was conducted to a filtrated δ-MnO_2 film, as shown in **Figure 5.1b**. Only (00*l*) series of peaks are found in XRD patterns with the peak position of (001) reflection at ~9.1°, indexing the *d* spacing of 0.97 nm. Meanwhile, the AFM results in **Figure 5.1c** also prove the thickness of the monolayered δ-MnO_2 nanosheet to be 0.9~1.0 nm. These results are well-matched with the reference of the TMA cations and water molecules co-intercalated Birnessite-phase MnO_2.[297]

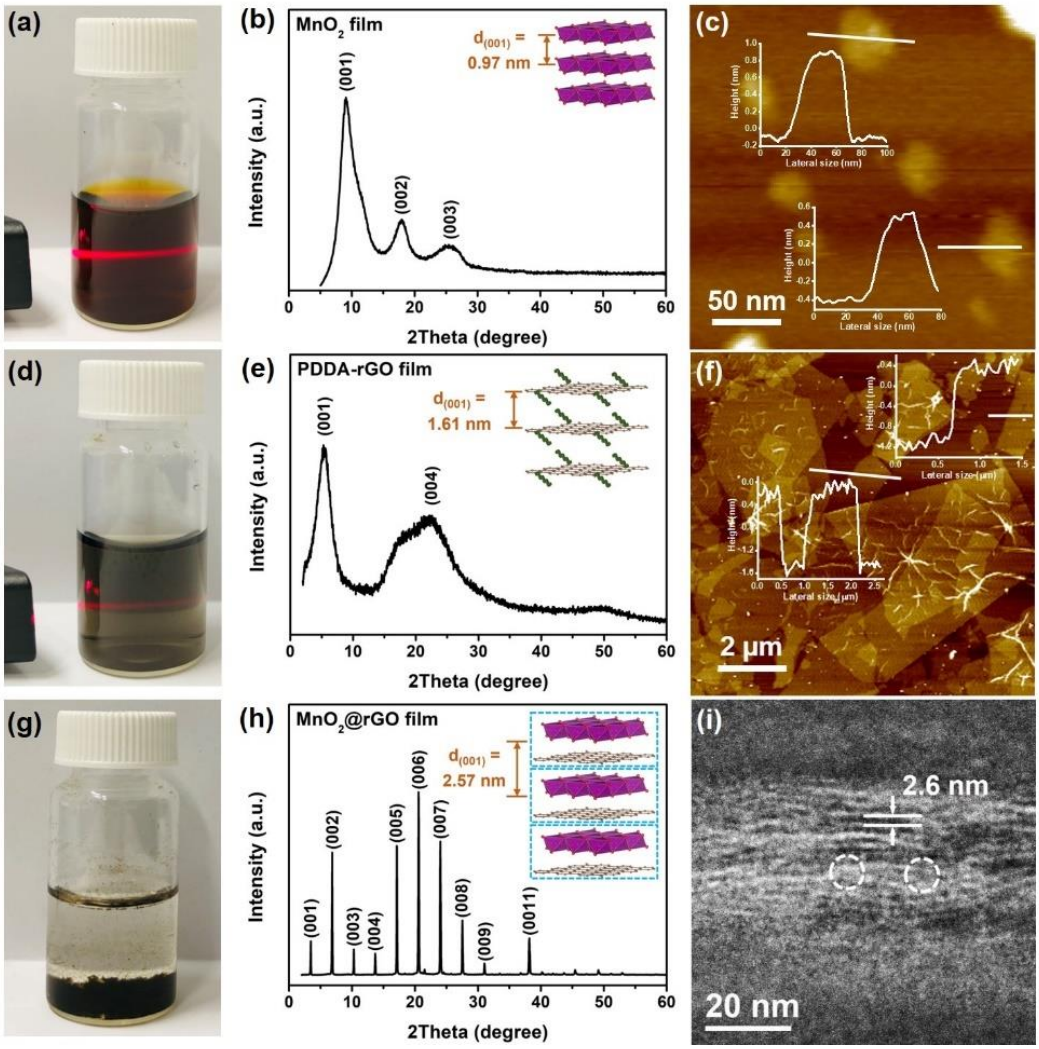

Figure 5.1 Fabrication of MnO_2@rGO superlattice. Digital images of (a) bare δ-MnO_2 and (d) PDDA-rGO colloid solutions and (g) MnO_2@rGO superlattice flocculation; XRD patterns with insets of schematic crystal structures for (b) δ-MnO_2, (e) PDDA-rGO, and (h) MnO_2@rGO superlattice films; AFM images of unilamellar (c) δ-MnO_2 and (f) PDDA-rGO nanosheets; and (i) cross-section TEM image of MnO_2@rGO superlattice (the dash line circles indicate the lattice dislocation).

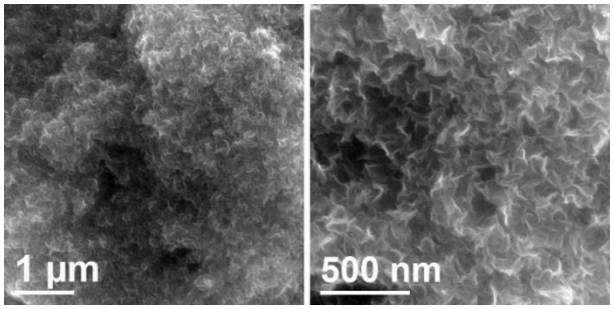

Figure 5.2 SEM images of restacked δ-MnO_2 nanosheets.

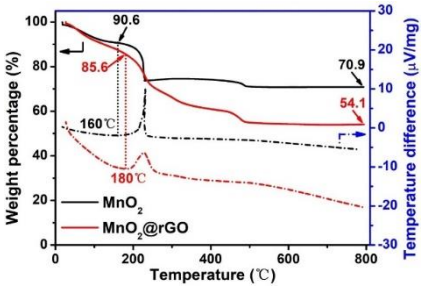

Figure 5.3 TGA results of restacked δ-MnO_2 nanosheets and MnO_2@rGO superlattice.

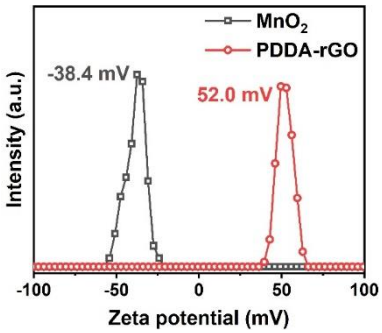

Figure 5.4 Zeta potential of MnO_2 and PDDA-rGO nanosheets.

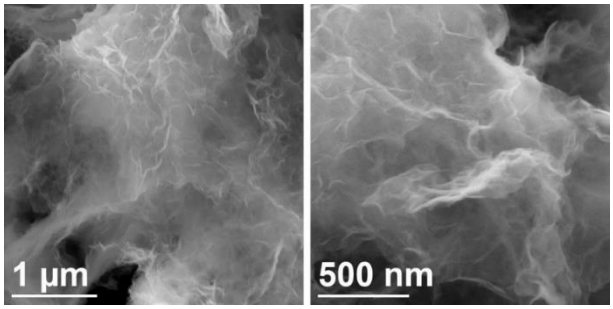

Figure 5.5 SEM images of the freeze-dried MnO_2@rGO superlattice.

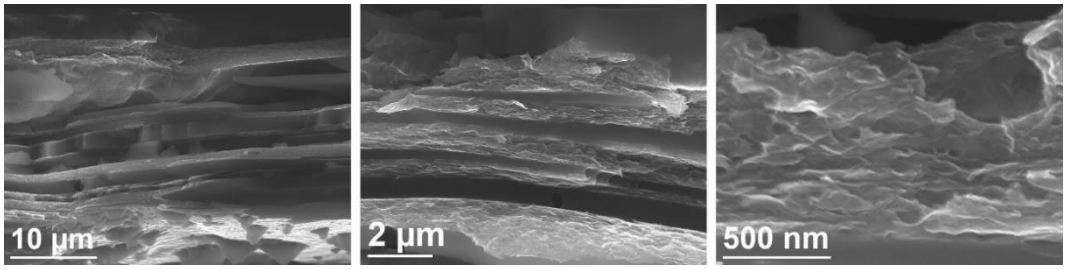

Figure 5.6 Cross-section SEM images of MnO_2@rGO superlattice films.

The positive-charged rGO nanosheets were prepared by reducing GO nanosheets and simultaneously grafting a high charge density cationic polymer PDDA as reported.[118,242] The manufactured PDDA modified rGO nanosheets can be dispersed in water and exhibit good stability (**Figure 5.1d**). The *d* spacing of PDDA-rGO is calculated as ~1.61 nm from XRD patterns (**Figure 5.1e**) of the filtrated PDDA-rGO film, associated with the AFM results (**Figure 5.1f**) for monolayered PDDA-rGO nanosheets of about 1.6 nm.

Typically, 2D superlattices constructed by 2D unilamellar nanosheets can be achieved by various techniques like layer-by-layer (LBL) assembly, Langmuir-Blodgett (LB) transfer, and spin coating.[298] In this case of MnO_2@rGO superlattice, the flocculation approach was applied based on an electrostatically self-assemble mechanism. Unilamellar δ-MnO_2 and PDDA-rGO nanosheets are the negative-charged and positive-charged building blocks. The colloid solutions of two species were mixed with a certain mass ratio of about 2.8:1, determined by the theoretical crystal lattice matching.[242] The real weight percentage of PDDA-rGO was calculated as 25.3% from TGA results (**Figure 5.3**), close to the theoretical value of 26.3%. After resting, flocculation-like sediment with a clear supernatant (**Figure 5.1g**) was obtained since the strongly negative and positive charges on MnO_2 (zeta potential −38.4 mV) and PDDA-rGO (zeta potential 52.0 mV) nanosheets (**Figure 5.4**). Benefitting from the large lateral size of the PDDA-rGO skeleton, the freeze-dried superlattice-like nanosheets also exhibit excellent flexibility observed from SEM images (**Figure 5.5**). Therefore, a MnO_2@rGO membrane can be attained by

filtration and applied for XRD characterization. **Figure 5.1h** shows that XRD peaks of (00*l*) reflections have extreme intensities and narrow full widths at half maximum (FWHMs), indicating the good crystallinity for the *c* axis of the superlattice film based on the Scherrer equation. This can also be proved by the highly stacking degree of MnO_2@rGO nanosheets in the cross-section SEM images (**Figure 5.6**). The position of (001) peaks is located at 3.45°, indexing the *d* spacing of ~2.57 nm for a superlattice unit (MnO_2 monolayer plus PDDA-rGO monolayer), which is perfectly aligned with the thickness of two unilamellar building blocks. Moreover, the *c*-axis lattice parameter of MnO_2@rGO superlattice can be directly read as ~2.6 nm from the cross-section TEM image (**Figure 5.1i**), where the white spots and lines represent the metallic Mn ions in MnO_2 and the nonmetallic C atoms from rGO nanosheets are distributed between them as the schematic illustrates in **Figure 5.1h**. Besides, the TEM image demonstrates a multi-layer (over 10 layers) stacking morphology in the micro scale with lattice dislocation marked in circles. This could be ascribed to the strong interaction between MnO_2 and rGO.

5.3.2 Lattice distortion-induced strain in superlattice

Density functional theory (DFT) calculations were applied to determine the interaction between unilamellar MnO_2 and graphene nanosheets. The charge density difference of the MnO_2@graphene profile was presented in **Figure 5.7a**, where the yellow and blue regions imply the charge accumulation and depletion, respectively. At the interfacial area between graphene and MnO_2 layers, the yellow regions are clustered around the MnO_2 surface, suggesting the electrons accumulate there, while the surface of the graphene layer is nearly covered by blue regions, indicating the intense hole aggregation. However, no charge density redistribution can be found in a typical bilayer MnO_2 structure (**Figure 5.8**). The root of such drastic charge redistribution is attributed to the strong chemical

bonding between graphene and MnO_2 layers, and the change of Mn 3d orbitals takes the responsibility. In the projected density of states (PDOS) (**Figure 5.7b**), the d-band center of Mn 3d in superlattice arises ~0.4 eV compared with the original state, proving the existence of the strong interaction.

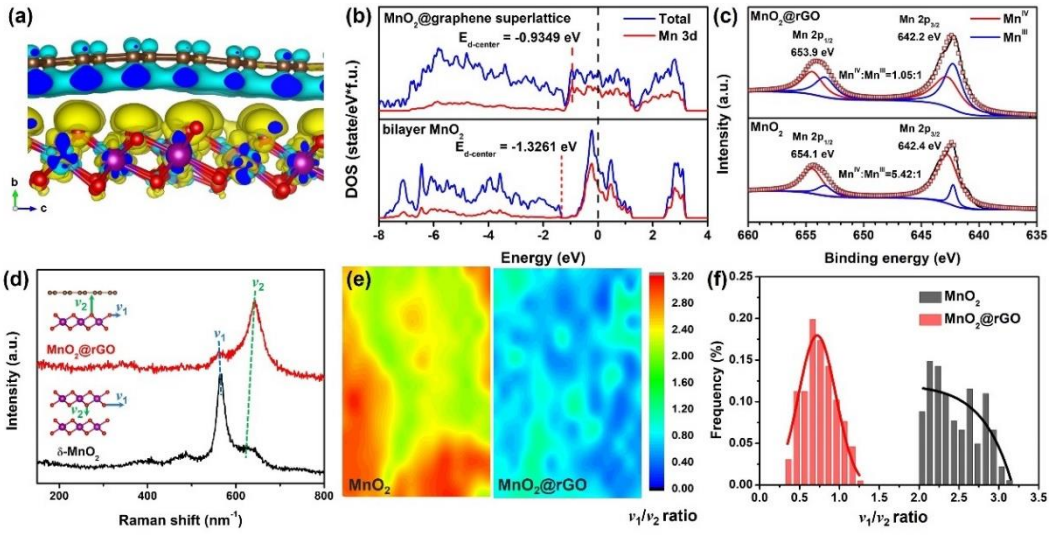

Figure 5.7 Lattice distortion in MnO_2@rGO superlattice. (a) Differential charge density distribution in MnO_2@graphene superlattice. (b) DOS of Mn 3d orbitals in bilayer MnO_2 nanosheets and MnO_2@graphene superlattice. (c) High resolution Mn 2p XPS of bare MnO_2 and MnO_2@rGO superlattice. (d) Raman spectra (the inset illustrates v_1 and v_2 stretching modes) with (e) contour graph and (f) statistical bar chart of v_1/v_2 ratios of bare MnO_2 and MnO_2@rGO superlattice.

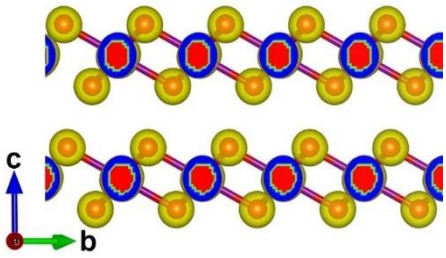

Figure 5.8 Charge density distribution in bilayer MnO_2 nanosheets.

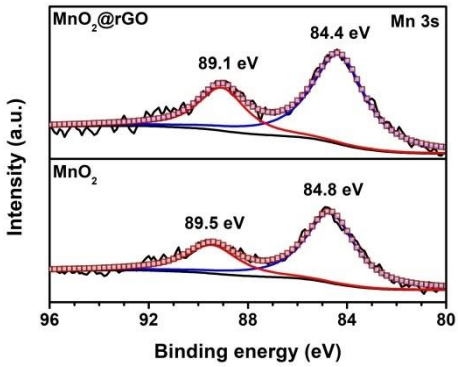

Figure 5.9 High-resolution Mn 3s spectra of bare MnO_2 nanosheets and MnO_2@rGO superlattice.

XPS characterizations were employed to quantify the valence states of Mn in both materials. **Figure 5.7c** compares high-resolution Mn 2p spectra of bare MnO_2 and MnO_2@rGO superlattice. The Mn $2p_{1/2}$ and $2p_{3/2}$ peaks of bare MnO_2 are located at 654.1 and 642.4 eV, respectively, with a binding energy gap of 11.7 eV, corresponding to a typical Birnessite-phase MnO_2. However, the overall peaks in MnO_2@rGO superlattice are blue-shifted 0.2 eV, suggesting the valence-state decrease of the Mn element. The blue shifts are also found in its Mn 3s spectra (**Figure 5.9**), with a higher degree of 0.4 eV. Further analysis of simulated peaks indicates two valence states of Mn elements in both materials, in terms of IV and III values, in which peak areas determine their percentages. After coupling with rGO nanosheets, unilamellar MnO_2 nanosheets have a dramatically increase of Mn^{III} components in both Mn $2p_{1/2}$ and $2p_{3/2}$ peaks with a Mn^{IV}/Mn^{III} ratio of 1.05:1 falling from 5.42:1, providing its accurate valence state on Mn of ca. +3.52, while the calculated value for the bare counterpart is ca. +3.84. Such highly valence-state reduction may trigger the crystal lattice distortion of MnO_2 nanosheets in the superlattice.

Raman was conducted to analyze the Mn−O bonding status in bare MnO_2 and MnO_2@rGO superlattice, as shown in **Figure 5.7d**. There are two dominating Mn−O

stretching modes in MnO_6 octahedra, in terms of the in-plane stretching vibration v_1 paralleled with the linked [MnO_6] sheets and the out-of-plane band v_2 perpendicular to the sheets as inset demonstrates. Previous investigations revealed that both v_1 and v_2 stretching vibrations are very sensitive to intercalated species among interlayers, especially the size.[299,300] In Birnessite-type MnO_2, the larger cation substitutions can weaken the interaction among interlayers, performing as a redshift of v_2 stretching vibrations.[288] In this case of MnO_2@rGO superlattice, the remarkable downshift of v_2 band from 625 nm^{-1} to 642 nm^{-1} is ascribed to the replacement of TMA cations by positive-charged rGO nanosheets, which has already reflected on the dramatic *d*-spacing increase in XRD patterns. Meanwhile, the v_2 band has the opposite shifting direction of the v_1 counterpart. Another important finding is the astonishing intensity changes of v_1 and v_2 stretching vibrations when comparing Raman spectra between bare MnO_2 and MnO_2@rGO superlattice. Over 200 quantified intensity ratios, v_1/v_2, calculated from Raman mapping results for each candidate were presented in contour graphs (**Figure 5.7e**) and a statistical bar chart (**Figure 5.7f**). Bare MnO_2 has an obviously higher overall v_1/v_2 ratios than MnO_2@rGO superlattice, attributed to the greater Mn^{IV} occupying rate (proved by XPS results) than the counterpart on the one hand.[299] The other reason should benefit from the superlattice construction where the large lateral size capping agents rGO nanosheets encapsulate every unilamellar MnO_2 nanosheets through electrostatic force but also hydrogen bonding to surface hydroxyl groups on MnO_2. The reported study found that the adsorption energy between MnO_2 and capping agents has an antilinear relationship with the v_1/v_2 ratios.[300] Therefore, the extraordinary decreasing v_1/v_2 ratios are the pronouncing evidence of the strong interaction between unilamellar MnO_2 and rGO nanosheets. Furthermore, the relatively lower v_1/v_2 ratios are mainly concentrated on the center of the aggregated MnO_2 nanosheets in the contour graph, reversely, the exposed

edges with higher v_1/v_2 ratios are more likely to be totally dominated by the out-of-plane v_1 stretching vibrations, suggesting the poor stability of MnO_6 octahedra blocks at the edge sites. Differently, the distribution of v_1/v_2 ratios on the MnO_2@rGO superlattice is more uniform and random as observed from the contour graph and in statistics obeying Gaussian distribution. In general, coupling with rGO nanosheets gives a more stable environment to MnO_2 nanosheets, but such large change of Mn−O bonding status may cause a lattice distortion of MnO_2 due to its low resistance to "Jahn-Teller" effect.

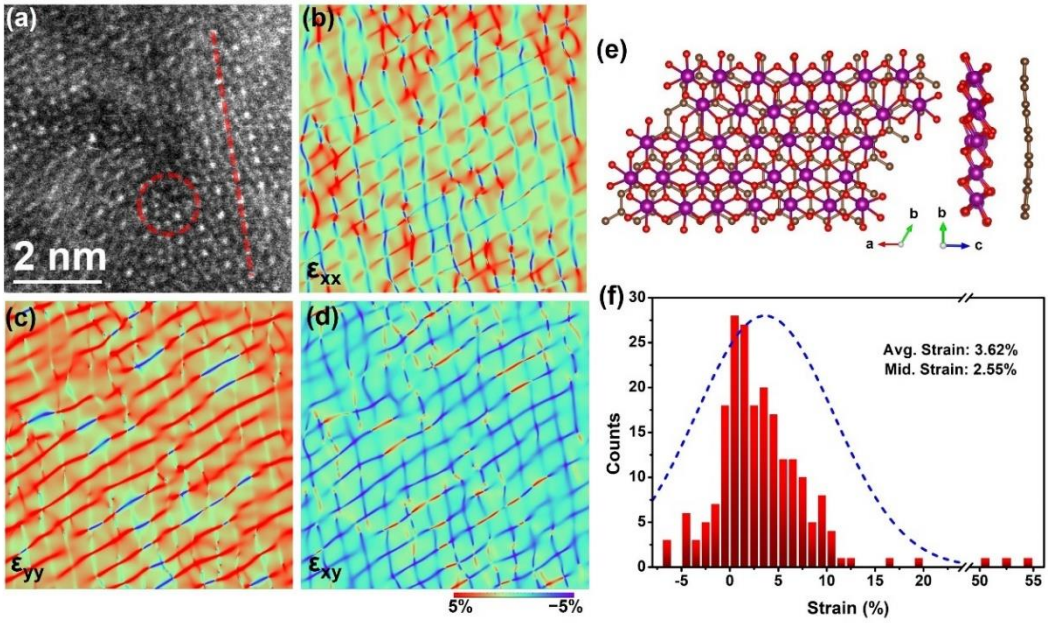

Figure 5.10 Strain in MnO_2@rGO superlattice. (a) aberration-corrected HAADF-STEM image of MnO_2@rGO superlattice (the lattice distortion marked by red dash line and circle) and the related (b) ε_{xx}, (c) ε_{yy}, and (d) ε_{xy} strain components after GPA treatments. (e) The optimized MnO_2@graphene superlattice structure after DFT calculations and (f) the calculated statistical strain distribution in the superlattice unit.

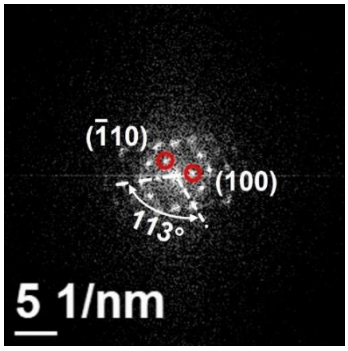

Figure 5.11 Fast Fourier transferred selected area electron diffraction (FFT-SAED) image of MnO_2@rGO superlattice.

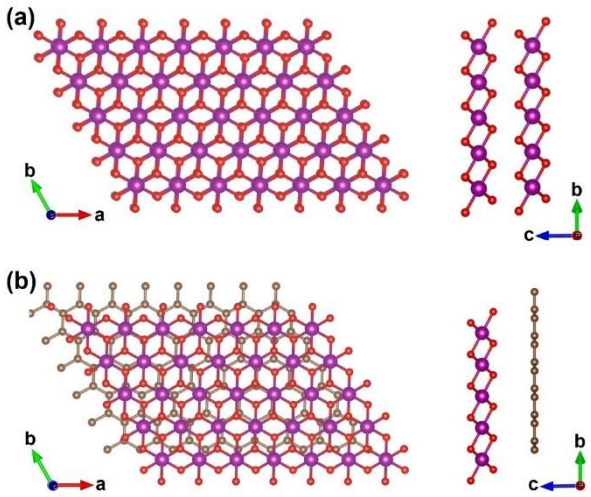

Figure 5.12 Calculated structure of (a) bilayer MnO_2 nanosheets and (b) MnO_2@graphene superlattice.

The lattice distortion of δ-MnO_2 can be directly observed from the aberration-corrected high-angle annular dark-field scanning transmission electron microscopy (HDDAF-STEM) image in **Figure 5.10a**. The light spots indicate the position of Mn atoms in the lattices. The red dash line as the reference marks the deviation of the Mn atoms from the standard lattice. Obviously, the lattice aberration of MnO_2 is expected in the superlattice structure. Besides, the lattice mismatch is also detected in the red dash circle region. The corresponding fast Fourier transferred selected area electron diffraction (FFT-SAED) image was presented in **Figure 5.11**, showing hexagonal diffraction spots of the single

crystal MnO_2. The angle between (100) and ($\bar{1}$10) facets is measured as 113°, much lower than the value (120°) in a typical hexagonal Birnessite-phase MnO_2.[301] Those results pronouncedly prove the existence of severe lattice distortion for MnO_2 in the superlattice structure, well-matched with the inference from Raman spectra.

Furthermore, the geometrical phase analysis (GPA) technique was applied to quantify the local strain field relaxation distribution in the superlattice, based on the HDDAF-STEM image. Taking *x* and *y* axis parallel to [100] and [$\bar{1}$10], respectively, the simulated strain field maps were presented in **Figure 5.10b-d**, in which the ε_{xy} strain component reflects the strain along [002] direction. The overall stains mainly distribute at the range of −5~5%, where the minus values displaying with cold colors represent the compressive strains, while the positive values with warm colors correspond to tensile strains. In **Figure 5.10b**, both compressive and tensile strains exist along with the lattice, but some regions show very strong tensile strains with red color, which are associated with the lattice mismatch areas in **Figure 5.10a**. However, the strain field distributions in **Figure 5.10c** and **d** are relatively monotonous and dominated by tensile and compressive strains, respectively, although the positions of strain follow the similar direction of lattice as ε_{xx} strain component. In conclusion, the compressive strains are mainly distributed along the *c*-axis direction since the strong interactions between MnO_2 and rGO strengthen the out-of-plane vibrations of Mn−O bonds. Oppositely, the in-plane vibrations of Mn−O bonds are passively weakened to stabilize the structure, and thus the strain components at this region are dominated by tensile species.

DFT calculations were conducted to confirm this hypothesis. Compared with the bilayer MnO_2 and initial state of MnO_2@graphene superlattice structures (**Figure 5.12**), the optimized superlattice (**Figure 5.10e**) displays apparent lattice distortions of both

MnO_2 and graphene sheets. The distortion-induced strain in MnO_2 cells can be calculated based on the length change of Mn−O bonds as the equation:

$$\varepsilon\% = \frac{L_{\text{Mn-O}}(MnO_2@rGO) - L_{\text{Mn-O}}(MnO_2)}{L_{\text{Mn-O}}(MnO_2)} \times 100\%.$$

The calculated results were performed in **Table 5.1** and the statistical bar chart of **Figure 5.10f.** Strains predominantly spread in the range of −5~10% obeying the Gaussian distribution and concentrate among 0~5% with the average and median values of 3.62% and 2.55%, respectively. These results are well-coordinated with local strain field relaxation distribution gained from GPA.

Table 5.1 Position of Mn and O sites with corresponding bond lengths of Mn−O in original bilayer MnO_2 nanosheets (BL_0) and modified MnO_2@graphene superlattice (BL), and the calculated strain ε.

Mn	O	BL_0(Å)	BL(Å)	ε(%)	Mn	O	BL_0(Å)	BL(Å)	ε(%)	Mn	O	BL_0(Å)	BL(Å)	ε(%)
1	1	1.87549	1.79958	-4.05	12	22	1.82832	1.86463	1.99	24	38	1.88997	1.85365	-1.92
1	9	1.89007	1.99029	5.30	12	23	1.87565	1.86229	-0.71	24	45	1.89007	2.05871	8.92
1	10	1.82832	1.96553	7.50	13	14	1.87575	1.87936	0.19	24	46	1.82817	1.85752	1.61
1	61	1.82832	1.92238	5.14	13	15	1.82832	1.91595	4.79	24	47	1.87549	1.94469	3.69
1	62	1.88997	1.94638	2.98	13	16	1.88997	1.92592	1.90	25	38	1.87575	1.94992	3.95
1	70	1.87575	1.89221	0.88	13	23	1.89008	1.95696	3.54	25	39	1.82832	1.91746	4.88
2	1	1.89007	2.88791	52.79	13	24	1.82832	1.83986	0.63	25	40	1.88997	2.01626	6.68
2	2	1.82832	1.80769	-1.13	13	25	1.87565	1.89296	0.92	25	47	1.89007	1.88172	-0.44
2	3	1.87549	1.96005	4.51	14	16	1.87575	1.98438	5.79	25	48	1.82817	1.89683	3.76
2	62	1.87575	1.91211	1.94	14	17	1.82832	1.99578	9.16	25	49	1.87549	1.91884	2.31
2	63	1.82832	1.85179	1.28	14	18	1.88997	1.90293	0.69	26	41	1.82832	2.03437	11.27
2	64	1.88997	1.77315	-6.18	14	25	1.89008	1.87351	-0.88	26	42	1.88997	1.83054	-3.14
3	3	1.89007	1.84743	-2.26	14	26	1.82832	1.84527	0.93	26	50	1.87575	1.78553	-4.81
3	4	1.82832	1.91079	4.51	14	27	1.87564	1.88442	0.47	26	51	1.87565	2.06982	10.35
3	5	1.87549	1.84905	-1.41	15	18	1.87575	1.88865	0.69	26	59	1.89008	2.02246	7.00
3	64	1.87575	2.04237	8.88	15	19	1.82832	1.98971	8.83	26	60	1.82832	1.79072	-2.06
3	65	1.82832	1.93996	6.11	15	20	1.88997	1.92226	1.71	27	42	1.87575	1.88186	0.33
3	66	1.88997	1.94485	2.90	15	27	1.89008	1.90828	0.96	27	43	1.82832	1.86375	1.94
4	5	1.89007	2.00825	6.25	15	28	1.82832	1.87078	2.32	27	44	1.88997	1.86663	-1.23

4	6	1.82832	1.99498	9.12	15	29	1.87565	1.96666	4.85	27	51	1.89008	2.05865	8.92
4	7	1.87549	1.94092	3.49	16	21	1.82832	1.96280	7.36	27	52	1.82832	2.01008	9.94
4	66	1.87575	1.89675	1.12	16	22	1.88997	1.93591	2.43	27	53	1.87565	1.94185	3.53
4	67	1.82832	1.88564	3.14	16	30	1.87575	1.93770	3.30	28	44	1.87575	1.82241	-2.84
4	68	1.88997	1.84702	-2.27	16	31	1.87565	1.93335	3.08	28	45	1.82832	1.88387	3.04
5	7	1.89007	1.85530	-1.84	16	39	1.89008	1.98772	5.17	28	46	1.88997	1.84467	-2.40
5	8	1.82832	1.88000	2.83	16	40	1.82832	1.84774	1.06	28	53	1.89008	2.07851	9.97
5	9	1.87549	1.86705	-0.45	17	22	1.87575	1.89811	1.19	28	54	1.82832	1.73784	-4.95
5	68	1.87575	1.97724	5.41	17	23	1.82832	1.92743	5.42	28	55	1.87565	2.02470	7.95
5	69	1.82832	1.99917	9.34	17	24	1.88997	2.03047	7.43	29	46	1.87575	2.01924	7.65
5	70	1.88997	2.02150	6.96	17	31	1.89008	1.90316	0.69	29	47	1.82832	1.88430	3.06
6	1	1.82832	1.74856	-4.36	17	32	1.82832	1.87220	2.40	29	48	1.88997	1.90086	0.58
6	2	1.88997	2.26342	19.76	17	33	1.87565	2.01909	7.65	29	55	1.89008	1.93993	2.64
6	10	1.87560	1.90352	1.49	18	24	1.87575	1.88419	0.45	29	56	1.82832	1.94027	6.12
6	11	1.87565	1.75640	-6.36	18	25	1.82832	2.02556	10.79	29	57	1.87565	1.87352	-0.11
6	19	1.89008	1.82639	-3.37	18	26	1.88997	1.99313	5.46	30	48	1.87575	1.86141	-0.76
6	20	1.82832	1.96501	7.48	18	33	1.89008	1.89655	0.34	30	49	1.82832	1.84579	0.96
7	2	1.87560	1.88352	0.42	18	34	1.82832	1.85626	1.53	30	50	1.88997	1.89055	0.03
7	3	1.82832	1.87703	2.66	18	35	1.87565	1.91027	1.85	30	57	1.89008	1.89349	0.18
7	4	1.88997	1.81658	-3.88	19	26	1.87575	1.89610	1.08	30	58	1.82832	1.97043	7.77
7	11	1.89008	2.91713	54.34	19	27	1.82832	1.86870	2.21	30	59	1.87565	2.11117	12.56
7	12	1.82832	1.82789	-0.02	19	28	1.88997	1.89217	0.12	31	51	1.82832	1.99593	9.17
7	13	1.87565	1.85373	-1.17	19	35	1.89008	2.01105	6.40	31	52	1.88997	1.87240	-0.93
8	4	1.87560	1.91509	2.11	19	36	1.82832	1.91073	4.51	31	60	1.87575	2.00421	6.85
8	5	1.82832	1.88929	3.33	19	37	1.87564	1.95802	4.39	31	61	1.87565	1.93061	2.93
8	6	1.88997	1.89642	0.34	20	28	1.87575	1.92721	2.74	31	69	1.89008	1.90516	0.80
8	13	1.89008	1.91222	1.17	20	29	1.82832	1.85575	1.50	31	70	1.82832	1.84502	0.91
8	14	1.82832	1.91355	4.66	20	30	1.88997	2.00944	6.32	32	52	1.87575	1.85796	-0.95
8	15	1.87565	1.94199	3.54	20	37	1.89008	1.87121	-1.00	32	53	1.82832	1.83064	0.13
9	6	1.87560	1.88497	0.50	20	38	1.82832	1.94659	6.47	32	54	1.88997	2.84540	50.55
9	7	1.82832	1.91116	4.53	20	39	1.87565	1.94930	3.93	32	61	1.89008	1.80876	-4.30
9	8	1.88997	1.91040	1.08	21	31	1.82832	1.84103	0.70	32	62	1.82832	1.84924	1.14
9	15	1.89008	1.97831	4.67	21	32	1.88997	1.87588	-0.75	32	63	1.87565	1.95876	4.43
9	16	1.82832	1.89266	3.52	21	40	1.87575	1.87517	-0.03	33	54	1.87575	1.74976	-6.72
9	17	1.87564	1.87094	-0.25	21	41	1.87549	1.98042	5.59	33	55	1.82832	1.90885	4.40
10	8	1.87560	1.87617	0.03	21	49	1.89007	1.97313	4.39	33	56	1.88997	1.92598	1.91
10	9	1.82832	1.87816	2.73	21	50	1.82817	2.13362	16.71	33	63	1.89008	1.99621	5.62
10	10	1.88997	1.91610	1.38	22	32	1.87575	1.99279	6.24	33	64	1.82832	1.91068	4.50
10	17	1.89008	1.87345	-0.88	22	33	1.82832	1.86730	2.13	33	65	1.87565	1.93027	2.91
10	18	1.82832	1.93304	5.73	22	34	1.88997	1.88505	-0.26	34	56	1.87575	1.95252	4.09

10	19	1.87565	2.00253	6.76	22	41	1.89007	2.06880	9.46	34	57	1.82832	1.97697	8.13
11	11	1.82832	1.74640	-4.48	22	42	1.82817	1.93321	5.75	34	58	1.88997	1.86431	-1.36
11	12	1.88997	1.95702	3.55	22	43	1.87549	1.89587	1.09	34	65	1.89008	1.92631	1.92
11	20	1.87575	1.96536	4.78	23	34	1.87575	1.93906	3.38	34	66	1.82832	1.85847	1.65
11	21	1.87565	1.86550	-0.54	23	35	1.82832	1.83786	0.52	34	67	1.87565	1.90635	1.64
11	29	1.89008	1.95296	3.33	23	36	1.88997	1.98222	4.88	35	58	1.87575	1.86404	-0.62
11	30	1.82832	1.88098	2.88	23	43	1.89007	1.92279	1.73	35	59	1.82832	2.02704	10.87
12	12	1.87575	2.01616	7.49	23	44	1.82817	1.99328	9.03	35	60	1.88997	2.01186	6.45
12	13	1.82832	2.02780	10.91	23	45	1.87549	1.94748	3.84	35	67	1.89008	1.88467	-0.29
12	14	1.88997	1.96465	3.95	24	36	1.87575	1.92190	2.46	35	68	1.82832	1.86375	1.94
12	21	1.89008	1.90904	1.00	24	37	1.82832	1.91996	5.01	35	69	1.87565	1.88483	0.49

5.3.3 Electrochemical stability in aqueous zinc-ion batteries

Before conducting electrochemical tests of bare MnO_2 and MnO_2@rGO superlattice in zinc-ion batteries, we investigated the statical stability of two materials through *in-situ* UV-vis characterizations in the acid electrolytes, 2M $ZnSO_4$ aqueous solution with the additive of 0.1M $MnSO_4$, which will be applied in the following battery test. Two electrodes with mass loadings of ~2.5 mg cm^{-2} were put at the bottom of UV-vis cells and immersed by the electrolytes with a relatively higher ratio of m(active materials): V(electrolytes)= 1 mg: 0.5 mL than that usually used in zinc-ion batteries. The dissolving status of the two types of materials is clearly performed via the change of the time-dependent UV-vis spectra (**Figure 5.13a**). Both materials are dissolved in the electrolytes, presenting a redshift of wavelength associated with the continuously dissolving Mn^{2+} ions due to the corrosion of H^+ ions from the acid electrolyte, especially in the first 2 hours. This is more clearly shown in wavelength-time plots (**Figure 5.14**), where the wavelength is collected from the midpoint of the slope in UV-vis spectra. After resting for 3 hours, the increasing rates of redshifted wavelengths slow down, representing the dynamic equilibrium of the dissolution of Mn^{2+} in the electrolytes. However, the bare MnO_2 electrode demonstrates a much faster Mn^{2+} dissolving speed and larger redshift than the MnO_2@rGO superlattice, ascribing to the lower resistance to the H^+ corrosion. Moreover,

the broad ranges of *in-situ* UV-vis spectra for bare MnO_2 electrodes cover the peak at 221 nm belonging to δ-MnO_2 colloid (**Figure 5.15**), indicating the decomposition of MnO_2 nanosheets during the resting process. That means its large UV-vis redshifts are also contributed by the increasing amount of dissolved MnO_2 fragments. Whereas no peak of δ-MnO_2 or PDDA-rGO is found in *in-situ* UV-vis spectra of MnO_2@rGO superlattice electrode.

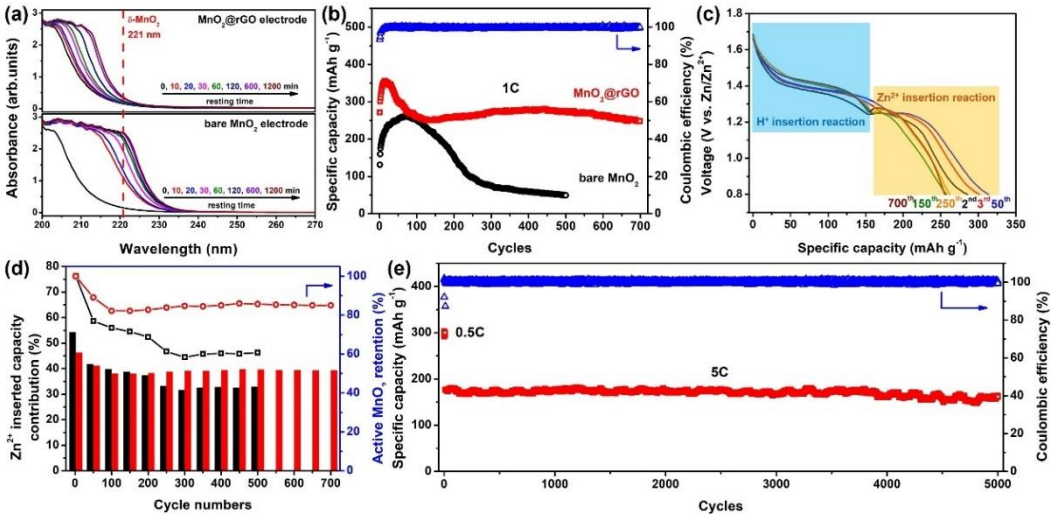

Figure 5.13 Electrochemical stability in aqueous zinc-ion batteries. (a) Time-dependent *in-situ* Raman spectra of bare MnO_2 and MnO_2@rGO superlattice electrodes immersed in electrolytes. (b) Cycling performance of bare MnO_2 and MnO_2@rGO superlattice electrodes at the rate of 1C. (c) Galvanostatic discharge curves of MnO_2@rGO superlattice electrodes at various cycles with (d) the calculated capacity contributions by Zn^{2+} insertion reaction and active MnO_2 retention ratios after cycles for bare MnO_2 and MnO_2@rGO superlattice electrodes. (e) Long-term cycling life of MnO_2@rGO superlattice electrodes at a high rate of 5C.

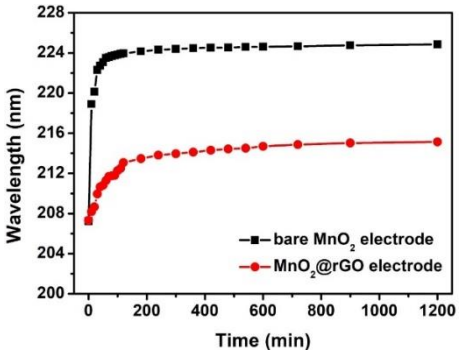

Figure 5.14 *In-situ* UV-vis spectra wavelength-time plots of bare MnO_2 and MnO_2@rGO superlattice electrodes.

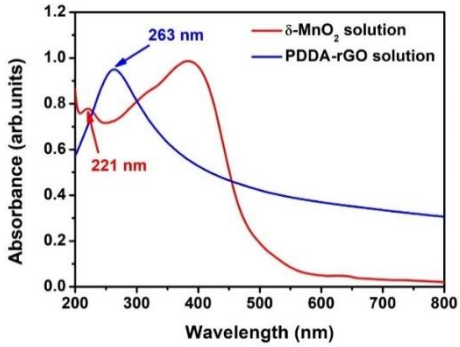

Figure 5.15 UV-vis spectra of δ-MnO_2 and PDDA-rGO colloid solutions.

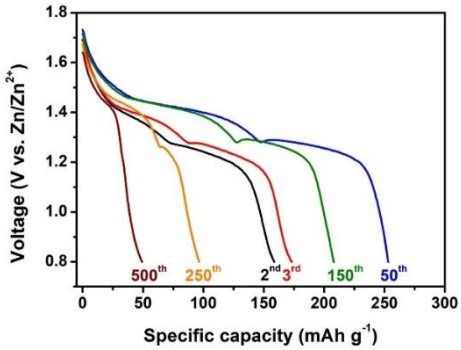

Figure 5.16 Galvanostatic discharge profiles of bare MnO_2 electrodes at various cycles.

The electrochemical performance of bare MnO_2 and MnO_2@rGO superlattice electrodes was tested in full zinc-ion batteries using fresh Zn foil anodes. **Figure 5.13b** is the cycling behavior of both electrodes at the current density of 1C (308 mA g^{-1}). The MnO_2@rGO superlattice electrodes exhibit a reversible specific capacity of 270 mAh g^{-1}

with a high initial Coulombic efficiency of 93.4%. After activation, the specific capacity is stabilized with Coulombic efficiencies close to 100% and capacity retention of 91.2% over 700 cycles. In contrast, the bare MnO_2 electrodes deliver a deficient initial reversible capacity and a long activating duration adjacent by a quick capacity fading within 300 cycles. Only ~50 mAh g^{-1} specific capacity has remained after 500 cycles. The cycling stability is also reflected in the galvanostatic discharge profiles (**Figure 5.13c & 5.16**) of both electrodes. Compared with the bare MnO_2 electrodes, the MnO_2@rGO superlattice electrodes display more likely overlapped discharge curves during cycles. Noticeably, there is an "inflection point" at ~1.25V dividing a discharge profile into two plateaus, as reported, a transformation indicator of the energy storage mechanism from H^+ insertion to Zn^{2+} insertion.[302] However, in the discharge profile of bare MnO_2 electrodes, the boundary of those two reactions becomes inconspicuous after 500 cycles since the H^+ insertion reaction possesses superior kinetics that dominates the discharge process.[289] That means the capacity contribution by the Zn^{2+} insertion reaction decreases during cycling. Therefore, we calculated and compared the Zn^{2+} insertion capacity contribution of both electrodes from the second cycle, as shown in **Figure 5.13d**. Compared with MnO_2@rGO superlattice electrodes, bare MnO_2 electrodes have a higher initial Zn^{2+} insertion capacity contribution of ~54% but faster dropping within cycles. After 500 cycles, the value reduces to only 32%, while MnO_2@rGO superlattice electrodes have a stable capacity contribution of ~40% from the 100^{th} cycle. Furthermore, as the final product of the Zn^{2+} insertion into δ-MnO_2 is $ZnMn_2O_4$, the change of Zn^{2+} insertion capacity contribution can semi-quantify the retention percentage of active MnO_2 using the initial value as reference. The calculated result in **Figure 5.13d** demonstrates that MnO_2@rGO superlattice electrodes possess over 85% active MnO_2 even after 700 cycles. On the contrary, only 60% active materials are left in bare MnO_2 electrodes, accompanied

by the continuous losing before the 300th cycle. Consequently, the capacity deterioration of bare MnO_2 electrodes is attributable to the large amount failing of active MnO_2. Combining with the *in-situ* UV-vis outcomes, the root of the poor cycling stability in bare MnO_2 electrodes is the permanent dissolution of Mn^{2+} ions and MnO_2 fragments. Oppositely, MnO_2@rGO superlattice electrodes survive in the Mn^{2+} dissolution because of the strain reinforcement. Even at a high rate of 5C, they also present excellent long-term cycling stability over 5000 cycles with a reversible capacity of 165 mAh g^{-1} (**Figure 5.13e**).

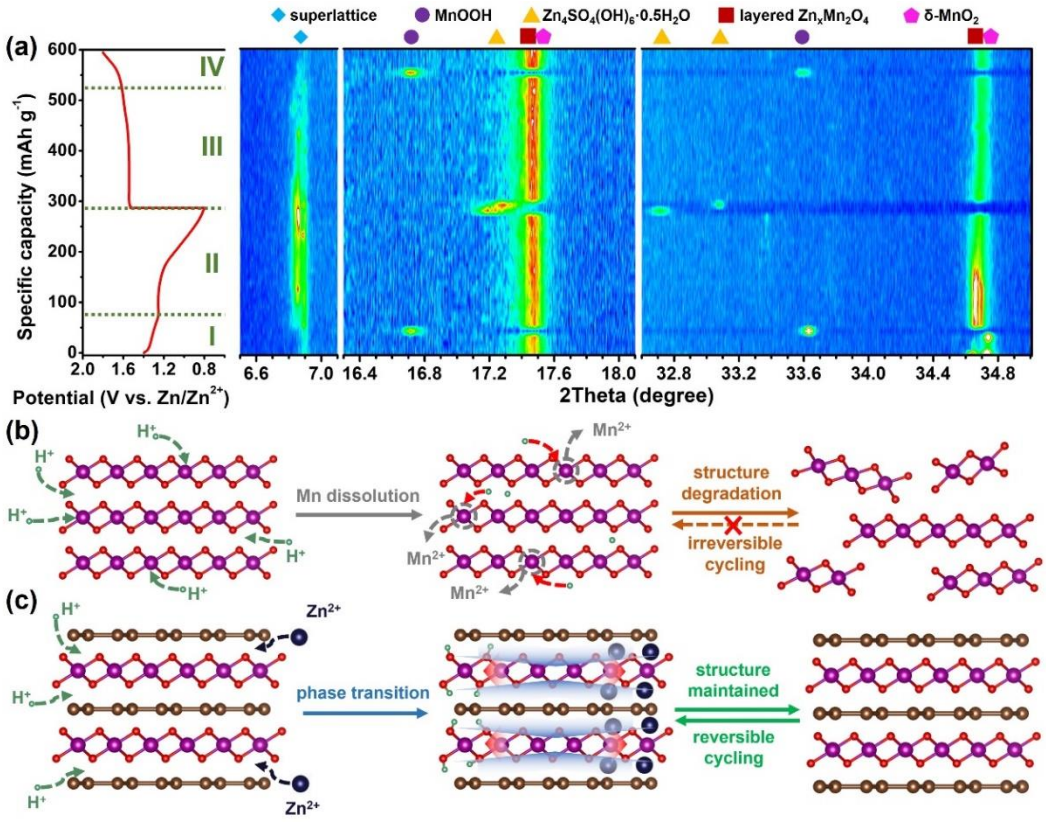

Figure 5.17 Zn storage mechanism in MnO_2@rGO superlattice. (a) *In-situ* synchrotron XRD contour graphs within a full cycle and the related galvanostatic discharge/charge profiles at the current density of 0.5C. Schematic illustration of (b) the structure degradation for bare MnO_2 electrodes and (c) good structural stability of MnO_2@rGO superlattice electrodes.

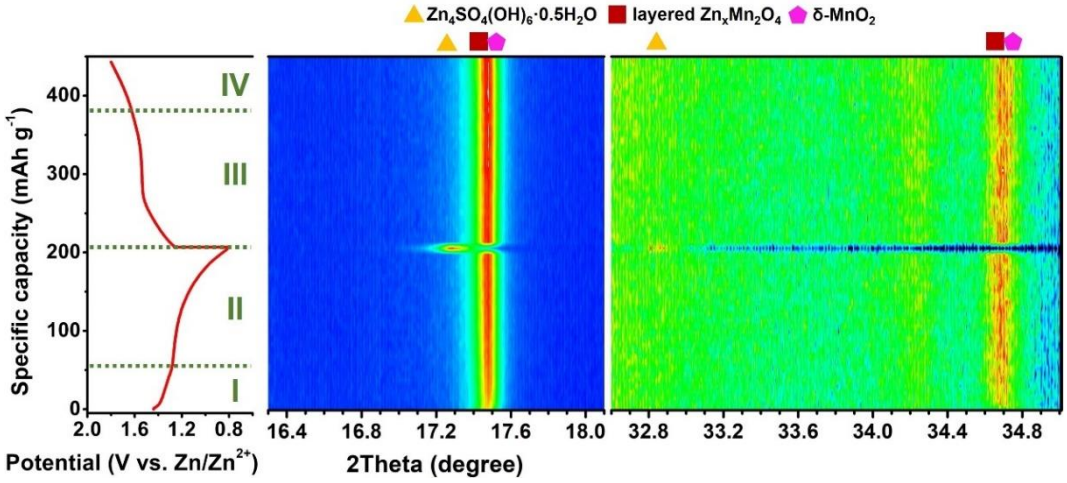

Figure 5.18 *In-situ* synchrotron XRD contour graphs of bare MnO_2 electrodes within a full cycle and the related galvanostatic discharge/charge profiles at the current density of 0.5C.

In-situ synchrotron XRD was employed to investigate the Zn storage mechanism of MnO_2@rGO superlattice. In **Figure 5.17a**, the galvanostatic discharge/charge profiles can be divided into four regions, corresponding to the H^+ intercalation/deintercalation (region I/IV) and the Zn^{2+} insertion/extraction (region II/III). The original superlattice peak in the XRD contour graph is at ~6.9°, associated with the (002) facet as indexed in XRD patterns (**Figure 5.1h**). During the Zn^{2+} insertion reaction at region II, the peak shifts to a lower angle with an increment less than 0.1°, suggesting that the increase of *d* spacing is no more than 0.2 Å, as well as the induced strain smaller than 1.6%. However, the theoretical value of the *d* spacing increment should be 0.88 Å, just as the radius size of the inserted Zn^{2+} ions, which can cause a severe strain over 6.9%. That means the pre-introduced out-of-plane compressive strain effectively offsets the strain and consequent lattice distortion brought by the Zn^{2+} insertion reaction. At the end and beginning of regions I and IV, respectively, the peaks of MnOOH are discovered at around 16.7° and 33.6°, related to the (020) and (040) facets of Groutite-phase MnOOH (JCPDS no. 12-0733). This is prominent evidence of the intercalation and deintercalation of H^+ ions.[302]

Another specific product, zinc sulfate hydroxide hydrate ($Zn_4SO_4(OH)_6 \cdot 0.5H_2O$, JCPDS no. 44-0674), is also detected at the end of the discharge process with locations of about 17.2° and 32.7°, corresponding to the $(0\bar{1}1)$ and (120) facets, respectively. They quickly shift to higher angles and vanish at the early stage of the charge process. As for the Zn^{2+} insertion product layered $Zn_xMn_2O_4$ for MnO_2, its peaks are overlapped with δ-phase MnO_2 at ~17.5° but can be identified at ~34.7°, due to the noticeable peak shifts within discharge/charge processes. Therefore, the Zn storage mechanism in MnO_2@rGO superlattice can be described as follow:

$$Mn^{IV}O_2 + H^+ + e^- \leftrightarrow Mn^{III}OOH$$

$$2Mn^{IV}O_2 + xZn^{2+} + 2xe^- \leftrightarrow Zn_xMn^{III,IV}{}_2O_4 \ (0 \leq x \leq 1)$$

$$4Zn^{2+} + 6OH^- + 4SO_4{}^{2-} + 0.5H_2O \leftrightarrow Zn_4SO_4(OH)_6 \cdot 0.5H_2O$$

However, the Zn storage mechanism in bare MnO_2 is slightly different. The peaks of $Zn_xMn_2O_4$ and $Zn_4SO_4(OH)_6 \cdot 0.5H_2O$ can be found in *in-situ* synchrotron XRD patterns (**Figure 5.18**), while no peak of MnOOH appears during discharge or charge process. Consequently, the structural degradation of bare MnO_2 can be deduced as **Schematic 5.17b** illustrated. H^+ ions can insert into the MnO_2 layers from the edges and directly attack the unprotected surface MnO_6 cells simultaneously. Even formed, MnOOH species will be fast eroded when exposed to the corrosion of surrounding H^+ ions, and then MnO_2 layers are irreversibly transformed into soluble Mn^{2+} ions and MnO_2 fragments. Differently, MnO_2 layers in MnO_2@rGO superlattice are sufficiently guarded benefited from the pre-introduced strain (**Schematic 5.17c**). When facing the H^+ insertion, the out-of-plane compressive strain can regulate the intercalation of H^+ ions principally from edge sites. Subsequently, MnOOH phases gradually grow towards central, bringing lattice mismatch at the interface between MnO_2 and MnOOH. Coincidentally, the Zn^{2+} insertion

formed layered $Zn_xMn_2O_4$ may induce the lattice distortion as well because of the poor resistance of Mn^{3+} ions to the "Jahn-Teller" effects.[303] Both situations will cause strains to spread from the edge inside, but pre-introduced in-plane tensile strain can effectively offset them and hence stabilize the superlattice structure within reversible cycles.

5.3.4 Zn^{2+} ion diffusion kinetics

Rate performance was first applied to investigate the kinetics of bare MnO_2 and MnO_2@rGO superlattice electrodes. In **Figure 5.19a**, MnO_2@rGO superlattice electrodes perform a better overall rate behavior than bare MnO_2 electrodes at various rates and deliver specific capacities of about 180 and 130 mAh g^{-1} at high rates of 5C and 10C, respectively, while the bare MnO_2 counterparts only have 100 and 50 mAh g^{-1}. This indicates the superior kinetics in the MnO_2@rGO superlattice. Cyclic voltammetry (CV) analysis was studied at different sweep rates to further explain the features of the two-step reaction kinetics related to H^+ and Zn^{2+} ions, as shown in **Figure 5.19b** and **Figure 5.20a**. There are two pairs of redox peaks clearly observed at the sweep rate of 0.1 mV s^{-1}, in terms of peak I/IV (1.39V/1.59V) and peak II/III (1.24V/1.54V), ascribed to the two-step insertion/extraction reactions of H^+ and Zn^{2+} ions, respectively. This is well-matched with the Zn storage mechanism in the *in-situ* synchrotron XRD results. With the increase of scan rates, the anodic peaks shift to low voltages; in reverse, the cathodic peaks shift to high voltages, suggesting that diffusion-limited and kinetic-controlled processes influence CV curves, especially peak currents. The relationship between peak currents (i) and sweep rates (v) are plotted in **Figure 5.19c** and **Figure 5.20b**. According to the equation of $i = av^b$ and the logarithmically transformed equation $\log i = \log a + b\log v$, the convertible parameter b is determined by the slope of the linear fitted log i-log v plot. The coefficient b varies from 0.5 to 1.0, where the minimum value 0.5 represents a solely diffusion-controlled process, while the maximum value of 1.0 suggests a totally

capacitive-dependent process. The *b* values of four peaks for MnO_2@rGO superlattice electrodes were calculated as 0.67, 0.52, 0.50, and 0.61, demonstrating a diffusion-dominated mechanism, especially for the Zn^{2+} storage process, while there is a slightly capacitive capacity contribution during H^+ insertion/extraction reactions. Bare MnO_2 electrodes have similar kinetics as MnO_2@rGO superlattice electrodes except for the H^+ extraction process, which inclines to be absolutely controlled by diffusion instead.

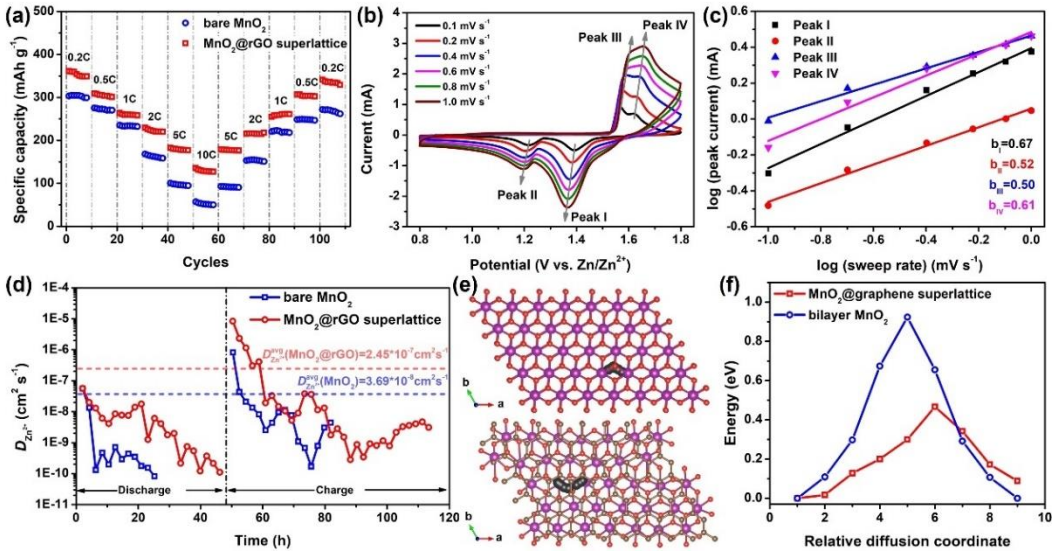

Figure 5.19 Zn^{2+} ion diffusion kinetics in aqueous zinc-ion batteries. (a) Rate performance of bare MnO_2 and MnO_2@rGO superlattice electrodes. (b) CV curves of MnO_2@rGO superlattice electrodes at various sweep rates and (c) the plot of related peak currents versus sweep rates. (d) The Zn^{2+} diffusion coefficients of bare MnO_2 and MnO_2@rGO superlattice electrodes, calculated from GITT results, with dash lines of average values. (e) Zn^{2+} diffusion pathways in bilayer MnO_2 nanosheets and MnO_2@graphene superlattice and (f) the corresponding diffusion energy.

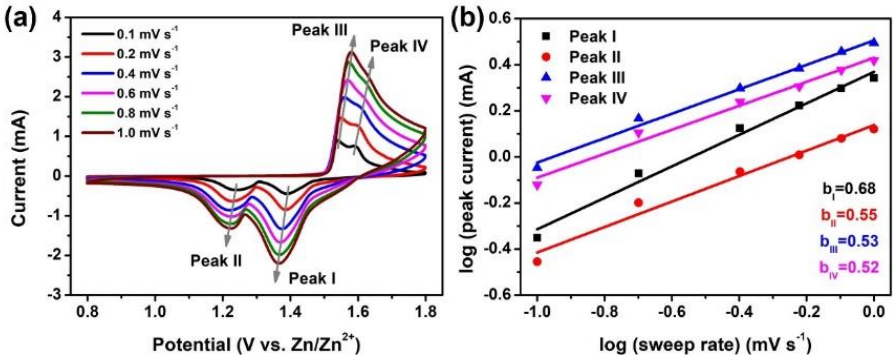

Figure 5.20 (a) CV curves of bare MnO_2 electrodes at various sweep rates and (b) the plot of related peak currents versus sweep rates.

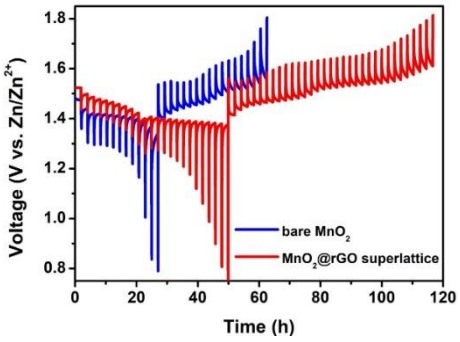

Figure 5.21 GITT curves of bare MnO_2 and MnO_2@rGO superlattice electrodes.

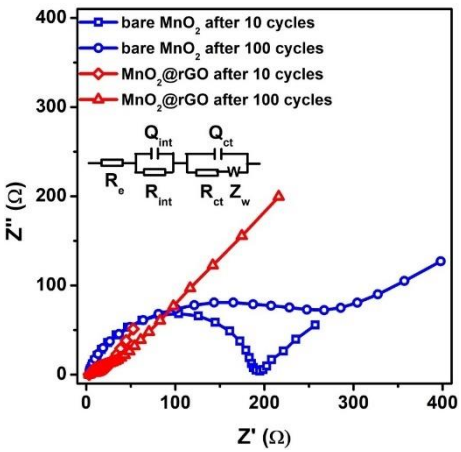

Figure 5.22 EIS spectra of bare MnO_2 and MnO_2@rGO superlattice electrodes after 10 and 100 cycles.

The quantification of diffusion coefficient was achieved by galvanostatic intermittent titration technique (GITT, **Figure 5.21**). The calculated Zn^{2+} diffusion coefficients (D_{Zn}^{2+})

of bare MnO_2 and MnO_2@rGO superlattice electrodes were plotted in **Figure 5.19d**. During the discharge process, the D_{Zn}^{2+} at the first plateaus represent the intercalation of protons and thus show higher values than the D_{Zn}^{2+} at the second plateaus denoting the larger-radius Zn^{2+} insertion. Whereas the situation reverses in the charge process, the possible reason should be the higher interaction between proton and manganese oxide species. Nevertheless, MnO_2@rGO superlattice electrodes exhibit superior D_{Zn}^{2+} values at every stage than bare MnO_2 electrodes. The average D_{Zn}^{2+} of MnO_2@rGO superlattice electrodes is 2.45×10^{-7} cm^2 s^{-1}, nearly one order of magnitude higher than the counterpart. Electrochemical impedance spectra (EIS, **Figure 5.22**) also demonstrated close results. The Nyquist plots of both electrodes can be fitted by the inset equivalent circuits, where the resistor element R_{ct} symbolize the bulk resistance of porous electrodes. The simulated results illustrate that MnO_2@rGO superlattice electrodes have a much lower R_{ct} (15.9 Ω) than bare MnO_2 electrodes (132.9 Ω) after 10 full cycles. Even after 100 cycles, the R_{ct} value of the former just increases to 30.7 Ω, versus 195.4 Ω for the later. This is beneficial from the excellent electronic conductivity of rGO framework. Besides, the slopes of the oblique Warburg regions for MnO_2@rGO superlattice electrodes are larger than bare MnO_2 counterpart and keep stable within cycles, indicating the superior diffusion kinetics.

Furthermore, DFT calculations were conducted to understand the Zn atom diffusion behavior in the strain-reinforced superlattice structure. The Zn diffusion pathway in bilayer MnO_2 nanosheets and one MnO_2@graphene superlattice unit were displayed in **Figure 5.19e**. The corresponding diffusion energy barriers were also calculated and shown in **Figure 5.19f**. Compared with bilayer MnO_2, MnO_2@graphene superlattice has a half lower Zn diffusion energy barrier, confirming the faster kinetics in the strain-reinforced superlattice.

5.4. Conclusions

In summary, the pre-introduction of strain was achieved by constructing a superlattice structure via electrostatic self-assembly of unilamellar MnO_2 and positive-charged rGO nanosheets. Within the superlattice structure, the strong chemical bonding effect between MnO_2 and rGO induced noticeable lattice distortions in δ-phase MnO_2 associated with the "Jahn-Teller" effect and consequently formed in-plane tensile and out-of-plane compressive stains on MnO_2 layers. During cycling, two kinds of strains synergistically overcame H^+ corrosion towards Mn sites in MnO_6 octahedra, and the strain brought by H^+ and Zn^{2+} co-insertion induced phase transformation, which effectively suppressed the dissolution of Mn and improved the structural stability of δ-MnO_2. Hence, the MnO_2@rGO superlattice exhibited excellent cycling stability over 700 cycles at 1C with capacity retention of 91.2% and a high reversible capacity of 165 mAh g^{-1} over 5000 cycles at 5C, under the shield of pre-introduced strain. Kinetics investigation demonstrated that the pre-introduction of strain also had a particular enhancement to ion diffusion. In this respect, it is a novel and promising strategy of pre-introducing strain into electrode materials to stabilize the construction, especially to transition metal oxides with a low resistance to lattice distortion, like Mn-based and V-based oxides when applied in aqueous zinc-ion batteries.

Chapter 6 Summary and Perspective

6.1 Summary

In summary, we presented three works about 2D material-based heterostructures in this doctoral thesis, where the dimensionalities of building blocks varied from 0D Sb single atoms and quantum dots, 1D N-doped carbon encapsulated Sb_2Se_3 nanorods, 2D δ-phase MnO_2 nanosheets coupled with 2D counterparts including MXene and rGO nanosheets. Two general fabrication strategies, in terms of *in-situ* growth processing and liquid-phase self-assembly, were employed to obtain these three heterostructures, namely 0D-2D Sb single atoms and quantum dots co-decorated MXene-based aerogel, 1D-2D N-doped carbon encapsulation and 2D confinement of rGO nanosheets co-modified Sb_2Se_3 nanorods, and 2D-2D MnO_2@rGO superlattice. As for the functional improvements in rechargeable batteries, in 0D-2D heterostructures, the atomic distribution of 0D Sb species facilitates both charge transport and potassium storage, and meanwhile GO-assisted MXene 2D substrates provide fast electron pathway, increase the contact with electrolyte, and accommodate volume change to stabilize heterostructure in potassium-ion batteries. As a result, the obtained Sb SQ@MA heterostructure anodes delivered a high reversible capacity of 521 mAh g^{-1} at 0.1 A g^{-1} and kept high capacity retention over 94% at 1 A g^{-1} even after 1000 cycles. As for 1D-2D heterostructures, the synergistic effect of encapsulation and confinement ultimately suppress the volumetric expansion of Sb_2Se_3 nanorods during potassiation process, where the NC coating layers help to protect Sb_2Se_3 nanorods from pulverization and flexible rGO nanosheets maintain the overall structural integrity. This achieved a high reversible specific capacity of 590 mA h g^{-1} and good cycling stability up to 350 cycles. Moreover, the thorough investigation revealed the potassium storage mechanism in Sb_2Se_3 as a two-step conversion reaction with a

multi-step alloying reaction. 2D-2D heterostructures successfully minimized Mn dissolution of δ-MnO_2 during the H^+/Zn^{2+} co-insertion reaction processes in aqueous zinc-ion batteries benefited from the pre-introduced strains after the construction. Therefore, MnO_2@rGO superlattice electrodes exhibited stable cycling over 700 cycles at 1C with capacity retention of 91.2% and a high reversible capacity of 165 mAh g^{-1} after 5000 cycles at 5C. Furthermore, the origination and features of pre-introduce strains were exhaustively studied that strong chemical bonding between MnO_2 and rGO generated lattice distortion and thus formed in-plane and out-of-plane distributed tensile and compressive strains on MnO_2 sheets, respectively. The functional effects during cycling were also detailly clarified as the pre-introduced tensile and compressive strains synergistically offset the H^+/Zn^{2+} co-insertion brought adverse stress.

6.2 Future perspective

So far, numerous studies have engaged in understanding the functional roles of 2D material-based heterostructures at atomic levels *via* advanced experimental techniques and theoretical calculations. Nevertheless, challenges remain, like how to maximize these advances and integrate them into one electrode structure. Therefore, we proposed some prospective research directions, which might further facilitate the development of 2D material-based heterostructures for practical energy storage devices with higher energy and power density, as well as longer lifetimes.

(1) *Elucidating exact functions of 2D material-based heterostructures in electrochemical reactions*. As we summarized in the last section, the multi-functionalities of 2D material-based heterostructures have been recognized in a great number of publications. Among most studies, they claimed that the outstanding electrochemical performances of heterostructures could be assigned to synergistic effects of

heterostructures, including enhanced electronic and ionic conductivity, more accessible active sites, and improved mechanical properties. However, to better understand the functions of specific heterostructures and offer instructions for precise construction of the desired heterostructures, advanced *operando* and *ex-situ* characterization techniques should be applied to unravel the accurate roles and structural transformation of heterostructures in the electrochemical processes.

(2) *Increasing electrochemically active sites while maintaining structural stability.* Pursuing higher capacity is a continuous target in the energy storage field, and it is why heterostructures based on conversion- and alloying-type 2D materials, like phosphorene, tin/antimony sulfides or selenides, are favorable for alkali-ions storage. Although building heterostructures with complementary ingredients can confine the structural change of these high-capacity materials, it inevitably causes volume expansion and deteriorates long-term cycling stability of devices. Therefore, we should put in more effort to explore novel strategies for maximizing active sites of 2D materials-based heterostructures without sacrificing the structural stability. A good example is introducing molecular-level surface redox sites to the 2D phosphorene/graphene heterostructure, and the capacitors using the said materials presented a significantly improved capacitance and cycling performance owing to the boosted pseudocapacitive mechanism.[304]

(3) *Considering mechanical effects from microscopic level to electrodes in devices.* Except for thermodynamic and kinetic properties, mechanical effect in 2D material-based heterostructures, such as grain stress in crystals and electrode strain, is another important factor influencing the electrochemical behaviors, especially cycling stability of practical rechargeable batteries.[118,295,305,306] It is of great significance in developing advanced

experimental techniques coupled with theoretical simulations to understand mechanical effects, which would instruct the design from materials to electrode configurations.

(4) *Balancing heterointerfaces with other factors that influencing the electrochemical performance.* Heterointerfaces are the core of a heterostructure, which can boost the electronic and ionic charge transfer because of the introduction of the localized electric field. In this case, the 2D-2D heterostructures with maximized heterointerfaces should possess fast reaction kinetics and contribute to the high-rate performance. However, most of these stacked 2D-2D heterostructures present poorer rate performance compared to other-type mixed-dimensional heterostructures, which can be ascribed to the lower ion-mobility within electrolytes.[307] A rational heterostructure design is expected to consider both the solid-state diffusion and reaction kinetics (inherent characteristics of the heterostructure electrode) and electrode-electrolyte interactions.

(5) *From assumptions, theories, and experiments to practices.* The development of 2D material-based heterostructures is nearly parallel with the progress of 2D materials. As a result, the bottlenecks in 2D materials limit the growth of the derived 2D material-based heterostructure, such as their complicated synthesis process, relatively low yields, uncontrollable lateral sizes, metastable properties, *etc.* For pushing 2D material-based heterostructures into practical applications, the inferior cost-effective performance reduces their competitive capability compared with traditional or rising electrode materials, especially anode materials, like graphite, Si/C composites, hard carbonaceous materials, and so on. Therefore, the commercialization of 2D materials is the base stone of the industrial practice for 2D material-based heterostructures, although 2D materials are still very young since the discovery of graphene. After that, the preparation engineering of 2D material-based heterostructures should be simplified and modified in

priority to meet large-scale production requirements, according to the present fundamental investigations.

REFERENCES

[1] D. Larcher, J. M. Tarascon, *Nature Chemistry* **2014**, *7*, 19.

[2] B. Dunn, H. Kamath, J.-M. Tarascon, *Science* **2011**, *334*, 928.

[3] J. W. Choi, D. Aurbach, *Nature Review Materials* **2016**, *1*, 16013.

[4] P. G. Bruce, S. A. Freunberger, L. J. Hardwick, J. M. Tarascon, *Nature Materials* **2012**, *11*, 19.

[5] H. Gao, X. Guo, S. Wang, F. Zhang, H. Liu, G. Wang, *EcoMat* **2020**, *2*,

[6] M. Zhong, L. Kong, K. Zhao, Y.-H. Zhang, N. Li, X.-H. Bu, *Advanced Science* **2021**, *8*, 2001980.

[7] G. Xu, P. Nie, H. Dou, B. Ding, L. Li, X. Zhang, *Mater. Today* **2017**, *20*, 191.

[8] K. S. Novoselov, A. Mishchenko, A. Carvalho, A. H. Castro Neto, *Science* **2016**, *353*, aac9439.

[9] Y. Ding, Y. Li, M. Wu, H. Zhao, Q. Li, Z.-S. Wu, *Energy Storage Materials* **2020**, *31*, 470.

[10] Q. Yun, L. Li, Z. Hu, Q. Lu, B. Chen, H. Zhang, *Advanced Materials* **2020**, *32*,

[11] M. Jana, R. Xu, X.-B. Cheng, J. S. Yeon, J. M. Park, J.-Q. Huang, Q. Zhang, H. S. Park, *Energy & Environmental Science* **2020**, *13*, 1049.

[12] X. Wang, Q. Weng, Y. Yang, Y. Bando, D. Golberg, *Chemical Society Reviews* **2016**, *45*, 4042.

[13] Y. Liu, C. Zeng, J. Yu, J. Zhong, B. Li, Z. Zhang, Z. Liu, Z. M. Wang, A. Pan, X. Duan, *Chem Soc Rev* **2021**,

[14] Y. Liu, S. Zhang, J. He, Z. M. Wang, Z. Liu, *Nano-Micro Letters* **2019**, *11*,

[15] E. Pomerantseva, Y. Gogotsi, *Nature Energy* **2017**, *2*, 17089.

[16] C. R. Dean, A. F. Young, I. Meric, C. Lee, L. Wang, S. Sorgenfrei, K. Watanabe, T. Taniguchi, P. Kim, K. L. Shepard, J. Hone, *Nature Nanotechnology* **2010**, *5*, 722.

[17] Y. Liu, Y. Gao, S. Zhang, J. He, J. Yu, Z. Liu, *Nano Research* **2019**, *12*, 2695.

[18] J. Yu, X. Kuang, Y. Gao, Y. Wang, K. Chen, Z. Ding, J. Liu, C. Cong, J. He, Z. Liu, Y. Liu, *Nano Lett* **2020**, *20*, 1172.

[19] J. Yu, X. Kuang, J. Li, J. Zhong, C. Zeng, L. Cao, Z. Liu, Z. Zeng, Z. Luo, T. He, A. Pan, Y. Liu, *Nat Commun* **2021**, *12*, 1083.

[20] J. Zhong, J. Yu, L. Cao, C. Zeng, J. Ding, C. Cong, Z. Liu, Y. Liu, *Nano Research* **2020**, *13*, 1780.

[21] L. Wang, I. Meric, P. Y. Huang, Q. Gao, Y. Gao, H. Tran, T. Taniguchi, K. Watanabe, L. M. Campos, D. A. Muller, J. Guo, P. Kim, J. Hone, K. L. Shepard, C. R. Dean, *Science* **2013**, *342*, 614.

[22] X. Xie, M.-Q. Zhao, B. Anasori, K. Maleski, C. E. Ren, J. Li, B. W. Byles, E. Pomerantseva, G. Wang, Y. Gogotsi, *Nano Energy* **2016**, *26*, 513.

[23] Z. Zhang, P. Chen, X. Duan, K. Zang, J. Luo, X. Duan, *Science* **2017**, *357*, 788.

[24] M.-Q. Zhao, N. Trainor, C. E. Ren, M. Torelli, B. Anasori, Y. Gogotsi, *Advanced Materials Technologies* **2019**, *4*, 1800639.

[25] M.-Q. Zhao, C. E. Ren, Z. Ling, M. R. Lukatskaya, C. Zhang, K. L. Van Aken, M. W. Barsoum, Y. Gogotsi, *Advanced Materials* **2015**, *27*, 339.

[26] J. Duan, S. Chen, M. Jaroniec, S. Z. Qiao, *ACS Nano* **2015**, *9*, 931.

[27] F. Zhang, X. Guo, P. Xiong, J. Zhang, J. Song, K. Yan, X. Gao, H. Liu, G. Wang, *Advanced Energy Materials* **2020**, *10*, 2000446.

[28] X. Zhang, Z. Lai, Q. Ma, H. Zhang, *Chemical Society Reviews* **2018**, *47*, 3301.

[29] M. Kumar, Y. Ando, *Journal of Nanoscience and Nanotechnology* **2010**, *10*, 3739.

[30] A. Ismach, C. Druzgalski, S. Penwell, A. Schwartzberg, M. Zheng, A. Javey, J. Bokor, Y. Zhang, *Nano Letters* **2010**, *10*, 1542.

[31] X. Li, M.-W. Lin, J. Lin, B. Huang, A. A. Puretzky, C. Ma, K. Wang, W. Zhou, S. T. Pantelides, M. Chi, I. Kravchenko, J. Fowlkes, C. M. Rouleau, D. B. Geohegan, K. Xiao, *Science Advances* **2016**, *2*, e1501882.

[32] Y. Gong, J. Lin, X. Wang, G. Shi, S. Lei, Z. Lin, X. Zou, G. Ye, R. Vajtai, B. I. Yakobson, H. Terrones, M. Terrones, Beng K. Tay, J. Lou, S. T. Pantelides, Z. Liu, W. Zhou, P. M. Ajayan, *Nature Materials* **2014**, *13*, 1135.

[33] T. Zhang, B. Jiang, Z. Xu, R. G. Mendes, Y. Xiao, L. Chen, L. Fang, T. Gemming, S. Chen, M. H. Rümmeli, L. Fu, *Nature Communications* **2016**, *7*, 13911.

[34] J. Shi, M. Liu, J. Wen, X. Ren, X. Zhou, Q. Ji, D. Ma, Y. Zhang, C. Jin, H. Chen, S. Deng, N. Xu, Z. Liu, Y. Zhang, *Advanced Materials* **2015**, *27*, 7086.

[35] H. G. Kim, H.-B.-R. Lee, *Chemistry of Materials* **2017**, *29*, 3809.

[36] B. Ahmed, D. H. Anjum, Y. Gogotsi, H. N. Alshareef, *Nano Energy* **2017**, *34*, 249.

[37] J. Azadmanjiri, V. K. Srivastava, P. Kumar, Z. Sofer, J. Min, J. Gong, *Applied Materials Today* **2020**, *19*,

[38] S. Zhao, H.-B. Zhang, J.-Q. Luo, Q.-W. Wang, B. Xu, S. Hong, Z.-Z. Yu, *ACS Nano* **2018**, *12*, 11193.

[39] X. Wu, Z. Wang, M. Yu, L. Xiu, J. Qiu, *Advanced Materials* **2017**, *29*, 1607017.

[40] M. Yu, S. Zhou, Z. Wang, J. Zhao, J. Qiu, *Nano Energy* **2018**, *44*, 181.

[41] M. Yu, Z. Wang, J. Liu, F. Sun, P. Yang, J. Qiu, *Nano Energy* **2019**, *63*, 103880.

[42] T. Jiang, F. Bu, X. Feng, I. Shakir, G. Hao, Y. Xu, *ACS Nano* **2017**, *11*, 5140.

[43] J. Cui, S. Yao, Z. Lu, J.-Q. Huang, W. G. Chong, F. Ciucci, J.-K. Kim, *Advanced Energy Materials* **2018**, *8*, 1702488.

[44] Z. Wang, H. Gao, Q. Zhang, Y. Liu, J. Chen, Z. Guo, *Small* **2019**, *15*, e1803858.

[45] Y. Deng, T. Shang, Z. Wu, Y. Tao, C. Luo, J. Liang, D. Han, R. Lyu, C. Qi, W. Lv, F. Kang, Q.-H. Yang, *Advanced Materials* **2019**, *31*, 1902432.

[46] A. Khan, J. Azadmanjiri, B. Wu, L. Liping, Z. Sofer, J. Min, *Advanced Energy Materials* **2021**, *11*,

[47] X. Wen, J. Min, H. Tan, D. Gao, X. Chen, K. Szymańska, B. Zielińska, E. Mijowska, T. Tang, *Composites Part A: Applied Science and Manufacturing* **2020**, *129*,

[48] C. Song, L. Hao, B. Zhang, Z. Dong, Q. Tang, J. Min, Q. Zhao, R. Niu, J. Gong, T. Tang, *Science China Materials* **2020**, *63*, 779.

[49] X. Liang, A. Garsuch, L. F. Nazar, *Angewandte Chemie International Edition* **2015**, *54*, 3907.

[50] X. Hui, R. Zhao, P. Zhang, C. Li, C. Wang, L. Yin, *Advanced Energy Materials* **2019**, *9*, 1901065.

[51] S. Wang, F. Cao, Y. Li, Z. Zhang, D. Zhou, Y. Yang, Z. Tang, *Adv Sci (Weinh)* **2019**, *6*, 1900028.

[52] C. Tang, Q. Zhang, M.-Q. Zhao, J.-Q. Huang, X.-B. Cheng, G.-L. Tian, H.-J. Peng, F. Wei, *Advanced Materials* **2014**, *26*, 6100.

[53] X. Guo, J. Zhang, J. Song, W. Wu, H. Liu, G. Wang, *Energy Storage Materials* **2018**, *14*, 306.

[54] W. Du, Z. Ahmed, Q. Wang, C. Yu, Z. Feng, G. Li, M. Zhang, C. Zhou, R. Senegor, C. Y. Yang, *2D Materials* **2019**, *6*,

[55] W.-H. Ryu, H. Wilson, S. Sohn, J. Li, X. Tong, E. Shaulsky, J. Schroers, M. Elimelech, A. D. Taylor, *ACS Nano* **2016**, *10*, 3257.

[56] N. Wang, J. Yue, L. Chen, Y. Qian, J. Yang, *ACS Applied Materials & Interfaces* **2015**, *7*, 10348.

[57] Y.-T. Liu, P. Zhang, N. Sun, B. Anasori, Q.-Z. Zhu, H. Liu, Y. Gogotsi, B. Xu, *Advanced Materials* **2018**, *30*, 1707334.

[58] S. B. Ambade, R. B. Ambade, W. Eom, S. H. Noh, S. H. Kim, T. H. Han, *Advanced Materials Interfaces* **2018**, *5*, 1801361.

[59] S. J. Wang, P. Xiong, X. Guo, J. Q. Zhang, X. C. Gao, F. Zhang, X. Tang, P. H. L. Notten, G. X. Wang, *Advanced Functional Materials* **2020**, *30*, 2001588.

[60] M.-L. Tsai, M.-Y. Li, J. R. D. Retamal, K.-T. Lam, Y.-C. Lin, K. Suenaga, L.-J. Chen, G. Liang, L.-J. Li, J.-H. He, *Advanced Materials* **2017**, *29*, 1701168.

[61] G. Wang, J. Zhang, S. Yang, F. Wang, X. Zhuang, K. Müllen, X. Feng, *Advanced Energy Materials* **2018**, *8*, 1702254.

[62] C. Chen, X. Xie, B. Anasori, A. Sarycheva, T. Makaryan, M. Zhao, P. Urbankowski, L. Miao, J. Jiang, Y. Gogotsi, *Angewandte Chemie International Edition* **2018**, *57*, 1846.

[63] C. H. Naylor, W. M. Parkin, Z. Gao, J. Berry, S. Zhou, Q. Zhang, J. B. McClimon, L. Z. Tan, C. E. Kehayias, M.-Q. Zhao, R. S. Gona, R. W. Carpick, A. M. Rappe, D. J. Srolovitz, M. Drndic, A. T. C. Johnson, *ACS Nano* **2017**, *11*, 8619.

[64] X. Wang, H. Li, H. Li, S. Lin, W. Ding, X. Zhu, Z. Sheng, H. Wang, X. Zhu, Y. Sun, *Advanced Functional Materials* **2020**, *30*, 0190302.

[65] S. Liu, Y. Liu, W. Lei, X. Zhou, K. Xu, Q. Qiao, W.-H. Zhang, *Journal of Materials Chemistry A* **2018**, *6*, 20267.

[66] J. Min, X. Xu, J. J. Koh, J. Gong, X. Chen, J. Azadmanjiri, F. Zhang, X. Wen, C. He, *ACS Applied Energy Materials* **2021**, *4*, 3317.

[67] B. Chen, Y. Meng, F. He, E. Liu, C. Shi, C. He, L. Ma, Q. Li, J. Li, N. Zhao, *Nano Energy* **2017**, *41*, 154.

[68] J. Min, S. Zhang, J. Li, R. Klingeler, X. Wen, X. Chen, X. Zhao, T. Tang, E. Mijowska, *Waste Manag* **2019**, *85*, 333.

[69] P. Xiong, R. Ma, N. Sakai, L. Nurdiwijayanto, T. Sasaki, *ACS Energy Letters* **2018**, *3*, 997.

[70] P. Xiong, X. Zhang, F. Zhang, D. Yi, J. Zhang, B. Sun, H. Tian, D. Shanmukaraj, T. Rojo, M. Armand, R. Ma, T. Sasaki, G. Wang, *ACS Nano* **2018**, *12*, 12337.

[71] P. Xiong, X. Zhang, H. Wan, S. Wang, Y. Zhao, J. Zhang, D. Zhou, W. Gao, R. Ma, T. Sasaki, G. Wang, *Nano Letters* **2019**, *19*, 4518.

[72] P. Xiong, F. Zhang, X. Zhang, S. Wang, H. Liu, B. Sun, J. Zhang, Y. Sun, R. Ma, Y. Bando, C. Zhou, Z. Liu, T. Sasaki, G. Wang, *Nature Communications* **2020**, *11*, 3297.

[73] J. H. Peng, X. Z. Chen, W. J. Ong, X. J. Zhao, N. Li, *Chem* **2019**, *5*, 18.

[74] Z. Dai, L. Liu, Z. Zhang, *Advanced Materials* **2019**, *31*, 1805417.

[75] M. Alhabeb, K. Maleski, B. Anasori, P. Lelyukh, L. Clark, S. Sin, Y. Gogotsi, *Chemistry of Materials* **2017**, *29*, 7633.

[76] J. Kim, L. J. Cote, F. Kim, W. Yuan, K. R. Shull, J. X. Huang, *Journal of the American Chemical Society* **2010**, *132*, 8180.

[77] V. Kamysbayev, A. S. Filatov, H. Hu, X. Rui, F. Lagunas, D. Wang, R. F. Klie, D. V. Talapin, *Science* **2020**, *369*, 979.

[78] Y. Xie, Y. Dall'Agnese, M. Naguib, Y. Gogotsi, M. W. Barsoum, H. L. Zhuang, P. R. C. Kent, *ACS Nano* **2014**, *8*, 9606.

[79] C. Wang, S. Chen, L. Song, *Advanced Functional Materials* **2020**, *30*, 2000869.

[80] J. Li, X. Yuan, C. Lin, Y. Yang, L. Xu, X. Du, J. Xie, J. Lin, J. Sun, *Advanced Energy Materials* **2017**, *7*, 1602725.

[81] X. Guo, W. Zhang, J. Zhang, D. Zhou, X. Tang, X. Xu, B. Li, H. Liu, G. Wang, *ACS Nano* **2020**, *14*, 3651.

[82] X. Xie, C. Chen, N. Zhang, Z.-R. Tang, J. Jiang, Y.-J. Xu, *Nature Sustainability* **2019**, *2*, 856.

[83] H. Huang, J. Cui, G. Liu, R. Bi, L. Zhang, *ACS Nano* **2019**, *13*, 3448.

[84] X. Tang, D. Zhou, P. Li, X. Guo, B. Sun, H. Liu, K. Yan, Y. Gogotsi, G. Wang, *Advanced Materials* **2020**, *32*, 1906739.

[85] X. H. Wu, Z. Y. Wang, M. Z. Yu, L. Y. Xiu, J. S. Qiu, *Advanced Materials* **2017**, *29*,

[86] Q. Ren, N. Qin, B. Liu, Y. Yao, X. Zhao, Z. Deng, Y. Li, Y. Dong, D. Qian, B.-L. Su, W. Zhang, H.-E. Wang, *Journal of Materials Chemistry A* **2020**, *8*, 3450.

[87] X. Sun, Z. Wang, *Applied Surface Science* **2018**, *455*, 911.

[88] J. Zhang, Y. Zhao, X. Guo, C. Chen, C.-L. Dong, R.-S. Liu, C.-P. Han, Y. Li, Y. Gogotsi, G. Wang, *Nature Catalysis* **2018**, *1*, 985.

[89] Y. Wen, T. E. Rufford, X. Chen, N. Li, M. Lyu, L. Dai, L. Wang, *Nano Energy* **2017**, *38*, 368.

[90] Y. Zhu, W. Peng, Y. Li, G. Zhang, F. Zhang, X. Fan, *Journal of Materials Chemistry A* **2019**, *7*, 23577.

[91] X. Tang, D. Zhou, P. Li, X. Guo, B. Sun, H. Liu, K. Yan, Y. Gogotsi, G. Wang, *Adv Mater* **2020**, *32*, e1906739.

[92] Z.-Z. Luo, Y. Zhang, C. Zhang, H. T. Tan, Z. Li, A. Abutaha, X.-L. Wu, Q. Xiong, K. A. Khor, K. Hippalgaonkar, J. Xu, H. H. Hng, Q. Yan, *Advanced Energy Materials* **2017**, *7*,

[93] T. R. Jow, S. A. Delp, J. L. Allen, J.-P. Jones, M. C. Smart, *Journal of The Electrochemical Society* **2018**, *165*, A361.

[94] D. K. Bediako, M. Rezaee, H. Yoo, D. T. Larson, S. Y. F. Zhao, T. Taniguchi, K. Watanabe, T. L. Brower-Thomas, E. Kaxiras, P. Kim, *Nature* **2018**, *558*, 425.

[95] X. Shao, K. Wang, R. Pang, X. Shi, *The Journal of Physical Chemistry C* **2015**, *119*, 25860.

[96] L. Su, N. Zhao, C. Shi, L. Ma, E. Liu, *Electrochimica Acta* **2018**, *285*, 309.

[97] F. Gong, Z. Ding, Y. Fang, C. J. Tong, D. Xia, Y. Lv, B. Wang, D. V. Papavassiliou, J. Liao, M. Wu, *ACS Appl Mater Interfaces* **2018**, *10*, 14614.

[98] J. Ma, J. Fu, M. Niu, R. Quhe, *Carbon* **2019**, *147*, 357.

[99] H. W. Lee, H. Jung, B. C. Yeo, D. Kim, S. S. Han, *The Journal of Physical Chemistry C* **2018**, *122*, 20653.

[100] Z. Wang, K. Dong, D. Wang, S. Luo, Y. Liu, Q. Wang, Y. Zhang, A. Hao, C. Shi, N. Zhao, *Journal of Materials Chemistry A* **2019**, *7*, 14309.

[101] D. Adekoya, S. Zhang, M. Hankel, *ACS Appl Mater Interfaces* **2020**, *12*, 25875.

[102] P. Ruan, X. Xu, X. Gao, J. Feng, L. Yu, Y. Cai, X. Gao, W. Shi, F. Wu, W. Liu, X. Zang, F. Ma, X. Cao, *Sustainable Materials and Technologies* **2021**, *28*,

[103] D.-X. Song, L. Xie, Y.-F. Zhang, Y. Lu, M. An, W.-G. Ma, X. Zhang, *ACS Applied Energy Materials* **2020**, *3*, 7699.

[104] J. Li, Q. Peng, J. Zhou, Z. Sun, *The Journal of Physical Chemistry C* **2019**, *123*, 11493.

[105] C. He, J. H. Zhang, W. X. Zhang, T. T. Li, *The Journal of Physical Chemistry C* **2019**, *123*, 5157.

[106] H. Liu, Z. Huang, G. Wu, Y. Wu, G. Yuan, C. He, X. Qi, J. Zhong, *Journal of Materials Chemistry A* **2018**, *6*, 17040.

[107] D. Sun, K. Liu, J. Hu, J. Zhou, *Small* **2021**, *17*, e2006374.

[108] Y. Zheng, T. Zhou, C. Zhang, J. Mao, H. Liu, Z. Guo, *Angew Chem Int Ed Engl* **2016**, *55*, 3408.

[109] C. Yang, X. Liang, X. Ou, Q. Zhang, H.-S. Zheng, F. Zheng, J.-H. Wang, K. Huang, M. Liu, *Advanced Functional Materials* **2019**, *29*,

[110] S. Wang, S. Liu, X. Li, C. Li, R. Zang, Z. Man, Y. Wu, P. Li, G. Wang, *Chemistry* **2018**, *24*, 3873.

[111] F. Chen, D. Shi, M. Yang, H. Jiang, Y. Shao, S. Wang, B. Zhang, J. Shen, Y. Wu, X. Hao, *Advanced Functional Materials* **2020**,

[112] L. Fang, Z. Lan, W. Guan, P. Zhou, N. Bahlawane, W. Sun, Y. Lu, C. Liang, M. Yan, Y. Jiang, *Energy Storage Materials* **2019**, *18*, 107.

[113] C. Li, S. Dong, R. Tang, X. Ge, Z. Zhang, C. Wang, Y. Lu, L. Yin, *Energy & Environmental Science* **2018**, *11*, 3201.

[114] X. Xie, S. Wang, K. Kretschmer, G. Wang, *J Colloid Interface Sci* **2017**, *499*, 17.

[115] P. Xiong, R. Ma, G. Wang, T. Sasaki, *Energy Storage Materials* **2019**, *19*, 281.

[116] J. Nan, X. Guo, J. Xiao, X. Li, W. Chen, W. Wu, H. Liu, Y. Wang, M. Wu, G. Wang, *Small* **2019**, e1902085.

[117] J. Yu, M. Zhou, M. Yang, Q. Yang, Z. Zhang, Y. Zhang, *ACS Applied Energy Materials* **2020**, *3*, 11699.

[118] P. Xiong, F. Zhang, X. Zhang, S. Wang, H. Liu, B. Sun, J. Zhang, Y. Sun, R. Ma, Y. Bando, C. Zhou, Z. Liu, T. Sasaki, G. Wang, *Nat Commun* **2020**, *11*, 3297.

[119] S. X. Hongchang Jin, Chenghao Chuang, Wangda Li, Haiyun Wang, Jian Zhu, Huanyu Xie, Taiming Zhang, Yangyang Wan, Zhikai Qi, Wensheng Yan, Ying-Rui Lu, Ting-Shan Chan, Xiaojun Wu, John B. Goodenough, Hengxing Ji, Xiangfeng Duan, *Science* **2020**, *370*, 192.

[120] T. Wang, D. Legut, Y. Fan, J. Qin, X. Li, Q. Zhang, *Nano Lett* **2020**, *20*, 6199.

[121] X. Xie, Z. Ao, D. Su, J. Zhang, G. Wang, *Advanced Functional Materials* **2015**, *25*, 1393.

[122] R. Zhao, Z. Qian, Z. Liu, D. Zhao, X. Hui, G. Jiang, C. Wang, L. Yin, *Nano Energy* **2019**, *65*,

[123] M. Ma, S. Zhang, Y. Yao, H. Wang, H. Huang, R. Xu, J. Wang, X. Zhou, W. Yang, Z. Peng, X. Wu, Y. Hou, Y. Yu, *Adv Mater* **2020**, *32*, e2000958.

[124] J. Yang, J. Luo, Y. Kuang, Y. He, P. Wen, L. Xiong, X. Wang, Z. Yang, *ACS Appl Mater Interfaces* **2021**, *13*, 2072.

[125] Y. Lee, J.-Y. Yoon, D. Scullion, J. Jang, E. J. G. Santos, H. Y. Jeong, K. Kim, *Journal of Physics D: Applied Physics* **2017**, *50*,

[126] J. Pang, A. Bachmatiuk, Y. Yin, B. Trzebicka, L. Zhao, L. Fu, R. G. Mendes, T. Gemming, Z. Liu, M. H. Rummeli, *Advanced Energy Materials* **2018**, *8*,

[127] Y. Shi, Z. Yi, Y. Kuang, H. Guo, Y. Li, C. Liu, Z. Lu, *Chem Commun (Camb)* **2020**, *56*, 11613.

[128] F. Zhou, L. Ouyang, J. Liu, X.-S. Yang, M. Zhu, *Journal of Power Sources* **2020**, *449*,

[129] X. Ou, C. Yang, X. Xiong, F. Zheng, Q. Pan, C. Jin, M. Liu, K. Huang, *Advanced Functional Materials* **2017**, *27*,

[130] X. Tang, H. Liu, X. Guo, S. Wang, W. Wu, A. K. Mondal, C. Wang, G. Wang, *Materials Chemistry Frontiers* **2018**, *2*, 1811.

[131] X. Guo, X. Xie, S. Choi, Y. Zhao, H. Liu, C. Wang, S. Chang, G. Wang, *Journal of Materials Chemistry A* **2017**, *5*, 12445.

[132] A. Gentile, C. Ferrara, S. Tosoni, M. Balordi, S. Marchionna, F. Cernuschi, M. H. Kim, H. W. Lee, R. Ruffo, *Small Methods* **2020**, *4*,

[133] C. Wu, G. Zhao, X. Yu, C. Liu, P. Lyu, G. Maurin, S. Le, K. Sun, N. Zhang, *Chemical Engineering Journal* **2021**, *412*,

[134] Martin Ebner, Federica Marone, Marco Stampanoni, V. Wood, *Science* **2013**, *342*, 716.

[135] Q. Peng, Z. Wang, B. Sa, B. Wu, Z. Sun, *ACS Appl Mater Interfaces* **2016**, *8*, 13449.

[136] Q. Peng, K. Hu, B. Sa, J. Zhou, B. Wu, X. Hou, Z. Sun, *Nano Research* **2017**, *10*, 3136.

[137] J. Sun, H. W. Lee, M. Pasta, H. Yuan, G. Zheng, Y. Sun, Y. Li, Y. Cui, *Nat Nanotechnol* **2015**, *10*, 980.

[138] H. Shuai, P. Ge, W. Hong, S. Li, J. Hu, H. Hou, G. Zou, X. Ji, *Small Methods* **2019**, *3*,

[139] S. Tan, Y. Jiang, Q. Wei, Q. Huang, Y. Dai, F. Xiong, Q. Li, Q. An, X. Xu, Z. Zhu, X. Bai, L. Mai, *Adv Mater* **2018**, *30*, e1707122.

[140] L. Chen, Y. Weng, Y. Meng, F. Dou, Z. An, P. Song, G. Chen, D. Zhang, *ACS Applied Energy Materials* **2020**, *3*, 9337.

[141] S. Wang, P. Xiong, X. Guo, J. Zhang, X. Gao, F. Zhang, X. Tang, P. H. L. Notten, G. Wang, *Advanced Functional Materials* **2020**, *30*,

[142] M. Goktas, C. Bolli, E. J. Berg, P. Novák, K. Pollok, F. Langenhorst, M. v. Roeder, O. Lenchuk, D. Mollenhauer, P. Adelhelm, *Advanced Energy Materials* **2018**, *8*,

[143] H.-K. Kim, K. C. Roh, K.-B. Kim, *Journal of The Electrochemical Society* **2015**, *162*, A2308.

[144] J. Min, K. Kierzek, X. Chen, P. K. Chu, X. Zhao, R. J. Kaleńczuk, T. Tang, E. Mijowska, *New Journal of Chemistry* **2017**, *41*, 13553.

[145] J. Min, X. Wen, T. Tang, X. Chen, K. Huo, J. Gong, J. Azadmanjiri, C. He, E. Mijowska, *Chem Commun (Camb)* **2020**, *56*, 9142.

[146] B.-W. Zhang, T. Sheng, Y.-X. Wang, S. Chou, K. Davey, S.-X. Dou, S.-Z. Qiao, *Angewandte Chemie* **2019**, *131*, 1498.

[147] G. Xu, J. Han, B. Ding, P. Nie, J. Pan, H. Dou, H. Li, X. Zhang, *Green Chemistry* **2015**, *17*, 1668.

[148] G. Xu, D. Yu, D. Zheng, S. Wang, W. Xue, X. E. Cao, H. Zeng, X. Xiao, M. Ge, W. K. Lee, M. Zhu, *iScience* **2020**, *23*, 101576.

[149] J. Song, X. Guo, J. Zhang, Y. Chen, C. Zhang, L. Luo, F. Wang, G. Wang, *Journal of Materials Chemistry A* **2019**, *7*, 6507.

[150] Q. Zhang, Y. Wang, Z. W. Seh, Z. Fu, R. Zhang, Y. Cui, *Nano Lett* **2015**, *15*, 3780.

[151] G. Zhou, H. Tian, Y. Jin, X. Tao, B. Liu, R. Zhang, Z. W. Seh, D. Zhuo, Y. Liu, J. Sun, J. Zhao, C. Zu, D. S. Wu, Q. Zhang, Y. Cui, *Proc Natl Acad Sci U S A* **2017**, *114*, 840.

[152] C. Ye, Y. Jiao, H. Jin, A. D. Slattery, K. Davey, H. Wang, S. Z. Qiao, *Angew Chem Int Ed Engl* **2018**, *57*, 16703.

[153] Z. Du, X. Chen, W. Hu, C. Chuang, S. Xie, A. Hu, W. Yan, X. Kong, X. Wu, H. Ji, L. J. Wan, *J Am Chem Soc* **2019**, *141*, 3977.

[154] L. Cao, X. Gao, B. Zhang, X. Ou, J. Zhang, W. B. Luo, *ACS Nano* **2020**, *14*, 3610.

[155] J. He, A. Bhargav, H. Yaghoobnejad Asl, Y. Chen, A. Manthiram, *Advanced Energy Materials* **2020**, *10*, 2001017.

[156] B. Zhang, C. Luo, Y. Deng, Z. Huang, G. Zhou, W. Lv, Y.-B. He, Y. Wan, F. Kang, Q.-H. Yang, *Advanced Energy Materials* **2020**, *10*, 2000091.

[157] J.-L. Yang, S.-X. Zhao, Y.-M. Lu, X.-T. Zeng, W. Lv, G.-Z. Cao, *Nano Energy* **2020**, *68*,

[158] T. Zhou, W. Lv, J. Li, G. Zhou, Y. Zhao, S. Fan, B. Liu, B. Li, F. Kang, Q.-H. Yang, *Energy & Environmental Science* **2017**, *10*, 1694.

[159] X. Gao, D. Zhou, Y. Chen, W. Wu, D. Su, B. Li, G. Wang, *Communications Chemistry* **2019**, *2*,

[160] B. Zhang, C. Luo, Y. Deng, Z. Huang, G. Zhou, W. Lv, Y. B. He, Y. Wan, F. Kang, Q. H. Yang, *Advanced Energy Materials* **2020**, *10*,

[161] N. Wei, J. Cai, R. Wang, M. Wang, W. Lv, H. Ci, J. Sun, Z. Liu, *Nano Energy* **2019**, *66*,

[162] Y. Song, W. Zhao, L. Kong, L. Zhang, X. Zhu, Y. Shao, F. Ding, Q. Zhang, J. Sun, Z. Liu, *Energy & Environmental Science* **2018**, *11*, 2620.

[163] R. Li, X. Zhou, H. Shen, M. Yang, C. Li, *ACS Nano* **2019**, *13*, 10049.

[164] X. Guo, B. Sun, D. Su, X. Liu, H. Liu, Y. Wang, G. Wang, *Science Bulletin* **2017**, *62*, 442.

[165] Z. Zhang, X.-G. Wang, X. Zhang, Z. Xie, Y.-N. Chen, L. Ma, Z. Peng, Z. Zhou, *Advanced Science* **2018**, *5*, 1700567.

[166] J. Wang, R. Gao, L. Zheng, Z. Chen, Z. Wu, L. Sun, Z. Hu, X. Liu, *ACS Catalysis* **2018**, *8*, 8953.

[167] R. Liang, C. Shu, A. Hu, M. Li, Z. Ran, R. Zheng, J. Long, *Chemical Engineering Journal* **2020**, *393*, 124592.

[168] W. Zhang, Y. Liu, Z. Guo, *Sci Adv* **2019**, *5*, eaav7412.

[169] K. Song, C. Liu, L. Mi, S. Chou, W. Chen, C. Shen, *Small* **2019**, e1903194.

[170] Y. Wu, S. Hu, R. Xu, J. Wang, Z. Peng, Q. Zhang, Y. Yu, *Nano Letters* **2019**, *19*, 1351.

[171] H. Gao, X. Guo, S. Wang, F. Zhang, H. Liu, G. Wang, *EcoMat* **2020**, *2*, e12027.

[172] B. Y. Wang, Z. W. Deng, Y. T. Xia, J. X. Hu, H. J. Li, H. Wu, Q. B. Zhang, Y. Zhang, H. K. Liu, S. X. Dou, *Advanced Energy Materials* **2020**, *10*,

[173] H. Wang, X. Wu, X. Qi, W. Zhao, Z. Ju, *Materials Research Bulletin* **2018**, *103*, 32.

[174] Y. Zhu, L. Peng, Z. Fang, C. Yan, X. Zhang, G. Yu, *Advanced Materials* **2018**, *30*,

[175] Y. Wu, H. B. Huang, Y. Feng, Z. S. Wu, Y. Yu, *Adv Mater* **2019**, *31*, e1901414.

[176] F. Yang, H. Gao, J. Chen, Z. Guo, *Small Methods* **2017**, *1*, 1700216.

[177] E. Pomerantseva, F. Bonaccorso, X. Feng, Y. Cui, Y. Gogotsi, *Science* **2019**, *366*, eaan8285.

[178] R. Zhao, H. Di, C. Wang, X. Hui, D. Zhao, R. Wang, L. Zhang, L. Yin, *ACS Nano* **2020**, *14*, 13938.

[179] H. Chen, N. Chen, M. Zhang, M. Li, Y. Gao, C. Wang, G. Chen, F. Du, *Nanotechnology* **2019**, *30*, 134001.

[180] H. Tan, D. Chen, X. Rui, Y. Yu, *Advanced Functional Materials* **2019**, *29*, 1808745.

[181] H. Gao, T. Zhou, Y. Zheng, Y. Liu, J. Chen, H. Liu, Z. Guo, *Advanced Energy Materials* **2016**, *6*, 1601037.

[182] R. Meng, J. Huang, Y. Feng, L. Zu, C. Peng, L. Zheng, L. Zheng, Z. Chen, G. Liu, B. Chen, Y. Mi, J. Yang, *Advanced Energy Materials* **2018**, *8*, 1801514.

[183] S. Wang, S. Zhao, X. Guo, G. Wang, *Advanced Energy Materials* **2021**, *n/a*, 2100864.

[184] J. Yang, W. Li, D. Wang, Y. Li, *Advanced Materials* **2020**, *32*, 2003300.

[185] P. Su, W. Pei, X. Wang, Y. Ma, Q. Jiang, J. Liang, S. Zhou, J. Zhao, J. Liu, G. Q. Lu, *Angewandte Chemie* **2021**,

[186] J. Gu, M. Jian, L. Huang, Z. Sun, A. Li, Y. Pan, J. Yang, W. Wen, W. Zhou, Y. Lin, H. J. Wang, X. Liu, L. Wang, X. Shi, X. Huang, L. Cao, S. Chen, X. Zheng, H. Pan, J. Zhu, S. Wei, W. X. Li, J. Lu, *Nat Nanotechnol* **2021**, *16*, 1141.

[187] A. VahidMohammadi, J. Rosen, Y. Gogotsi, *Science* **2021**, *372*, eabf1581.

[188] J. Pang, R. G. Mendes, A. Bachmatiuk, L. Zhao, H. Q. Ta, T. Gemming, H. Liu, Z. Liu, M. H. Rummeli, *Chemical Society Reviews* **2019**, *48*, 72.

[189] K. L. Firestein, J. E. von Treifeldt, D. G. Kvashnin, J. F. S. Fernando, C. Zhang, A. G. Kvashnin, E. V. Podryabinkin, A. V. Shapeev, D. P. Siriwardena, P. B. Sorokin, D. Golberg, *Nano Letters* **2020**, *20*, 5900.

[190] Kresse, Hafner, *Physical review. B, Condensed matter* **1994**, *49*, 14251.

[191] Kresse, Furthmuller, *Physical review. B, Condensed matter* **1996**, *54*, 11169.

[192] Perdew, Burke, Wang, *Physical review. B, Condensed matter* **1996**, *54*, 16533.

[193] Blochl, *Physical review. B, Condensed matter* **1994**, *50*, 17953.

[194] D. Zhao, Z. Chen, W. Yang, S. Liu, X. Zhang, Y. Yu, W.-C. Cheong, L. Zheng, F. Ren, G. Ying, X. Cao, D. Wang, Q. Peng, G. Wang, C. Chen, *Journal of the American Chemical Society* **2019**, *141*, 4086.

[195] C. Xia, Y. Qiu, Y. Xia, P. Zhu, G. King, X. Zhang, Z. Wu, J. Y. Kim, D. A. Cullen, D. Zheng, P. Li, M. Shakouri, E. Heredia, P. Cui, H. N. Alshareef, Y. Hu, H. Wang, *Nature Chemistry* **2021**,

[196] F. Bu, M. M. Zagho, Y. Ibrahim, B. Ma, A. Elzatahry, D. Zhao, *Nano Today* **2020**, *30*, 100803.

[197] C. Tang, Y. Min, C. Chen, W. Xu, L. Xu, *Nano Letters* **2019**, *19*, 5577.

[198] Q. Zhang, J. Mao, W. K. Pang, T. Zheng, V. Sencadas, Y. Chen, Y. Liu, Z. Guo, *Advanced Energy Materials* **2018**, *8*,

[199] L. Madec, V. Gabaudan, G. Gachot, L. Stievano, L. Monconduit, H. Martinez, *Acs Applied Materials & Interfaces* **2018**, *10*, 34116.

[200] S. Zhao, Z. Liu, G. Xie, X. Guo, Z. Guo, F. Song, G. Li, C. Chen, X. Xie, N. Zhang, B. Sun, S. Guo, G. Wang, *Angewandte Chemie International Edition n/a*,

[201] Q. Liu, L. Fan, S. Chen, S. Su, R. Ma, X. Han, B. Lu, *Energy Technology* **2019**, *7*,

[202] Y. Liu, Z. Tai, J. Zhang, W. K. Pang, Q. Zhang, H. Feng, K. Konstantinov, Z. Guo, H. K. Liu, *Nat Commun* **2018**, *9*, 3645.

[203] D. Liu, L. Yang, Z. Chen, G. Zou, H. Hou, J. Hu, X. Ji, *Science Bulletin* **2020**, *65*, 1003.

[204] Y. An, Y. Tian, L. Ci, S. Xiong, J. Feng, Y. Qian, *ACS Nano* **2018**, *12*, 12932.

[205] Y. N. Ko, S. H. Choi, H. Kim, H. J. Kim, *ACS Appl Mater Interfaces* **2019**, *11*, 27973.

[206] Z. Yi, Y. Qian, J. Tian, K. Shen, N. Lin, Y. Qian, *Journal of Materials Chemistry A* **2019**, *7*, 12283.

[207] Y. Han, T. Li, Y. Li, J. Tian, Z. Yi, N. Lin, Y. Qian, *Energy Storage Materials* **2019**, *20*, 46.

[208] N. Cheng, J. G. Zhao, L. Fan, Z. M. Liu, S. H. Chen, H. B. Ding, X. Z. Yu, Z. G. Liu, B. G. Lu, *Chemical Communications* **2019**, *55*, 12511.

[209] Y. N. Ko, S. H. Choi, H. Kim, H. J. Kim, *Acs Applied Materials & Interfaces* **2019**, *11*, 27973.

[210] Q. Liu, L. Fan, S. Chen, S. Su, R. Ma, X. Han, B. Lu, *Energy Technology* **2019**, *7*, 1900634.

[211] D. Liu, L. Yang, Z. Chen, G. Zou, H. Hou, J. Hu, X. Ji, *Science Bulletin* **2020**,

[212] Y. Liu, Z. Tai, J. Zhang, W. K. Pang, Q. Zhang, H. Feng, K. Konstantinov, Z. Guo, H. K. Liu, *Nature Communications* **2018**, *9*, 3645.

[213] Z. Yi, Y. Qian, J. Tian, K. Z. Shen, N. Lin, Y. T. Qian, *Journal of Materials Chemistry A* **2019**, *7*, 12283.

[214] Z. Y. Wang, K. Z. Dong, D. Wang, S. H. Luo, Y. G. Liu, Q. Wang, Y. H. Zhang, A. M. Hao, C. S. Shi, N. Q. Zhao, *Journal of Materials Chemistry A* **2019**, *7*, 14309.

[215] K. Liu, Y. Liu, D. Lin, A. Pei, Y. Cui, *Sci. Adv.* **2018**, *4*, eaas9820.

[216] J. Lu, T. Wu, K. Amine, *Nat. Energy* **2017**, *2*, 17011.

[217] H. Kim, J. C. Kim, M. Bianchini, D.-H. Seo, J. Rodriguez-Garcia, G. Ceder, *Adv. Energy Mater.* **2018**, *8*, 1702384.

[218] K. Kubota, M. Dahbi, T. Hosaka, S. Kumakura, S. Komaba, *Chem. Rec.* **2018**, *18*, 459.

[219] J.-Y. Hwang, S.-T. Myung, Y.-K. Sun, *Adv. Funct. Mater.* **2018**, *28*, 1802938.

[220] X. Tang, D. Zhou, P. Li, X. Guo, B. Sun, H. Liu, K. Yan, Y. Gogotsi, G. Wang, *Adv. Mater.* **2019**, *32*, 1906739.

[221] H. Tian, X. Yu, H. Shao, L. Dong, Y. Chen, X. Fang, C. Wang, W. Han, G. Wang, *Adv. Energy Mater.* **2019**, *9*, 1901560.

[222] Z. Jian, W. Luo, X. Ji, *J. Am. Chem. Soc.* **2015**, *137*, 11566.

[223] B. Cao, Q. Zhang, H. Liu, B. Xu, S. Zhang, T. Zhou, J. Mao, W. K. Pang, Z. Guo, A. Li, J. Zhou, X. Chen, H. Song, *Adv. Energy Mater.* **2018**, *8*, 1801149.

[224] L. Wang, J. Yang, J. Li, T. Chen, S. Chen, Z. Wu, J. Qiu, B. Wang, P. Gao, X. Niu, H. Li, *J. Power Sources* **2019**, *409*, 24.

[225] X. He, J. Liao, Z. Tang, L. Xiao, X. Ding, Q. Hu, Z. Wen, C. Chen, *J. Power Sources* **2018**, *396*, 533.

[226] J. Zhao, X. Zou, Y. Zhu, Y. Xu, C. Wang, *Adv. Funct. Mater.* **2016**, *26*, 8103.

[227] S. Wang, S. Liu, X. Li, C. Li, R. Zang, Z. Man, Y. Wu, P. Li, G. Wang, *Chem. Eur. J.* **2018**, *24*, 3873.

[228] J. Zheng, Y. Yang, X. Fan, G. Ji, X. Ji, H. Wang, S. Hou, M. R. Zachariah, C. Wang, *Energy Environ. Sci.* **2019**, *12*, 615.

[229] V. Gabaudan, R. Berthelot, L. Stievano, L. Monconduit, *J. Phys. Chem. C* **2018**, *122*, 18266.

[230] L. Wang, Q. Zhang, J. Zhu, X. Duan, Z. Xu, Y. Liu, H. Yang, B. Lu, *Energy Storage Mater.* **2019**, *16*, 37.

[231] Q. Zhang, L. Wang, J. Wang, X. Yu, J. Ge, H. Zhang, B. Lu, *J. Mater. Chem. A* **2018**, *6*, 9411.

[232] J. Ge, B. Wang, J. Wang, Q. Zhang, B. Lu, *Adv. Energy Mater.* **2019**, *10*, 1903277.

[233] Y. Liu, Z. Tai, J. Zhang, W. K. Pang, Q. Zhang, H. Feng, K. Konstantinov, Z. Guo, H. K. Liu, *Nat. Commun.* **2018**, *9*, 3645.

[234] W. Zhang, Y. Liu, Z. Guo, *Sci. Adv.* **2019**, *5*, eaav7412.

[235] I. Sultana, M. M. Rahman, Y. Chen, A. M. Glushenkov, *Adv. Funct. Mater.* **2018**, *28*, 1703857.

[236] Z. Yi, Y. Qian, J. Tian, K. Shen, N. Lin, Y. Qian, *J. Mater. Chem. A* **2019**, *7*, 12283.

[237] S. Fang, L. Shen, S. Li, G. T. Kim, D. Bresser, H. Zhang, X. Zhang, J. Maier, S. Passerini, *ACS Nano* **2019**, *13*, 9511.

[238] Q. Liu, L. Fan, R. Ma, S. Chen, X. Yu, H. Yang, Y. Xie, X. Han, B. Lu, *Chem. Commun.* **2018**, *54*, 11773.

[239] P. Xiong, P. Bai, S. Tu, M. Cheng, J. Zhang, J. Sun, Y. Xu, *Small* **2018**, *14*, 1802140.

[240] W. Sun, L. Wan, X. Li, X. Zhao, X. Yan, *J. Mater. Chem. A* **2016**, *4*, 10948.

[241] Y. Ma, R. Younesi, R. Pan, C. Liu, J. Zhu, B. Wei, K. Edström, *Adv. Funct. Mater.* **2016**, *26*, 6797.

[242] P. Xiong, R. Ma, N. Sakai, T. Sasaki, *ACS Nano* **2018**, *12*, 1768.

[243] X. Xie, S. Wang, K. Kretschmer, G. Wang, *J. Colloid Interface Sci.* **2017**, *499*, 17.

[244] P. Xiong, B. Sun, N. Sakai, R. Ma, T. Sasaki, S. Wang, J. Zhang, G. Wang, *Adv. Mater.* **2019**, 1902654.

[245] Z. Yi, Y. Qian, S. Jiang, Y. Li, N. Lin, Y. Qian, *Chem. Eng. J.* **2020**, *379*, 122352.

[246] P. Xiong, J. Zhu, L. Zhang, X. Wang, *Nanoscale Horiz.* **2016**, *1*, 340.

[247] X. Wang, H. Wang, Q. Li, H. Li, J. Xu, G. Zhao, H. Li, P. Guo, S. Li, Y.-k. Sun, *J. Electrochem. Soc.* **2017**, *164*, A2922.

[248] Y.-T. Xu, Y. Guo, C. Li, X.-Y. Zhou, M. C. Tucker, X.-Z. Fu, R. Sun, C.-P. Wong, *Nano Energy* **2015**, *11*, 38.

[249] X. Liu, D. Chao, Q. Zhang, H. Liu, H. Hu, J. Zhao, Y. Li, Y. Huang, J. Lin, Z. X. Shen, *Sci. Rep.* **2015**, *5*, 15665.

[250] D. Y. Yu, P. V. Prikhodchenko, C. W. Mason, S. K. Batabyal, J. Gun, S. Sladkevich, A. G. Medvedev, O. Lev, *Nat. Commun.* **2013**, *4*, 2922.

[251] P. Ge, X. Cao, H. Hou, S. Li, X. Ji, *ACS Appl. Mater. Interfaces* **2017**, *9*, 34979.

[252] H. Hou, M. Jing, Z. Huang, Y. Yang, Y. Zhang, J. Chen, Z. Wu, X. Ji, *ACS Appl. Mater. Interfaces* **2015**, *7*, 19362.

[253] W. Zhao, C. M. Li, *J. Colloid Interface Sci.* **2017**, *488*, 356.

[254] Y. Zhang, P. Chen, X. Gao, B. Wang, H. Liu, H. Wu, H. Liu, S. Dou, *Adv. Funct. Mater.* **2016**, *26*, 7754.

[255] S. Tan, Y. Jiang, Q. Wei, Q. Huang, Y. Dai, F. Xiong, Q. Li, Q. An, X. Xu, Z. Zhu, X. Bai, L. Mai, *Adv. Mater.* **2018**, *30*, 1707122.

[256] X. Ou, C. Yang, X. Xiong, F. Zheng, Q. Pan, C. Jin, M. Liu, K. Huang, *Adv. Funct. Mater.* **2017**, *27*, 1606242.

[257] H. Liu, M. Jia, B. Cao, R. Chen, X. Lv, R. Tang, F. Wu, B. Xu, *J. Power Sources* **2016**, *319*, 195.

[258] L. Fan, R. Ma, Q. Zhang, X. Jia, B. Lu, *Angew. Chem. Int. Ed.* **2019**, *58*, 10500.

[259] R. Zhang, J. Bao, Y. Wang, C. F. Sun, *Chem. Sci.* **2018**, *9*, 6193.

[260] W. Luo, J.-J. Gaumet, P. Magri, S. Diliberto, F. Li, P. Franchetti, J. Ghanbaja, L. Mai, *J. Energy Chem.* **2019**, *30*, 27.

[261] W. Li, M. Zhou, H. Li, K. Wang, S. Cheng, K. Jiang, *Electrochem. Commun.* **2015**, *60*, 74.

[262] W. Luo, A. Calas, C. Tang, F. Li, L. Zhou, L. Mai, *ACS Appl. Mater. Interfaces* **2016**, *8*, 35219.

[263] K.-H. Nam, C.-M. Park, *J. Power Sources* **2019**, *433*, 126639.

[264] Y. Fang, X. Y. Yu, X. W. D. Lou, *Angew. Chem. Int. Ed.* **2018**, *57*, 9859.

[265] N. W. Tideswell, F. H. Kruse, J. D. McCullough, *Acta Cryst.* **1957**, *10*, 99.

[266] V. Gabaudan, R. Berthelot, L. Stievano, L. Monconduit, *ACS Omega* **2018**, *3*, 12195.

[267] Y. Liu, Z. Tai, Q. Zhang, H. Wang, W. K. Pang, H. K. Liu, K. Konstantinov, Z. Guo, *Nano Energy* **2017**, *35*, 36.

[268] L. Su, Z. Zhou, M. Ren, *Chem. Commun.* **2010**, *46*, 2590.

[269] S. Chen, L. Shen, P. A. van Aken, J. Maier, Y. Yu, *Adv. Mater.* **2017**, *29*, 1605650.

[270] J. Liu, Q. Zhang, T. Zhang, J.-T. Li, L. Huang, S.-G. Sun, *Adv. Funct. Mater.* **2015**, *25*, 3599.

[271] Y. N. Ko, S. H. Choi, H. Kim, H. J. Kim, *ACS Appl. Mater. Interfaces* **2019**, *11*, 27973.

[272] B. Tang, L. Shan, S. Liang, J. Zhou, *Energy & Environmental Science* **2019**, *12*, 3288.

[273] W. Shi, W. S. V. Lee, J. Xue, *ChemSusChem* **2021**, *14*, 1634.

[274] Y. Zhao, Y. Zhu, X. Zhang, *InfoMat* **2019**, *2*, 237.

[275] S. Huang, J. Zhu, J. Tian, Z. Niu, *Chemistry* **2019**, *25*, 14480.

[276] H. Pan, Y. Shao, P. Yan, Y. Cheng, K. S. Han, Z. Nie, C. Wang, J. Yang, X. Li, P. Bhattacharya, K. T. Mueller, J. Liu, *Nature Energy* **2016**, *1*,

[277] N. Zhang, F. Cheng, J. Liu, L. Wang, X. Long, X. Liu, F. Li, J. Chen, *Nat Commun* **2017**, *8*, 405.

[278] Y. Xu, J. Zhu, J. Feng, Y. Wang, X. Wu, P. Ma, X. Zhang, G. Wang, X. Yan, *Energy Storage Materials* **2021**, *38*, 299.

[279] C. Qiu, X. Zhu, L. Xue, M. Ni, Y. Zhao, B. Liu, H. Xia, *Electrochimica Acta* **2020**, *351*,

[280] H. Chen, S. Cai, Y. Wu, W. Wang, M. Xu, S. J. Bao, *Materials Today Energy* **2021**, *20*,

[281] B. Wu, G. Zhang, M. Yan, T. Xiong, P. He, L. He, X. Xu, L. Mai, *Small* **2018**, *14*, e1703850.

[282] S. Islam, M. H. Alfaruqi, J. Song, S. Kim, D. T. Pham, J. Jo, S. Kim, V. Mathew, J. P. Baboo, Z. Xiu, J. Kim, *Journal of Energy Chemistry* **2017**, *26*, 815.

[283] J. Huang, X. Tang, K. Liu, G. Fang, Z. He, Z. Li, *Materials Today Energy* **2020**, *17*,

[284] S. Guo, S. Liang, B. Zhang, G. Fang, D. Ma, J. Zhou, *ACS Nano* **2019**, *13*, 13456.

[285] J. Ji, H. Wan, B. Zhang, C. Wang, Y. Gan, Q. Tan, N. Wang, J. Yao, Z. Zheng, P. Liang, J. Zhang, H. Wang, L. Tao, Y. Wang, D. Chao, H. Wang, *Advanced Energy Materials* **2020**, *11*,

[286] D. Zhang, J. Cao, X. Zhang, N. Insin, S. Wang, J. Han, Y. Zhao, J. Qin, Y. Huang, *Advanced Functional Materials* **2021**, *31*,

[287] L. Liu, Y. C. Wu, L. Huang, K. Liu, B. Duployer, P. Rozier, P. L. Taberna, P. Simon, *Advanced Energy Materials* **2021**, *11*,

[288] Q. Xie, G. Cheng, T. Xue, L. Huang, S. Chen, Y. Sun, M. Sun, H. Wang, L. Yu, *Materials Today Energy* **2021**,

[289] J. Huang, Z. Wang, M. Hou, X. Dong, Y. Liu, Y. Wang, Y. Xia, *Nat Commun* **2018**, *9*, 2906.

[290] Y. Yang, Y. Feng, Z. Chen, Y. Feng, Q. Huang, C. Ma, Q. Xia, C. Liang, L. Zhou, M. S. Islam, P. Wang, L. Zhou, L. Mai, W. Wei, *Nano Energy* **2020**, *76*,

[291] P. Liu, W. He, Q. Xie, Y. Cheng, W. Xu, Z. Qiao, L. Wang, B. Qu, Z. Z. Zhu, D. L. Peng, *J Phys Chem Lett* **2019**, *10*, 2202.

[292] P. Liu, W. He, Y. Cheng, Q. Wang, C. Zhang, Q. Xie, J. Han, Z. Qiao, H. Zheng, Q. Liu, L. Wang, B. Qu, Q. Luo, Z. Z. Zhu, D. L. Peng, *J Phys Chem Lett* **2020**, *11*, 2322.

[293] N. Muralidharan, R. Carter, L. Oakes, A. P. Cohn, C. L. Pint, *Sci Rep* **2016**, *6*, 27542.

[294] N. Muralidharan, C. N. Brock, A. P. Cohn, D. Schauben, R. E. Carter, L. Oakes, D. G. Walker, C. L. Pint, *ACS Nano* **2017**, *11*, 6243.

[295] L. Oakes, R. Carter, T. Hanken, A. P. Cohn, K. Share, B. Schmidt, C. L. Pint, *Nat Commun* **2016**, *7*, 11796.

[296] Z. Du, C. Wu, Y. Chen, Z. Cao, R. Hu, Y. Zhang, J. Gu, Y. Cui, H. Chen, Y. Shi, J. Shang, B. Li, S. Yang, *Adv Mater* **2021**, *33*, e2101473.

[297] Y. Y. Kazuya Kai, Hiroshi Kageyama, Gunzi Saito, Tetsuo Ishigaki, Yu Furukawa, and Jun Kawamata, *Journal of the American Chemical Society* **2008**, *130*, 15938.

[298] P. Xiong, B. Sun, N. Sakai, R. Ma, T. Sasaki, S. Wang, J. Zhang, G. Wang, *Adv Mater* **2020**, *32*, e1902654.

[299] C. Julien, *Solid State Ionics* **2003**, *159*, 345.

[300] A. V. Soldatova, G. Balakrishnan, O. F. Oyerinde, C. A. Romano, B. M. Tebo, T. G. Spiro, *Environ Sci Technol* **2019**, *53*, 4185.

[301] Y. M. Xiaojing Yang, Zong-huai Liu, Kohji Sakane, and Kenta Ooi, *Chem. Mater.* **2004**, *16*, 5581.

[302] W. Sun, F. Wang, S. Hou, C. Yang, X. Fan, Z. Ma, T. Gao, F. Han, R. Hu, M. Zhu, C. Wang, *J Am Chem Soc* **2017**, *139*, 9775.

[303] M. H. Alfaruqi, J. Gim, S. Kim, J. Song, D. T. Pham, J. Jo, Z. Xiu, V. Mathew, J. Kim, *Electrochemistry Communications* **2015**, *60*, 121.

[304] P. Nakhanivej, X. Yu, S. K. Park, S. Kim, J.-Y. Hong, H. J. Kim, W. Lee, J. Y. Hwang, J. E. Yang, C. Wolverton, J. Kong, M. Chhowalla, H. S. Park, *Nature Materials* **2019**, *18*, 156.

[305] B. Rieger, S. Schlueter, S. V. Erhard, A. Jossen, *Journal of The Electrochemical Society* **2016**, *163*, A1595.

[306] H. Michael, F. Iacoviello, T. M. M. Heenan, A. Llewellyn, J. S. Weaving, R. Jervis, D. J. L. Brett, P. R. Shearing, *Journal of The Electrochemical Society* **2021**, *168*,

[307] R. Tian, M. Breshears, D. V. Horvath, J. N. Coleman, *ACS Nano* **2020**, *14*, 3129.